

SOLUTION OF BOHR HAMILTONIAN

SOLUTION OF THE BOHR HAMILTONIAN WITH  
APPLICATION TO HIGH SPIN STATES

By

BRIAN CLARKE SMITH, B.SC., M.A.

A Thesis

Submitted to the School of Graduate Studies  
in Partial Fulfilment of the Requirements  
for the Degree  
Doctor of Philosophy

McMaster University

December 1975

DOCTOR OF PHILOSOPHY (1975)  
(Physics)

McMASTER UNIVERSITY  
Hamilton, Ontario

TITLE: Solution of Bohr Hamiltonian with Application  
to High Spin States

AUTHOR: Brian Clarke Smith, B.Sc. (McMaster University)  
M.A. (State University of New  
York at Stony Brook)

SUPERVISOR: Professor A.B. Volkov

NUMBER OF PAGES: x, 184

## ABSTRACT

The structure of rare earth nuclei in high spin states is investigated using two collective models. The first model is a generalization of the Variable Moment of Inertia model to allow for axially asymmetric deformation. This model predicts that at sufficiently high spin, the nucleus will minimize its rotational energy by changing from an axially symmetric to an axially asymmetric shape. This sudden shape change can cause a phenomenon described as "backbending". This model also provides a natural explanation for the phenomenon of "forking" as observed in  $\text{Ba}^{126}$  and  $\text{Os}^{186}$ .

The second model investigated is the quadrupole collective model of Bohr and Mottelson. The Schrödinger equation with the Bohr-Mottelson Hamiltonian is solved numerically for states with angular momentum as high as  $20\hbar$ . The method is valid for arbitrary collective potential energy and arbitrary inertial functions. The method involves converting the partial differential equation into a matrix eigenvalue equation using finite difference techniques. The resulting Hamiltonian matrix is diagonalized using the Lanczos algorithm. The results confirm the prediction of the previous model that backbending can result from a shape change.  $E2$  transition rates are calculated and found to agree with rigid rotor estimates to within a factor of 2.

The method of solution of the Bohr-Mottelson Hamiltonian

is extended to odd particle nuclei. It is found that the B representations of the  $D_2$  group are likely to be of physical importance in odd-even nuclei, a result which appears never to have been considered before.

## ACKNOWLEDGEMENTS

It is a pleasure to thank my supervisor, Professor Anatole Volkov, for the assistance he has given me. His boundless optimism and healthy enthusiasm greatly aided the completion of this thesis.

I wish to thank Professor Jim Waddington for making several helpful suggestions. I must also acknowledge my fellow graduate students, too numerous to mention by name, for their occasional assistance.

I am also indebted to the tax payers of Ontario for providing me with enough financial support to live on.

Finally I would like to express my sincere gratitude to Mrs. Helen Kennelly who, under trying circumstances, quickly transcribed almost indecipherable handwriting into a typed manuscript.

## TABLE OF CONTENTS

	<u>Page</u>
CHAPTER 1      INTRODUCTION	1
CHAPTER 2      VARIABLE MOMENT OF INERTIA MODELS	
I      Some Early Models of High Spin States	7
II     VMI Model of Mariscotti, Scharff-Goldhaber and Buck	11
III    Backbending	15
IV    Theoretical Justification of the VMI Model	17
V     An Axially Asymmetric VMI Model	24
VI    Results of VMIA Model for Ground State Band	28
VII   The VMIA Model and the Gamma Band	33
CHAPTER 3      BOHR'S COLLECTIVE MODEL: THEORY	
I      Introduction	43
II     Collective Model	46
III    Numerical Methods: Vibrational and Potential Energies	55
IV    Numerical Methods: Rotational Energy	68
V     Construction and Diagonalization of the Hamiltonian	74
VI    Electromagnetic Multipole Moments	87
CHAPTER 4      BOHR'S COLLECTIVE MODEL: RESULTS	
I      Test of Method: Spherical Harmonic Oscillator	92
II     Test of Method: Deformed Prolate Rotor	99
III    Features of Band Crossing	103

	<u>Page</u>
IV Choice of Inputs	105
V Er <sup>164</sup>	108
VI Er <sup>162</sup>	118
VII Os <sup>182</sup>	118
VIII Comparison of Variable Moment of Inertia Models with Bohr's Collective Model	128
CHAPTER 5 EXTENSION OF THE BOHR HAMILTONIAN SOLUTION TO ODD PARTICLE NUCLEI	
I Introduction	139
II Model Calculation: Single Nilsson Orbital	142
III Results of Model Calculation	146
CHAPTER 6 SUMMARY AND DISCUSSION	151
APPENDIX A D <sub>2</sub> GROUP	157
APPENDIX B THE QUANTUM-MECHANICAL ASYMMETRIC ROTOR	158
APPENDIX C SYMMETRIES OF THE BOHR COLLECTIVE HAMILTONIAN	162
APPENDIX D BRIEF DESCRIPTION OF SPLINE FUNCTIONS	166
APPENDIX E NUMERICAL INTEGRATION AND DIFFERENTIATION WEIGHTS	168
APPENDIX F BOUNDARY CONDITIONS AT $\gamma = \pi/3$	173
BIBLIOGRAPHY	180



# LIST OF TABLES

	<u>Page</u>
Table 3.1 Numerical Differentiation Constants: Matrix $R_{\alpha\beta\gamma}$	66
Table 4.1 $B(E2)$ 's for Harmonic Oscillators	98
Table 4.2 Probability that Wavefunction has $J_3 = K$	103
Table A.1 Character Table of $D_2$ Group	157

# LIST OF FIGURES

<u>Figure</u>		<u>Page</u>
2.1	$J-\omega^2$ plot of $\text{Er}^{162}$ data	14
2.2	Energy levels of a rigid asymmetric rotor	26
2.3	Energy levels of the VMIA model	30
2.4	$J-\omega^2$ plot of the energy levels of the VMIA model	32
2.5	$J-\omega^2$ plot of $\text{Os}^{186}$ and $\text{Ba}^{126}$ data showing forking	34
2.6	Energies of the VMIA model for $\text{Er}^{162}$ on an $J-\omega^2$ plot	35
2.7	Energy levels of $\gamma$ band from VMIA model	39
2.8	Correlation between critical angular momentum and " $\gamma$ stiffness"	42
3.1	Grid points in $\beta$ - $\gamma$ plane showing 4 major triangles	57
3.2	Single major triangle with x-y co-ordinate system	59
3.3	Numerical integration weights	62
3.4	Block structure of Hamiltonian matrix	73
3.5	Grid points showing cut-off parameter $\epsilon$	77
4.1	Energy levels of a harmonic oscillator	94
4.2	Energy levels of a harmonic oscillator	95
4.3	Wavefunction of $J=0$ state of harmonic oscillator	96

<u>Figure</u>		<u>Page</u>
4.4	Wavefunction of $J=0$ state of harmonic oscillator	97
4.5	Energy levels of prolate rotor	100
4.6	Energy levels of prolate rotor	102
4.7	Collective potential energy for $\text{Er}^{164}$	109
4.8	Energy levels of $\text{Er}^{164}$	111
4.9	Band crossing in $\text{Er}^{164}$	112
4.10	$\mathcal{J}-\omega^2$ plot for $\text{Er}^{164}$	114
4.11	Shape probability for $J=14$ state of $\text{Er}^{164}$	115
4.12	Shape probability for $J=16$ state of $\text{Er}^{164}$	116
4.13	$B(E2)$ 's for $\text{Er}^{164}$	117
4.14	Collective potential energy for $\text{Er}^{162}$	119
4.15	Energy levels of $\text{Er}^{162}$	120
4.16	$\mathcal{J}-\omega^2$ plot for $\text{Er}^{162}$	121
4.17	Collective potential energy for $\text{Os}^{182}$	122
4.18	Energy levels of $\text{Os}^{182}$	123
4.19	Band crossing in $\text{Os}^{182}$	125
4.20	$\mathcal{J}-\omega^2$ plot for $\text{Os}^{182}$	126
4.21	$B(E2)$ 's for $\text{Os}^{182}$	127
4.22	VMI-type "potential energies"	136
5.1	Calculated energy levels for A and B representations	148
5.2	Some experimental energy levels of $\text{Gd}^{151}$	149

## CHAPTER 1

### INTRODUCTION

One of the major tools which has been used to study the structure of atomic nuclei is spectroscopy. This technique involves measuring the energies, spins and parities of the stationary states of the nucleus. The goal of the theoretical physicist is to find a model which explains this data. The ground and excited states of a nucleus are extremely complicated quantum-mechanical systems. However many body theory suggests that the relationship between the ground state and the low lying excited states ("elementary excitations") can be relatively simple. Because of this it is possible to develop theories for more than just the lightest nuclei.

The history of nuclear physics is a good example of the interplay between theory and experiment. In the earliest days, there was very little experimental data on the excited states of a nucleus. The theories were correspondingly crude. For example the liquid drop theory predicted binding energies reasonably accurately. However this theory also predicted that all nuclei were spherical. With the advent of the technique of inelastic coulomb scattering it was possible to do spectroscopy on the lowest one or two excited states. The resultant spectra for some nuclei were somewhat reminiscent of the spectra

of rotating molecules. However according to quantum-mechanics, a spherical system can not rotate. Rainwater (Rai 50) realized that because of the spin dependence of the nuclear force, there was a tendency for the outer nucleons to "polarize" the nucleus. This implies that the equilibrium shape of some nuclei was deformed rather than spherical as the liquid drop model predicted. For this suggestion, Rainwater shared this year's Nobel Prize with Aage Bohr and Ben Mottelson.

In a series of papers in the early 1950's Bohr and Mottelson (Boh 52, BM 53) extended the ideas of Rainwater in developing an elaborate theory of collective motion. The Bohr-Mottelson theory has been spectacularly successful in explaining a large body of data including excitation energies, electromagnetic moments and lifetimes of nuclear states.

A steady refinement in experimental technique has resulted in not only more accurate data but also data on more states of more nuclei. Of particular interest to the study of this thesis is the structure of nuclei in high angular momentum states. Using the reaction  $(\alpha, xn\gamma)$  Morinaga and co-workers (MG 63, LM 65, ML 65, Mor 66) have been able to measure spectra of states in the ground state band as high as  $J = 12$ . Using heavy ions instead of  $\alpha$  particles, Stephens and co-workers (SLD 64, SLD 65, BDS 67, CDS+ 67, NSD 67) have extended the method to spins as high as  $J = 18$ . Large use is made of gamma-gamma coincidence techniques to determine the level schemes.

The reason for using heavy ions instead of, for example protons, is that heavy ions bring to the compound system a large amount of angular momentum without a corresponding large amount of energy.

Nuclear theoreticians have been unable to keep abreast of these developments. Nuclear spectra can be measured far more accurately than calculated. The structure of high spin states poses an interesting problem. The excitation spectra of many nuclei appear to be almost classical in nature. In particular, it appears that the excitation energy takes the form of kinetic energy of rotation. The classical relation between energy  $E$  and angular momentum  $J$  for a system rotating perpendicular to its symmetry axis is  $E = J^2/2I$ . Experimentally, the energy is approximately proportional to the square of the angular momentum. However if the classical formula for the moment of inertia is used, the answer is too large by a factor of about two. This means that nuclei do not rotate "rigidly". It is generally believed that pairing correlations reduce the effective moment of inertia from the "rigid" rotation value (Bel 59).

In 1972 the Stockholm group, using the  $(\alpha, xn\gamma)$  reaction, noticed that in  $\text{Er}^{162}$  at about  $J = 14$  the effective moment of inertia suddenly increased almost to the "rigid" rotor value. They called this effect backbending. Backbending is discussed in more detail in Chapter 2, Section III. Since then, backbending has been observed in more than a dozen nuclei. Several

theoretical explanations of this effect have been proposed. Most prominent among the microscopic theories are the Coriolis anti-pairing (CAP) effect of Mottelson and Valatin (MV 60) and the decoupling model of Stephens and Simon (SS 72).

The basic idea of the CAP effect is as follows. When the even-even nucleus is not rotating, pairs of identical particles are in degenerate time-reversed single particle states. Because of the short range of the nucleon-nucleon force, such pairs of particles tend to couple to  $J = 0$  thereby reducing the moment of inertia. However when the nucleus is rotating, the time reversal degeneracy is broken causing the pairing correlations to be weakened. For sufficiently high spin there should be no pairing correlations at all and the nucleus should rotate with the "rigid" rotor value of the moment of inertia. This is analogous to the Meisner effect in superconductivity.

In BCS theory there is no superconducting solution if the effective pairing strength  $G$  is smaller than some critical value  $G_c$ . In the CAP effect, the sudden vanishing of the gap is responsible for backbending. However the lack of a superconducting solution for  $G < G_c$  is a result in the approximations involved in the BCS model. It is not clear that this would happen if the Hamiltonian were solved more exactly. The attenuation of pairing correlations does, however, provide a natural explanation of the slow increase in the moment of inertia well below the critical angular momentum. Another problem with the CAP theory is the fact that a proper microscopic calculation

is very cumbersome. Ideally Hartree-Fock-Bogolyubov calculations with cranking, angular momentum and particle number projection before variation, and using a realistic interaction should be performed. Because of the technical difficulties involved, this has not yet been done.

At present interest in the microscopic theories is gravitating toward the decoupling model of Stephens and Simon (SS 72). They observe that the Coriolis force should be especially strong for nucleons in a state  $X_{\Omega}^j$  having large angular momentum  $j$  and small 3-projection  $\Omega$ . This is the case in the Nilsson model for neutrons at the Fermi level in the Er region of the periodic table. In this model a pair of  $i_{13/2}$  neutrons decouple from the rotating core and align their angular momentum along the axis of rotation. As a result the rotational band based on the appropriate two quasi-particle excitation crosses the ground state band at the critical angular momentum. Calculations have shown that this indeed can cause backbending. The decoupling model has difficulty in explaining backbending in the heavy rare earth nuclei where the  $i_{13/2}$  neutron states should be full.

The two microscopic theories are related. In the decoupling model, the pairing correlations in two nucleons are destroyed at the backbending point. In the CAP model, the pairing correlations in all the nucleons (or at least in all the neutrons) are destroyed at the backbending point. Any



particle aligned along the axis of rotation can not have good angular momentum along the symmetry axis of the core. Hence both theories predict that the nuclei can not have axial symmetry above the backbending point.

In this thesis a new theory of the structure of high spin states is presented. The basic idea is that at high angular momentum, the nucleus becomes axially asymmetric in shape. To investigate this idea, calculations are performed based on two collective theories: a generalized variable moment of inertia theory and the collective quadrupole theory of Bohr and Mottelson. The results of both these collective theories are compatible with the microscopic theories described previously. The collective theories provide an alternative but not incompatible viewpoint to the microscopic theories.

In Chapter 2, the variable moment of inertia model is generalized to allow for the possibility of axial asymmetry. It is shown that backbending can result from a sudden shape change. In Chapter 3 a method of solving the Bohr Hamiltonian for angular momentum as high as  $J = 20$  is described. In Chapter 4 the results of this method are given. Also in Chapter 4, the generalized variable moment of inertia model is compared to the Bohr collective model. In Chapter 5, the techniques used to solve the Bohr Hamiltonian are extended to odd particle nuclei. Finally a summary and discussion is given in Chapter 6.

## CHAPTER 2

### VARIABLE MOMENT OF INERTIA MODELS

#### I Some Early Models of High Spin States

##### 1. Power series

The simplest model for an even-even rotational nucleus is that of an axially symmetric rigid rotor. The state of this system is completely described by the two polar co-ordinates which give its orientation. The quantum-mechanical properties of this system are easily calculated. The excitation energies are

$$E_J = \frac{J(J+1)}{2\mathcal{I}} \quad (2.1)$$

Here the moment of inertia  $\mathcal{I}$  is independent of the angular momentum  $J$ . Because of symmetry reasons (see Appendix B),  $J$  is restricted to even integers. Thus the first three levels of a nucleus are predicted to have angular momenta  $J = 0, 2, 4$ , all with even parity. This prediction does indeed apply to a large number of even-even nuclei in the rare earth and actinide regions of the periodic table. Moreover, for many of these nuclei the level spacing given by equation (2.1) is approximately valid for the lowest few states.

Equation (2.1) predicts that the ratio of the energy of the second excited state to that of the first is  $3 \frac{1}{3}$ .

Experimentally this ratio is about 3.3 for good rotational nuclei. The deviations from equation (2.1) become progressively more severe for the higher states. The classic papers of Bohr and Mottelson (Boh 52; BM 53) showed that this deviation of the experimental spectra from that of a rigid rotor could be understood as a coupling between rotation and vibration.

In analogy with molecular spectra they modified equation (2.1) to

$$E_J = A J(J+1) - B(J(J+1))^2. \quad (2.2)$$

An explicit expression for B was given in terms of the  $\beta$  and  $\gamma$  stiffness parameters. However it was found that the agreement with experiment was significantly improved if B was taken as a phenomenological parameter and fitted to data. While equation (2.2) did result in improvement, it still was inadequate for the higher spin states.

Proceeding in the same spirit, additional terms were added to equation (2.2) yielding the equation

$$E_J = A J(J+1) - B(J(J+1))^2 + C(J(J+1))^3 + D(J(J+1))^4. \quad (2.3)$$

This time no attempt was made to give an expression for the parameters C and D. They were fitted to data for each nucleus. The addition of more parameters gives better agreement to experiment but no increase in knowledge of the physics involved. Moreover, to get reasonable fits, it takes almost as many

parameters as pieces of data. The energy is being expanded as a finite power series in  $J(J+1)$ . However  $J(J+1)$  is always greater than 1 and can be quite large indeed. As a result the highest term in the expansion becomes dominant for sufficiently high spin. This gives an unreasonable asymptotic behaviour for equation (2.3).

## 2. Centrifugal stretching models

Considerable effort has been devoted to obtaining a good fit to rotational spectra using a limited number (two or three) parameters. A major contribution to our understanding of rotational nuclei was made with the development of the Davydov-Chabon model (DC 60). Since details of this model are described elsewhere, only a brief sketch will be given here. The model is basically a simplification of the collective model of Bohr (Boh 52). The Davydov-Chabon (D-C) model involves an axially asymmetric rotor in which  $\beta$  stretching is treated quantum-mechanically. However the asymmetry parameter,  $\gamma$ , is taken to be a phenomenological constant rather than a dynamical co-ordinate.

A few years later, Diamond and co-workers (DSS 64) observed that the D-C model in the case of axial symmetry ( $\gamma = 0$ ) gave excellent results for the very high spin states. In this paper they outlined a classical analogue to the (axially symmetric) D-C model. They gave the following equations:

$$E_J = \frac{J(J+1)}{2J(\beta)} + \frac{1}{2} C (\beta - \beta_0)^2 \quad (2.4)$$

with

$$\mathcal{J}(\beta) = 3 B \beta^2 . \quad (2.5)$$

For each  $J$ , equation (2.4) was minimized with respect to  $\beta$ .

This procedure leads to a two parameter fit to the data.

Moszkowski (Mos 66) elaborated on the Diamond model to obtain the equations

$$E_J = \frac{1}{2J_0} \frac{FV(1+V)}{(1-V)^2} \quad (2.6 \text{ i})$$

$$J(J+1) = \frac{FV}{(1-V)^4} . \quad (2.6 \text{ ii})$$

The potential energy  $V$  is eliminated between the above two equations yielding a two-parameter formula for the energy as a function of angular momentum.

### 3. Harris model

The pair of equations (2.6) are similar to the two parameter equations proposed by Harris (Har 64). By considering higher terms in perturbation theory for the cranking (Ing 54) moment of inertia, he obtained the following:

$$E_J = \frac{1}{2} \omega^2 (\mathcal{J}_0 + 3 C \omega^2) \quad (2.7 \text{ i})$$

$$\sqrt{J(J+1)} = \omega (\mathcal{J}_0 + 2 C \omega^2) . \quad (2.7 \text{ ii})$$

Here  $\omega$  is eliminated between the two equations. Explicit expressions were given for  $\mathcal{J}_0$  and  $C$  using the cranking formalism. However using the method of least squares Harris fitted the

parameters  $\mathcal{J}_0$  and  $C$  to the data. In a second paper (Har 65) Harris extended his model to even higher order terms:

$$E_J = \frac{1}{2} \omega^2 (\mathcal{J}_0 + 3 C \omega^2 + 5 D \omega^4 + 7 F \omega^6 + \dots) \quad (2.8 \text{ i})$$

$$\sqrt{J(J+1)} = \omega (\mathcal{J}_0 + 2 C \omega^2 + 3 D \omega^4 + 4 F \omega^6 + \dots). \quad (2.8 \text{ ii})$$

Introduction of higher order terms leads to additional free parameters. Although Harris only applied his model to (even-even) rotational nuclei, his method yields reasonable results for many even-even transitional nuclei as well.

## II VMI Model of Mariscotti, Scharff-Goldhaber and Buck

### 1. Outline of the model

In 1969 Mariscotti, Scharff-Goldhaber and Buck proposed their now famous variable moment of inertia (VMI) model (MSB 69). It is a two-parameter phenomenological model for energy levels and transition rates of the ground state band of even-even nuclei. It is valid for rotational nuclei as well as those transitional nuclei for which  $E_4/E_2 \geq (10/3)^{2/3} = 2.23$ . The application of the model can be extended to bands other than the ground state band. The conventional statement of the model is given below. The excitation energies are

$$E_J = \frac{J(J+1)}{2\mathcal{J}_J^{(S)}} + \frac{1}{2} C (\mathcal{J}_J^{(S)} - \mathcal{J}_0^{(S)})^2 \quad (2.9 \text{ i})$$

For each angular momentum  $J$ , the moment of inertia is determined by the equilibrium condition

$$\left. \frac{dE_J}{dJ(J+1)} \right|_{J(J+1)} = 0. \quad (2.9 \text{ ii})$$

Under certain circumstances there can arise ambiguities connected with the statement of the model given above. As a result a more mathematical statement of the model will be given in Chapter 4, Section VIII.

In the original VMI paper (MSB 69), the above formula was least squares fitted to 88 even-even rotational and transitional nuclei. The results were excellent. It was also shown by Mariscotti et.al. that the VMI model is mathematically equivalent to the two parameter Harris model (Har 64).

## 2. Conventional plot of data

A group of Stockholm nuclear physicists have developed a convenient graphical method (JRS 71) for plotting the energy level data of rotational bands. In analogy with Harris (Har 64) they define an "angular velocity"  $\omega$  as

$$\hbar\omega = \frac{dE}{dJ(J+1)}. \quad (2.10 \text{ i})$$

Also they define the effective moment of inertia as

$$\frac{2J}{\hbar^2} = \left( \frac{dE}{dJ(J+1)} \right)^{-1} \quad (2.10 \text{ ii})$$

Equations (2.10) together imply that

$$\hbar\sqrt{J(J+1)} = J\omega. \quad (2.11)$$

Since the energy is experimental and is known only for discrete

values of the angular momenta, it is necessary to evaluate the differentials in equation (2.10) according to some finite difference interpolation procedure. The Stockholm procedure yields the following relations:

$$(\hbar\omega_J)^2 = \frac{J^2 - J + 1}{(2J - 1)^2} (\Delta E_J)^2 \quad (2.12)$$

$$\frac{2J}{\hbar^2} = \frac{2(2J - 1)}{\Delta E_J} \quad (2.13)$$

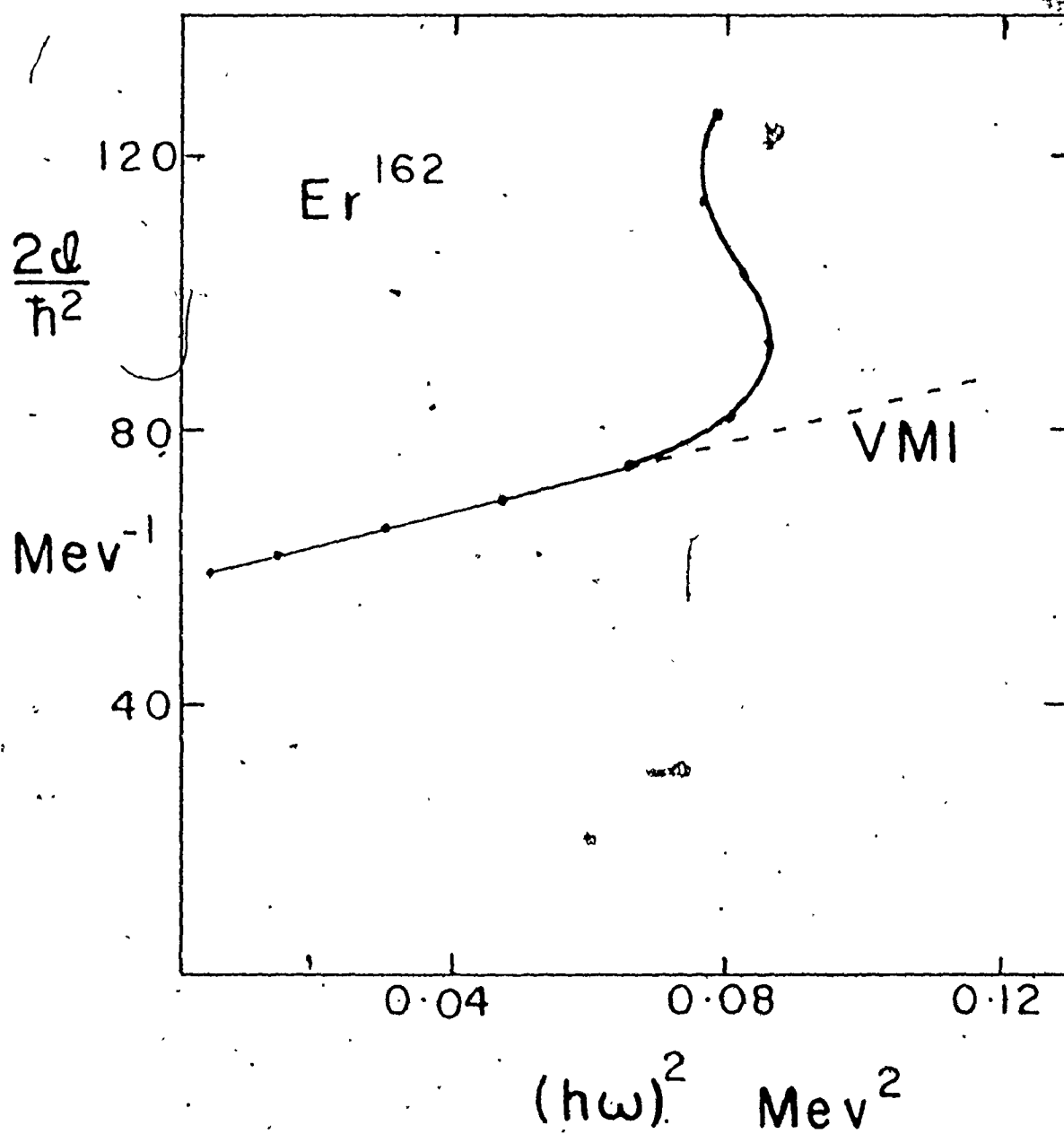
$$\Delta E_J = E_J - E_{J-2} \quad (2.14)$$

These definitions of  $J$  and  $\omega$  will be used in this work. Sorenson, in a review article (Sor 73), has discussed other possible definitions. In the conventional method of displaying the data,  $2J/\hbar^2$  is plotted as a function of  $(\hbar\omega)^2$  for each available energy level. An example of such a plot is given in Figure 2.1.

Several features of the  $J$ - $\omega^2$  plot should be noted. First, energy transitions rather than energy levels are displayed. This affords close contact with the data since what is measured is the energy of the gamma ray emitted during the transition. Second, each measured level (assuming all the lower levels are known) results in exactly one point on the plot. Third, the shape of the plotted curve is very sensitive to the data. Fourth and most important, the predictions of the



Figure 2.1



$J-\omega^2$  plot of Er<sup>162</sup> data. The straight line represents the prediction of the Variable Moment of Inertia model

VMI model on this kind of a plot yield approximately a straight line. This statement will be substantiated in Chapter 4, Section VIII. It is a remarkable achievement for the VMI model (likewise the two parameter Harris model) that the data for  $\text{Er}^{162}$  lies very close to a straight line for angular momentum as high as  $J = 12$ .

### III Backbending

In  $\text{Er}^{162}$  the level spacing  $\Delta E_J$  increases steadily with  $J$  until  $J$  reaches 14. At this point the level spacing suddenly decreases; that is  $\Delta E_{J=16} < \Delta E_{J=14}$ . For yet higher angular momentum, the level spacing resumes increasing. When  $E_J$  is plotted as a function of  $\sqrt{J(J+1)}$ , this change in  $\Delta E_J$  is not readily apparent. However on an  $\mathcal{J}-\omega^2$  plot, the change is quite dramatic. For large  $J$ ,  $\omega_J = \frac{1}{2} \Delta E_J$ . As a result, a decrease in  $\Delta E_J$  causes a decrease in  $\omega_J$  and a resulting sudden increase in  $\mathcal{J}_J$  (see equation (2.11)). This effect was first observed in 1972 by A. Johnson, H. Ryde and S. A. Hjorth (JRH 72). Some of their data is shown in Figure 2.1. They called this effect backbending.

This discovery caused considerable excitement. The interesting fact was not that  $\omega$  decreased but that the moment of inertia suddenly increased. Long before any such experiments were attempted, Mottelson and Valatin (MV 60) had predicted at sufficiently high spin all pairing correlation should disappear and the moment of inertia would increase rapidly

to the rigid rotor value. They predicted that this effect should occur at  $J_c = 12$  for mass number  $A = 180$ . This deduced effect was called the Coriolis anti-pairing (CAP) effect. At present the true cause of backbending is not absolutely known. It is clear, however, that backbending nuclei undergo a sudden change at a critical angular momentum  $J_c$ .

Since the pioneering work of Johnson et.al. (JRH 72), over a dozen nuclei have been found which exhibit backbending in the ground state band. Most of these nuclei are in the rare earth region of the periodic table. A few nuclei also show backbending in the  $\beta$ -band (WGG+ 73, KBB+ 73, AWG+ 74, LBD+ 74).

One theoretical approach to explain backbending was to generalize the VMI model. Das and Banerjee (DB 73) have substituted for the original potential energy term a more general term

$$V(J) = \sum_{n=2}^4 c_n J^{(S)} - J_0^{(S)} J^{(S)n/n!} \quad (2.15)$$

By least squares fitting the four parameters  $J_0$ ,  $c_2$ ,  $c_3$  and  $c_4$  to the data, backbending curves were produced. A fourth degree polynomial was chosen because this is the lowest order polynomial for which backbending is possible.

There is no reason why higher order terms could not be used. In fact Thieberger (Thi 72) has given a prescription for obtaining the appropriate VMI potential to fit any data (provided data does not show "downbending"). (Downbending describes a phenomenon in which the moment of inertia  $J$  decreases

With increasing angular momentum  $J$ .) The Thieberger prescription is described and utilized in Chapter 4, Section VIII. The fact that the VMI model can describe almost any level scheme has been used to criticize the model. It has been said that the model is just an alternative statement of the data. Perhaps this is true for the generalized VMI model. However the original two parameter formulation gives very good results for  $J < 10$ . It is a challenge to understand why this is so.

It has already been stated that Mariscotti et.al. proved the equivalence of the original VMI model to the two parameter Harris model. Klein, Dreizler and Das (KDD 70) have proved that the generalized VMI model is equivalent to the Harris model if taken to all orders. However this proof can be used only if  $\omega$  and  $J$  are monotonic functions of  $J$ . In the case of backbending,  $\omega$  is not monotonic. As a result the two models are equivalent only if there is no backbending (or downbending). The VMI model can reproduce backbending whereas the generalized Harris model cannot.

#### IV Theoretical Justification of the VMI Model

There have been several attempts to justify the VMI model on theoretical grounds. Das et.al. (DDK 71) and Volkov (Vol 71) have presented similar justifications based on the quantum-mechanical variational principle. A variational argument will be given here because it is suggestive as to how the VMI model can be extended. This argument will consider

only the ground state band although this limitation is not necessary.

As in the collective model, it is assumed that the Hamiltonian can be broken into an intrinsic vibrational part  $H_0$  and a rotational part. We take

$$H = H_0 + \sum_{v=1}^3 H_v \hat{J}_v^2. \quad (2.15)$$

The operators  $\hat{J}_r$  are the angular momentum operators about the body-fixed axes which, in the most general case, are defined as the principal axes of the asymmetric system. Assuming the validity of the Hamiltonian in equation (2.15), a trial wavefunction may be written:

$$\psi_J(\{\alpha_i\}) = \sum_{K=0}^J A_K(\{\alpha_i\}) \phi_{MK}^J(\theta_1, \theta_2, \theta_3) \quad (2.16)$$

where

$$\phi_{MK}^J(\theta_1, \theta_2, \theta_3) = \sqrt{\frac{2J+1}{16\pi^2(1+\delta_{K0})}} \times (D_{MK}^J(\theta_1, \theta_2, \theta_3) + (-1)^J D_{M-K}^J(\theta_1, \theta_2, \theta_3)). \quad (2.17)$$

The summation in equation (2.16) is over even  $K$  only. This wavefunction embodies the  $A$  representation of the  $D_2$  group. (See Appendices A, B.) The set  $\{\alpha_i | i = 1, 2, \dots, N\}$  labels the variational parameters. They represent any change in the intrinsic state within a band. For example, they could represent shape co-ordinates, pairing gaps, etc.

We now define the expectation value

$$W_0(\{\alpha_i\}) = \langle \psi_{J=0}(\{\alpha_i\}) | H | \psi_{J=0}(\{\alpha_i\}) \rangle \quad (2.18)$$

$$= \langle A_{K=0}(\{\alpha_i\}) | H_0 | A_{K=0}(\{\alpha_i\}) \rangle \quad (2.19)$$

The ground state energy  $E_0$  is obtained by minimizing  $W_0(\{\alpha_i\})$  with respect to the variational parameters  $\{\alpha_i\}$ . Thus we define the location of the  $J=0$  minimum,  $\{\alpha_i(0)\}$ , by

$$\left. \frac{\partial W_0(\{\alpha_i\})}{\partial \alpha_n} \right|_{\{\alpha_i(0)\}} = 0 \quad n = 1, 2, \dots, N \quad (2.20)$$

The ground state  $J=0$  must have  $K=0$ . We assume the intrinsic state varies slowly with  $J$ . Hence the higher  $K$  components must be small:

$$A_K(\{\alpha_i(0)\}) = 0 \quad \text{if } K \neq 0 \quad (2.21)$$

and

$$\left. \frac{\partial A_K(\{\alpha_i\})}{\partial \alpha_n} \right|_{\{\alpha_i(0)\}} = 0 \quad n = 1, 2, \dots, N \quad (2.22)$$

• The respective values of the energies of the excited states are

$$W_J(\{\alpha_i\}) = \langle \psi_J(\{\alpha_i\}) | H | \psi_J(\{\alpha_i\}) \rangle \quad (2.23)$$

$$= \sum_{K, K'=0}^J \langle A_K(\{\alpha_i\}) | H_0 | A_{K'}(\{\alpha_i\}) \rangle \quad (2.24)$$

$$+ \sum_{v=1}^3 \left( \sum_{K, K'=0}^J \langle A_K(\{\alpha_i\}) | H_v | A_{K'}(\{\alpha_i\}) \rangle \langle \phi_{MK}^J | \hat{J}_v^2 | \phi_{MK'}^J \rangle \right)$$

The excited state energy  $E_J$  is obtained by minimizing  $W_J(\{\alpha_i\})$ .

That is

$$E_J = \min(W_J(\{\alpha_i\})) - E_0 \quad (2.25)$$

The location of the minimum,  $\{\alpha_i(J)\}$ , is determined by

$$\left. \frac{\partial W_J(\{\alpha_i\})}{\partial \alpha_n} \right|_{\{\alpha_i(J)\}} = 0 \quad n = 1, 2, \dots, N. \quad (2.26)$$

Assuming that the minimum in parameter space is a function of  $J$ , we can expand

$$\begin{aligned} E_J = & \sum_{m,n=1}^N \frac{a_{mn} (\alpha_m(J) - \alpha_m(0)) (\alpha_n(J) - \alpha_n(0))}{2I} + \dots \\ & + \sum_{v=1}^3 \left( \sum_{K,K'=0}^J \langle A_K(\{\alpha_i(J)\}) | H_v | A_{K'}(\{\alpha_i(J)\}) \rangle \right. \\ & \times \left. \langle \phi_{MK}^J | \hat{J}_v^2 | \phi_{MK'}^J \rangle \right). \end{aligned} \quad (2.27)$$

The first order terms in  $\alpha_n(J) - \alpha_n(0)$  vanish because of equations (2.20), (2.21) and (2.22). If it is assumed that the Hamiltonian is axially symmetric, i.e.  $H_1 = H_2 = H_+$ , then the ground state band must be pure  $K = 0$ . This causes equation (2.27) to simplify to

$$\begin{aligned} E_J = & \sum_{m,n=1}^N a_{mn} \frac{(\alpha_m(J) - \alpha_m(0)) (\alpha_n(J) - \alpha_n(0))}{2I} + \dots \\ & + \langle A_{K=0}(\{\alpha_i(J)\}) | H_+ | A_{K=0}(\{\alpha_i(J)\}) \rangle J(J+1) \end{aligned} \quad (2.28)$$

However, to derive the ordinary VMI model, it is not necessary to make this assumption. Instead we define the quantity  $\mathcal{J}_J^{(S)}$  by requiring

$$\frac{J(J+1)}{2J^{(S)}} = \sum_{v=1}^3 \left( \sum_{K, K'=0}^J \langle A_K(\{\alpha_i(J)\}) | H_v | A_{K'}(\{\alpha_i(J)\}) \rangle \right. \\ \left. \times \langle \phi_{MK}^J | \hat{J}_v^2 | \phi_{MK'}^J \rangle \right). \quad (2.29)$$

For each  $J$  there is a point in parameter space  $\{\alpha_i(J)\}$  corresponding to the minimum of  $W_J(\{\alpha_i\})$ . The quantity  $J_J^{(S)}$  defined by equation (2.29) also depends on  $J$ . Hence it is possible to consider  $J^{(S)}$  as a function of  $\{\alpha_i\}$ . That is,

$$J_J^{(S)} = f(\{\alpha_i(J)\}) \quad (2.30)$$

For our purposes it is necessary to assume that  $J_J^{(S)}$  is a monotonically increasing function of  $J$ . Experimentally it is seen that this assumption is valid except in the case of downbending. This is not a severe limitation. As a result, equation (2.30) can be inverted to yield the vector function  $\vec{g}(J^{(S)})$  with components defined as

$$\alpha_i(J) = g_i(J_J^{(S)}) \quad i = 1, 2, \dots, N. \quad (2.31)$$

Expanding  $g(J_J^{(S)})$  in a Taylor series about  $J_0^{(S)}$  we obtain

$$\alpha_i(J) - \alpha_i(0) = \left. \frac{dg_i(J^{(S)})}{dJ^{(S)}} \right|_{J_0^{(S)}} \times (J_J^{(S)} - J_0^{(S)}) + \dots \quad (2.32)$$

Upon substitution of equations (2.32) and (2.29) into equation (2.27), the following simple equation is obtained:

$$E_J = \frac{J(J+1)}{2J^{(S)}} + C_2 (J_J^{(S)} - J_0^{(S)})^2 + \dots \quad (2.33)$$



where

$$C_2 = \frac{1}{2!} \sum_{m,n=1}^N (a_{mn} \left. \frac{dg_m(\mathcal{J}(S))}{d\mathcal{J}(S)} \right|_{\mathcal{J}_0(S)} \frac{dg_n(\mathcal{J}(S))}{d\mathcal{J}(S)} \Big|_{\mathcal{J}_0(S)}) \quad (2.34)$$

The locations of the energy minima  $\mathcal{J}_i(J)$  for  $J = 0, 2, 4$  etc. lie along a path in the  $N$ -dimensional parameter space. The quantity  $\mathcal{J}(S)$  is a monotonically increasing function of the distance along that path as  $J$  increases from 0. Thus the  $\{\alpha_i(J)\}$  can be considered to be implicit functions of  $\mathcal{J}(S)$  and these  $N$  variational parameters  $\{\alpha_i\}$  have been essentially replaced by a single quantity  $\mathcal{J}(S)$ . This process is exact.

The VMI equilibrium condition is obtained by substituting equation (2.31) into equation (2.26). This yields

$$\left. \frac{dW_J(\mathcal{J}(S))}{d\mathcal{J}(S)} \right|_{\mathcal{J}_J(S)} = 0 \text{ for all } J. \quad (2.35)$$

Employing equation (2.25) we finally obtain the condition

$$\left. \frac{dE_J}{d\mathcal{J}(S)} \right|_{\mathcal{J}_J(S)} = 0 \text{ for all } J. \quad (2.36)$$

This completes the justification for the ordinary VMI model.

In this model a single co-ordinate  $\mathcal{J}$  describes the change of the intrinsic structure within the band. However there is no reason why just one co-ordinate must be used. A natural choice would be to take the three moments of inertia about the three body-fixed axes as co-ordinates. Using this suggestion and working in analogy to equation (2.29) we define three moments of inertia by

$$R_J(J_1^J, J_2^J, J_3^J) = \sum_{v=1}^3 \left( \sum_{K, K'=0}^J \langle A_K(\{\alpha_i(J)\}) | H_v | A_{K'}(\{\alpha_i(J)\}) \rangle \right. \\ \left. \times \langle \phi_{MK}^J | \hat{J}_v^2 | \phi_{MK'}^J \rangle \right) \quad (2.37)$$

where  $R_J(J_1^J, J_2^J, J_3^J)$  is the lowest eigenvalue of the operator

$$R = \sum_{v=1}^3 \frac{\hat{J}_v^2}{2J_v^J}$$

for a wavefunction in the A representation of the  $D_2$  group with angular momentum J. Equation (2.37) does not uniquely define the quantities  $J_1^J$ ,  $J_2^J$  and  $J_3^J$  but this does not matter. It is clear that these quantities are not unique because equation (2.29) must be a special case of equation (2.37). All that matters is that the quantities  $J_1^J$ ,  $J_2^J$  and  $J_3^J$  do not change too rapidly with J so that an appropriate inversion and Taylor series expansion can be made.

An inversion analogous to equation (2.31) is performed to give the relations

$$\alpha_i(J) = g_i(J_1^J, J_2^J, J_3^J) \quad (2.38)$$

After substitution of equations (2.37) and (2.38) into equation (2.27) a "three-dimensional" VMI equation is obtained:

$$E_J = R_J(J_1^J, J_2^J, J_3^J) + \sum_{\mu, \nu=1}^3 \frac{C_{\mu\nu}}{2!} (J_\mu^J - J_\mu^0) (J_\nu^J - J_\nu^0) + \dots \quad (2.39)$$

where  $C_{\mu\nu}$  can be obtained easily. The equilibrium conditions for each  $J$  become

$$\left. \frac{E_J(J_1, J_2, J_3)}{\partial J_\nu} \right|_{(J_1^J, J_2^J, J_3^J)} = 0 \quad \nu = 1, 2, 3 \quad (2.40)$$

Equations (2.39) and (2.40) have not been used to study nuclei. Instead a model intermediate to the ordinary VMI and the "three-dimensional" VMI has been used. This model will be described in the next section.

#### V. An Axially Asymmetric VMI Model

A "two-dimensional" VMI type model (SV 73) has been developed and applied to several nuclei. Two co-ordinates based on a volume conserving hydrodynamical model (Boh 52) are employed to describe changes in the intrinsic wavefunction. The first co-ordinate  $\gamma$  describes the amount of axial asymmetry of the nuclear shape. A second co-ordinate  $\rho^{(A)}$ , instead of the traditional  $\beta$ , describes all other aspects of the change in the intrinsic wavefunction.

The starting point of the model is the three moments of inertia from the collective quadrupole model originally given by A. Bohr (Boh 52):

$$J_\nu = 4 B \beta^2 \sin^2(\gamma - \frac{2\pi}{3} \nu) \quad \nu = 1, 2, 3 \quad (2.41)$$

Note that  $\gamma$  determines the ratios of the three moments of inertia. The overall magnitude of the three moments of inertia is specified by the quantity  $J^{(A)}$  in the more general relation

$$J_v = \frac{4}{3} J^{(A)} \sin^2\left(\gamma - \frac{2\pi}{3} v\right) \quad v = 1, 2, 3. \quad (2.42)$$

Using these moments of inertia and following Davydov and Filippov (DF 58) the asymmetric rotor Hamiltonian is defined as (see Appendix B)

$$\hat{R} = \frac{3}{4} \frac{1}{2J^{(A)}} \sum_{v=1}^3 \frac{\hat{J}_v^2}{\sin^2\left(\gamma - \frac{2\pi}{3} v\right)}. \quad (2.43)$$

The lowest few eigenvalues of the operator  $\hat{R}$  are plotted as a function of  $\gamma$  in Figure 2.2. The rotor eigenvalues are symmetric about  $\gamma = \frac{\pi}{6}$  in the relevant range of  $0 \leq \gamma \leq \frac{\pi}{3}$ .

Two special cases are noted. In the case of axial symmetry ( $\gamma = 0$ ), the operator  $\hat{R}$  can be replaced by

$$\hat{R}_{\gamma=0} = \frac{1}{2J^{(A)}} (\hat{J}_1^2 + \hat{J}_2^2). \quad (2.44)$$

To avoid an infinite eigenvalue at  $\gamma = 0$ , the wavefunction must have  $K = 0$  since in this case the operator  $\hat{J}_3$  always has zero expectation value and thus  $\hat{J}_3$  can be omitted. The eigenvalues of  $\hat{R}_{\gamma=0}$  are the well known symmetric rotor energies

$$E_J = \frac{J(J+1)}{2J^{(A)}} \quad (2.45)$$

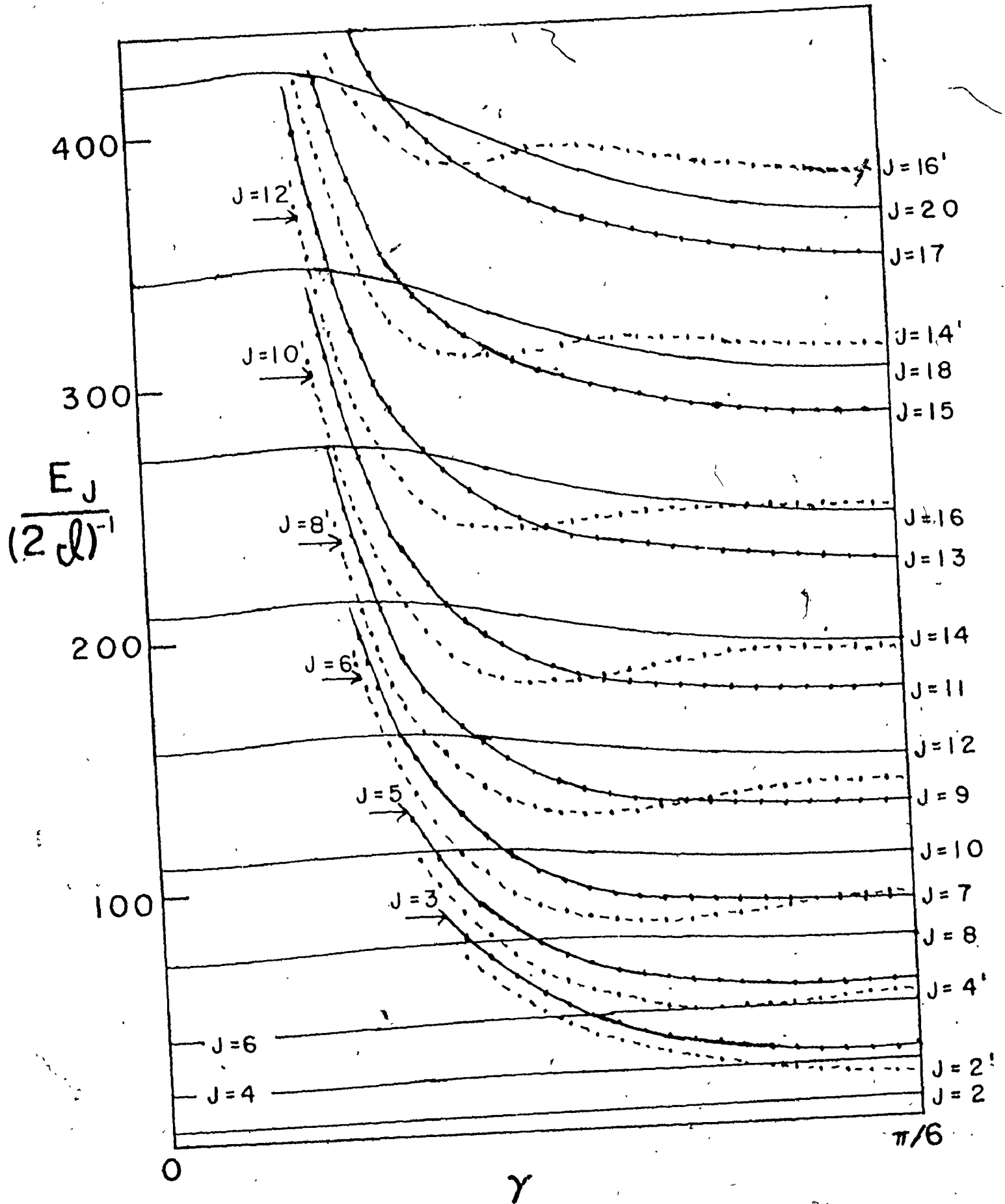
The second special case is that of maximal axial asymmetry ( $\gamma = \frac{\pi}{6}$ ). In this case the operator  $\hat{R}$  reduces to

$$\hat{R}_{\gamma=\pi/6} = \frac{3}{2J^{(A)}} \left( \frac{1}{4} \hat{J}_1^2 + \hat{J}_2^2 + \hat{J}_3^2 \right) = \frac{3}{2J^{(A)}} (\hat{J}^2 - \frac{3}{4} \hat{J}_1^2). \quad (2.46)$$

Despite the fact that the nuclear shape displays maximal

Energy levels of a rigid asymmetric rotor. These are the results of the Davydov-Filippov model.  $\gamma$  is the axial asymmetry parameter.

Figure 2.2



axial ~~asymmetry~~, the vector Hamiltonian for  $\gamma = \frac{\pi}{6}$  is actually axially symmetric about the 1-axis since  $J_2 = J_3$ .

As a result the wavefunction can be quantized with respect to the 1-axis and written in terms of a  $D_{MK}^J$  function. The eigenvalues of  $\hat{R}_{\gamma=\pi/6}$  are then simply


$$E_{JK_1} = \frac{3}{2J(A)} [J(J+1) - \frac{3}{4} K_1^2] . \quad (2.47)$$

For a given  $J$  the lowest, or so-called Yrast, level is obtained when  $K_1 = J$ :

$$E_{JJ} = \frac{1}{2J(A)} \frac{3}{4} J(J+4) . \quad (2.48)$$

Either by examining Figure 2.2 or by comparing equations (2.45) and (2.48) it can be seen that for  $J < 8$ , the energy is lowest when  $\gamma = 0$ . However for  $J = 8$  the axially symmetric and the maximal axially asymmetric systems have equal rotational energy. For  $J > 8$  the rotational energy favours a nucleus with a maximal asymmetric shape. This has important physical consequences in a more realistic case.

We now return to the construction of a new VMI type model. The symbol  $R_J(\gamma)$  is defined to be the lowest eigenvalue (consistent with angular momentum  $J$ ) of the operator  $2J(A)\hat{R}$  where  $\hat{R}$  is given in equation (2.43). In analogy with the two previous derivations the quantities  $J(A)$  and  $\gamma$  are determined by the condition



$$\frac{R_J(\gamma)}{2J_J^{(A)}} = \sum_{v=1}^3 \left( \sum_{K, K'=0}^J \langle A_n(\{\alpha_i(J)\}) | H_v | A_{K'}(\{\alpha_i(J)\}) \rangle \right. \\ \left. \times \langle \phi_{MK}^J | J_v^2 | \phi_{MK'}^J \rangle \right). \quad (2.49)$$

Then equation (2.49) is inserted into equation (2.27) and, after an appropriate functional inversion the equation

$$E_J = \frac{R_J(\gamma)}{2J_J^{(A)}} + \frac{1}{2} C (J_J^{(A)} - J_O^{(A)})^2 + D (J_J^{(A)} - J_O^{(A)}) \gamma_J \\ + \frac{1}{2} E \gamma_J^2 + \text{higher order terms} \quad (2.50)$$

is obtained. The equilibrium conditions become

$$\left. \frac{\partial E_J}{\partial J_J^{(A)}} \right|_{J_J^{(A)}} = 0 \quad (2.51)$$

and

$$\left. \frac{\partial E_J}{\partial \gamma} \right|_{\gamma_J} = 0 \quad (2.52)$$

To avoid confusion, this model will be called the asymmetric VMI model (VMIA). The model of Mariscotti et al (MSB 69), with perhaps a more general potential  $V(J)$ , will be called the symmetric VMI model (VMIS). Again it should be emphasized that the quantity  $J^{(A)}$  represents not only centrifugal stretching but also microscopic degrees of freedom.

## VI. Results of VMIA Model for Ground State Band

To test this model, calculations have been performed for a pair of special cases. It is assumed that the "potential surface" can adequately be represented by a paraboloid. The higher order terms in equation (2.50) have been neglected.



The minimization implied in equations (2.51) and (2.52) is performed as follows. Eleven equally spaced values of  $\gamma$  are chosen. For each choice of  $\gamma$ , say  $\gamma_i$ , and for each  $J$ , the equation

$$\left. \frac{\partial E_J(J^{(A)}, \gamma_i)}{\partial J^{(A)}} \right|_{J=J^{(A)}} = 0 \quad i = 1, 2, \dots, 11 \quad (2.53)$$

is solved. Because of the simple potential surface employed, the derivative in equation (2.53) can be determined analytically. The resulting equation is solved numerically yielding the value for  $J_{ji}^{(A)}$  appropriate for the choice  $\gamma_i$ .

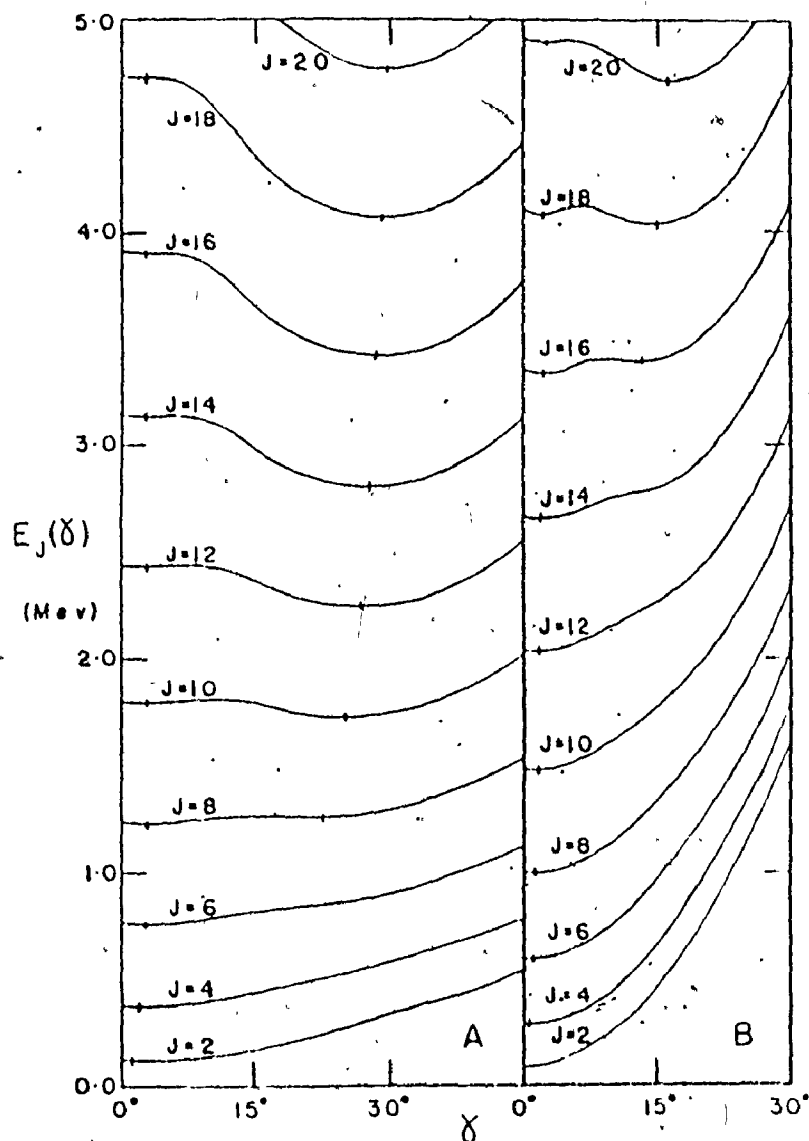
Now that  $J_{ji}^{(A)}$  is given as a function of  $\gamma_i$  it is possible to define a new function of  $\gamma_i$ :

$$E_J(\gamma_i) = E_J(J_{ji}^{(A)}, \gamma_i) \quad (2.54)$$

where  $J_{ji}^{(A)}$  is the root of equation (2.53). A suitable interpolation procedure is used to define a continuous function  $E_J(\gamma)$  based on  $E_J(\gamma_i)$ . The function  $E_J(\gamma)$  is plotted in Figure 2.3 for two choices of the set of parameters  $\{\sqrt{V_0}^{(A)}, C, D, E\}$  as defined in equation (2.50). The interpolation procedure used to determine  $E_J(\gamma)$  from  $E_J(\gamma_i)$ ,  $1 \leq i \leq 11$ , makes use of spline functions (see Appendix D). This functional fit to  $E_J(\gamma)$  allows an analytic determination of the minimum of  $E_J(\gamma)$  with respect to  $\gamma$ .

The minima in Figure 2.3 represent the solutions

Figure 2.3

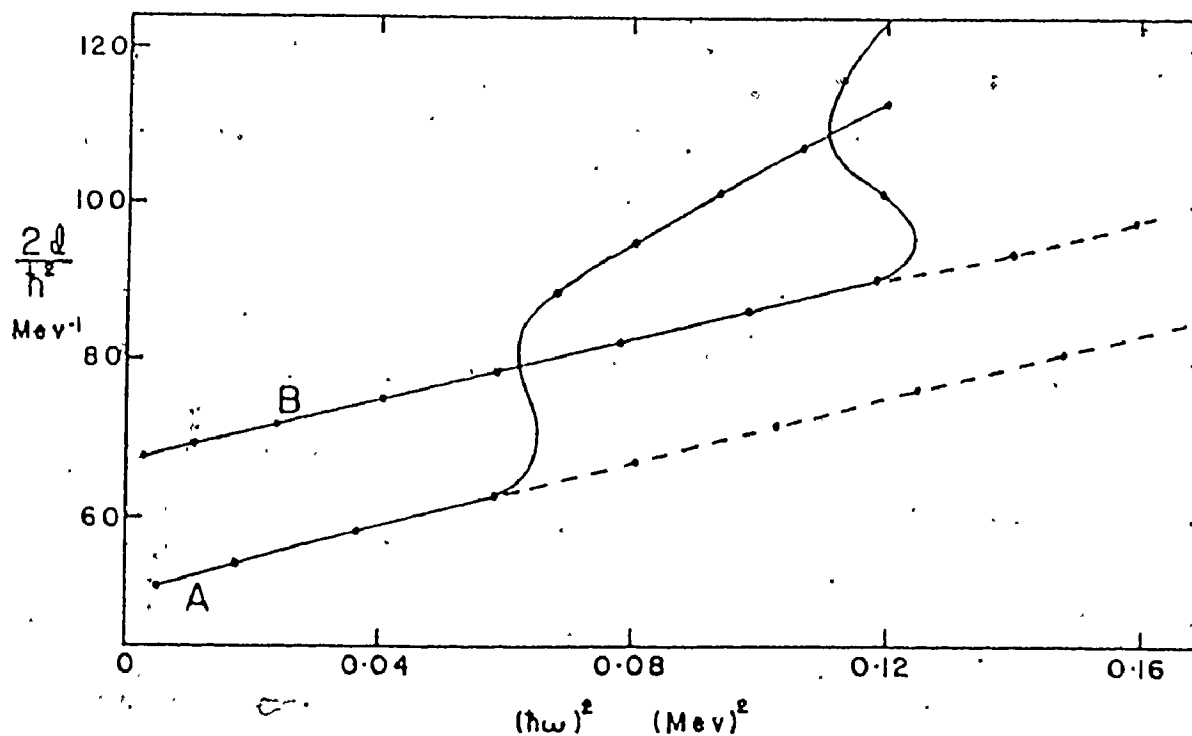


Energy levels of the VMIA model. Rotational energies as a function of the asymmetry parameter  $\gamma$ . Case A illustrates a  $\gamma$  "soft" nucleus and case B a relatively  $\gamma$  "hard" nucleus. Minima which represent VMIA solutions are marked on the figure.

of equations (2.50), (2.51) and (2.52) as determined by the variational procedure. Case A illustrates a  $\gamma$  "soft" nucleus, i.e. soft to asymmetric shape change, and case B a relatively  $\gamma$  "hard" nucleus. In case A for  $J \leq J_c = 8$  the prolate solution is obtained. However for  $J > J_c$  it is energetically favourable for the nucleus to become axially asymmetric. For case B the instability occurs at  $J_c = 16$ . For  $J \geq J_c$  there exists for each  $J$  a second minimum for which  $\gamma \approx 0$ . The transitions between these second minima as well as those between the absolute minima are plotted on an  $J-\omega^2$  plot in Figure 2.4. The change from axially symmetric to asymmetric results in backbending behaviour. On this plot the second minima appear as a straight line contribution of the curve for  $J \leq J_c$ . Since the original VMIS model predicts a straight line on the plot, those higher minima have been named the "VMIS solutions".

These "VMIS solutions" may have a physical interpretation in terms of "forking". Forking is a word introduced by G. Scharff-Goldhaber et al (SML+ 73) to describe some peculiar experimental results in  $\text{Pd}^{102}$  and  $\text{Pd}^{100}$ . Forking describes a phenomenon in which two rotational bands both feed with about equal intensity into a common lower band. What is interesting, is that the branch at lower energy displays backbending whereas the branch at higher energy follows the VMIS curve (on an  $J-\omega^2$  plot). Subsequently the Scharff-Goldhaber et al paper was shown to be in error (GGR+ 74). However since then two other cases of forking have been ob-

Figure 2.4



$\mathcal{I}\omega^2$  plot of the energy levels of the VMIA model. These are the same two cases as in Figure 2.3. The broken lines show the higher energy "VMIS" solutions ( $\gamma \approx 0$ ) while the backbending part of the solid line shows the Yrast asymmetric solutions.

served: one in  $\text{Ba}^{126}$  (FCS+ 74) and the other in  $\text{Os}^{186}$  (WBB+ 73). The data from these two nuclei are given in Figure 2.5. The fact that the "forked" state follows along the straight line lends credence to its interpretation in terms of the VMIA model.

In Figure 2.4 the  $\omega^2$  curves resume a steady rise after the backbending point. This is in contrast to the data. However this is due to the fact that a parabolic potential surface has been chosen. The results of a more realistic potential are given in Figure 2.6.

#### VII The VMIA Model and the Gamma Band

In the Davydov-Filippov model (DF 58) the lowest eigenvectors of the rotor Hamiltonian for odd  $J$ 's and the second lowest eigenvectors for even  $J$ 's form a sequence of states interpreted as the  $\gamma$ -band. From Figure 2.2 it can be seen that for  $\gamma = \pi/12$  these levels,  $J = 2', 3, 4', 5, 6'$  etc, have a reasonably regular energy spacing. The  $\gamma$ -band can also be incorporated into the VMIA model.

Since the justification of this model is based on the quantum-mechanical variational principle, some complications arise for the even angular momentum states. This is due to the fact that the lower even members of the  $\gamma$ -band are not Yrast states, i.e. there exist lower energy states of the same  $J$ . To obtain the ground state using the variational

$J-\omega^2$  plot of  $\text{Os}^{186}$  and  $\text{Ba}^{126}$  data showing forking. The dotted lines correspond to the higher energy "forked" state.

Figure 2.5

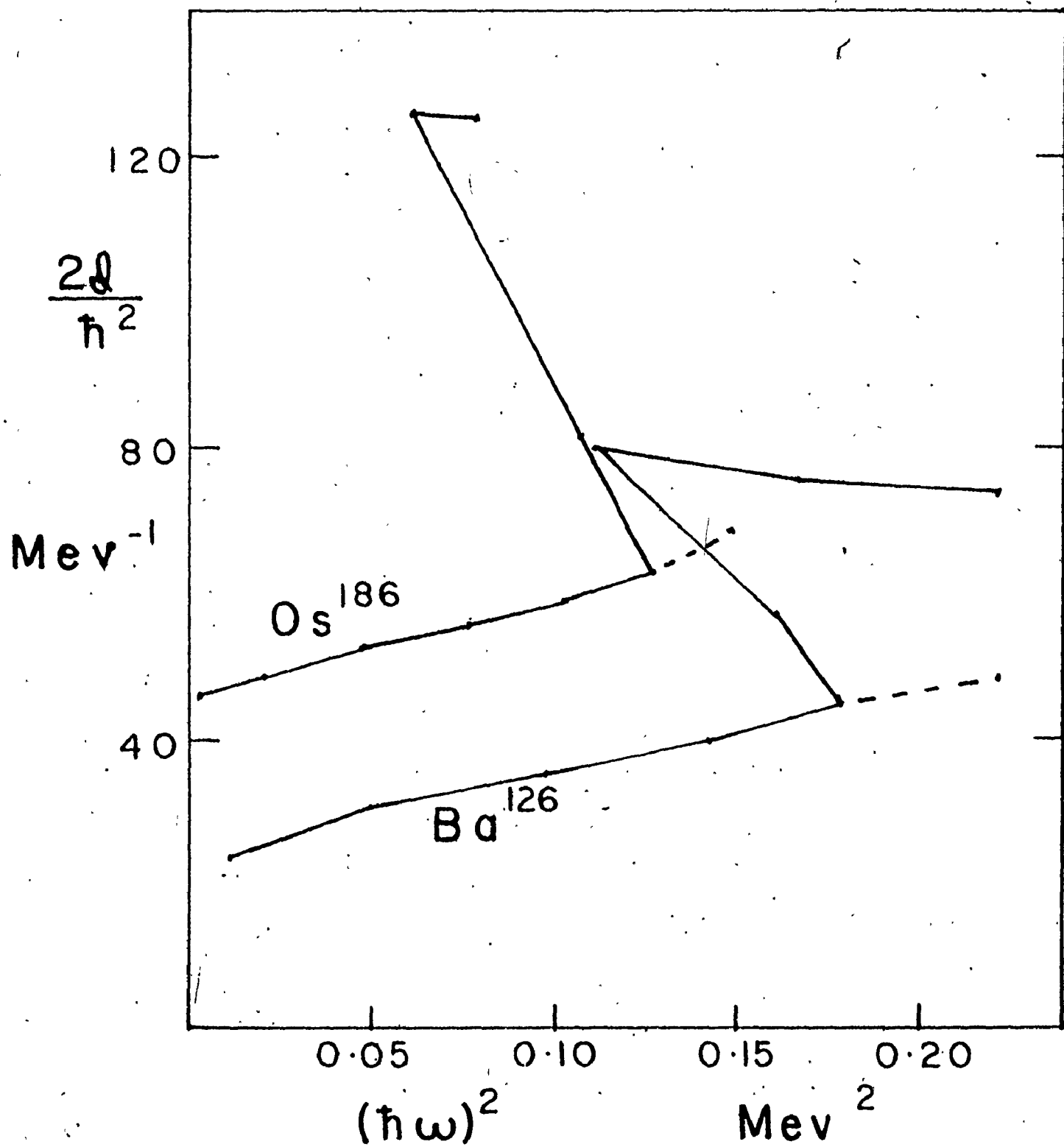
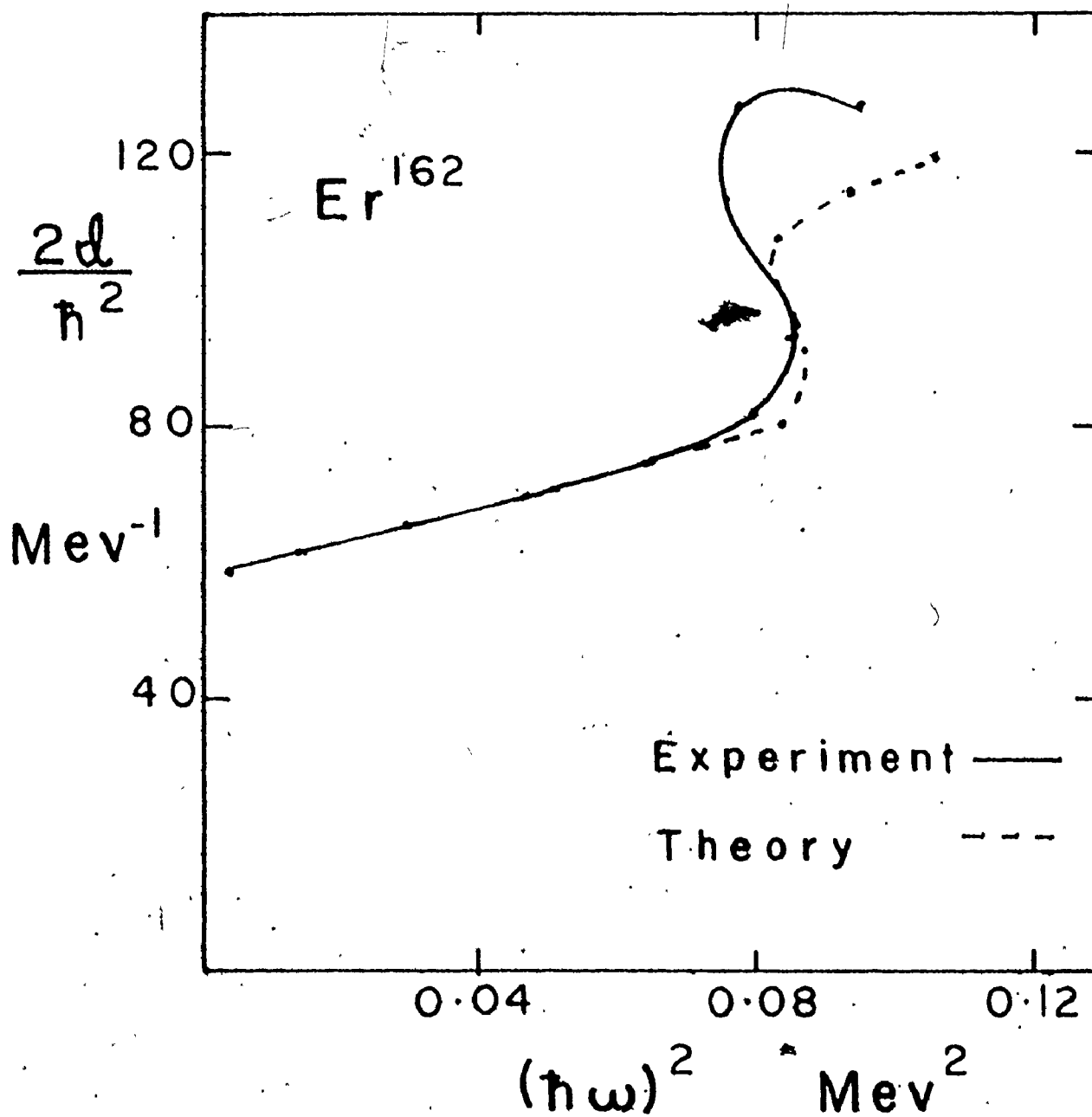


Figure 2.6



Energies of the VMIA model for  $\text{Er}^{162}$  on an  $\sqrt{-\omega^2}$  plot. The dotted line corresponds to the results of the VMIA model with a more complicated potential than the paraboloid given in equation (2.50).



principle, the class of trial wavefunctions is unrestricted except for requirements of normalization. However to obtain an excited state using the variational principle, it is necessary to ensure that each member of the class of trial wavefunctions is orthogonal to all the lower energy solutions of the Hamiltonian. In the case of an Yrast state, this orthogonality is guaranteed by the fact that states of different  $J$  have no overlap. On the other hand, for an even member of the  $\gamma$ -band, say  $J = 2$ , it must be ensured that each member of the class of trial wavefunctions are orthogonal to the state  $\psi_{J=2}$  of the ground state band.

The procedure used to obtain even  $J$  states is as follows. First the equilibrium value of  $\gamma$  for the ground state member of angular momentum  $J$  is obtained. This value of  $\gamma$ , written as  $\gamma_J$ , is used in defining the operator  $\hat{R}$  of equation (2.43). Then all the eigenvectors (with angular momentum  $J$ ) of the operator  $\hat{R}_{\gamma=\gamma_J}$  are calculated. These eigenvectors will be written  $\psi_{JM}^{(i)}(\gamma_J)$ ,  $i = 1, 2, \dots, N$  and  $N = J/2 + 1$ . Next the trial wavefunction

$$\psi_{J'M} = \sum_{i=2}^N a_i \psi_{JM}^{(i)}(\gamma_J) \quad (2.55)$$

is formed. The quantities  $a_i$  represent the variational parameters. It is now guaranteed that for any choice of  $a_i$ ,  $\psi_{J'M}$  is orthogonal to  $\psi_{JM}^{(i)}(\gamma_J)$ . To ensure normalization we require

$$\sum_{i=2}^N |a_i|^2 = 1. \quad (2.56)$$

The variational condition is

$$\delta \langle \psi_{J,M} | \hat{R}_Y | \psi_{J,M} \rangle = 0 \quad (2.57)$$

subject to equation (2.56). Substituting equation (2.55) into equation (2.57) we obtain

$$\delta \sum_{i,j=2}^N a_i a_j \langle \psi_{JM}^{(i)}(\gamma_J) | \hat{R}_Y | \psi_{JM}^{(j)}(\gamma_J) \rangle = 0 \quad (2.58)$$

subject to equation (2.56). Equations (2.56) and (2.57) are combined using a Lagrange multiplier to yield

$$\sum_{j=2}^N \langle \psi_{JM}^{(i)}(\gamma_J) | \hat{R}_Y | \psi_{JM}^{(j)}(\gamma_J) \rangle a_j - E a_i = 0$$

$$i = 2, 3, \dots, N. \quad (2.59)$$

Defining

$$b_i = a_{i+1}, \quad i = 1, 2, \dots, N-1 \quad (2.60)$$

and

$$R_{ij}^T = \langle \psi_{JM}^{(i+1)}(\gamma_J) | \hat{R}_Y | \psi_{JM}^{(j+1)}(\gamma_J) \rangle \quad (2.61)$$

equation (2.59) becomes the eigenvalue equation

$$\sum_{j=1}^{N-1} R_{ij}^T b_j = E b_i. \quad (2.62)$$

The procedure for the even members of the  $\gamma$ -band is now straight forward. From the eigenvectors  $\psi_{JM}^{(i)}(\gamma_J)$  the matrix  $\tilde{R}^T$  is formed using equation (2.61). Then the lowest eigenenergy,  $R_J(\gamma)$  of  $\tilde{R}^T$  is calculated. This energy depends

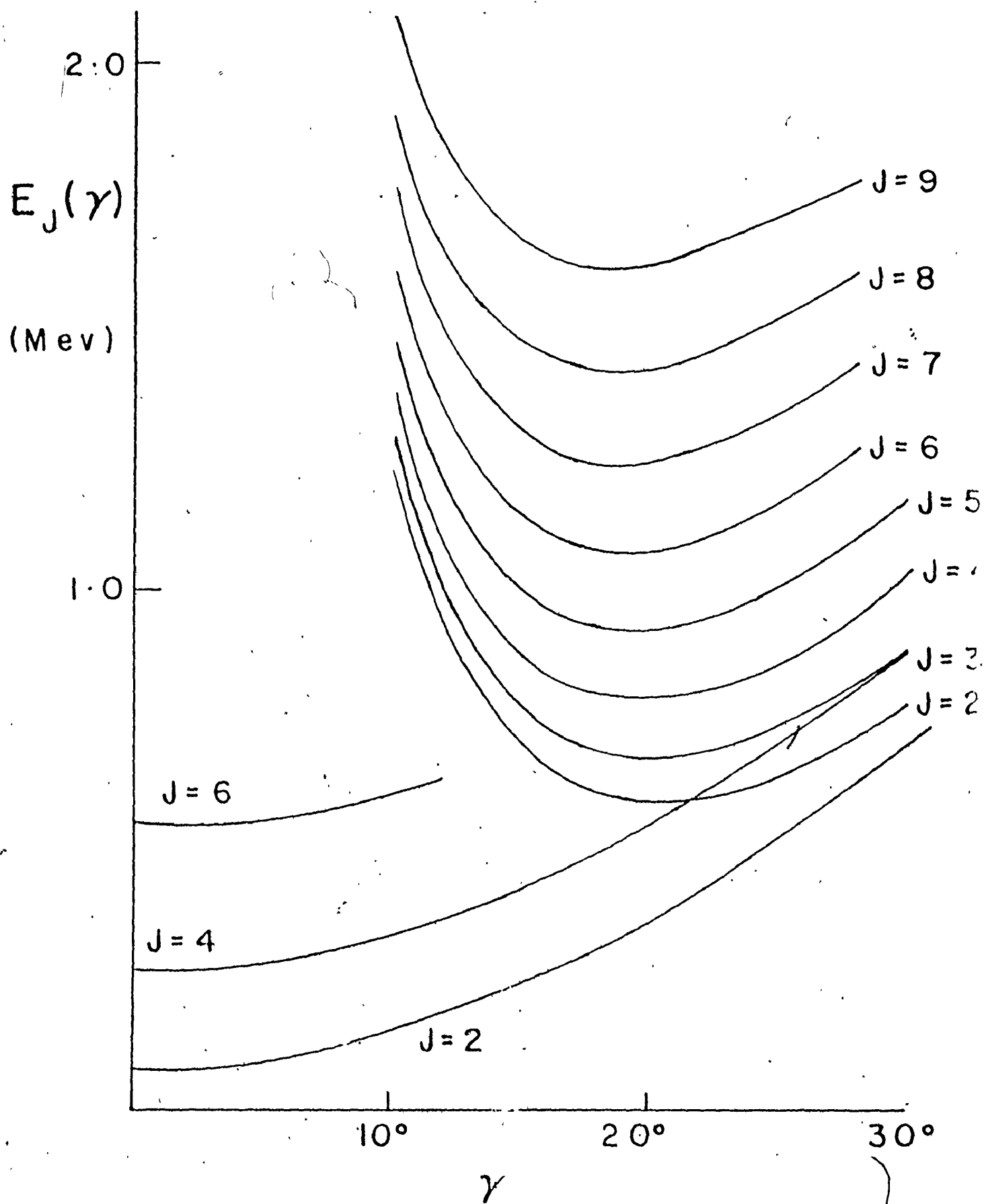
on  $\gamma$ . Finally  $R_{J_1}(\gamma)$  is substituted for  $R_J(\gamma)$  in equation (2.50). The conditions (2.51) and (2.52) give the equilibrium values  $\gamma_{J_1}^{(A)}$  and  $\gamma_{J_1}$ . In general  $\gamma_{J_1} \neq \gamma_J$ . Had it been true that  $\gamma_{J_1} = \gamma_J$  then the somewhat elaborate projection procedure outlined above would not be necessary. Instead the lowest eigenvector of  $\hat{R}_{\gamma_J}$  would represent the Yrast member and the second lowest eigenvector would represent the  $\gamma$ -band member. Orthogonality between the two states would be satisfied by virtue of the fact that the (non-degenerate) eigenvectors of a hermitian matrix are orthogonal. However, in general, the equilibrium values of  $\gamma$  for the Yrast and  $\gamma$  bands are different.

The energy levels resulting from this calculation are shown in Figure 2.7. The ordinate,  $E_J(\gamma)$ , is the same quantity as was plotted in Figure 2.3. However in the present case, both the  $\gamma$ -band and the lowest three members of the ground state band are plotted. The predicted energies are given by the minima of the curves. As in Figure 2.3, a parabolic potential energy surface was used. It is important to realize that the parameters appearing in the potential are the same for both the ground state band and the  $\gamma$ -band.

The VMIA model gives predictions for both the energy levels of the  $\gamma$ -band as well as the backbending behaviour of the ground state band. Moreover, the model predicts that the onset of backbending is sooner for the  $\gamma$  "soft" nuclei. The " $\gamma$  softness" of a nucleus can be determined quantitatively

Energy levels of the  $\gamma$  band from the VMIA model. The minima of these curves gives the equilibrium value of  $\gamma$  as in equation (2.52).

Figure 2.7



by measuring the energy of the  $\gamma$ -bandhead; the lower the  $\gamma$ -bandhead relative to the ground state band, the "softer" the nucleus with respect to  $\gamma$  deformation. The critical angular momentum,  $J_c$ , has been measured for several nuclei. This makes it possible to correlate  $J_c$  to  $\gamma$  "softness".

To do this an arbitrary unit of energy will be chosen, say  $E_0$ . It is then convenient to express moments of inertia in units of  $3/E_0$ . Then we can define

$$\bar{E}_J = E_J/E_0 \quad (2.63)$$

$$\bar{J}_J^{(A)} = J_J^{(A)} / (3/E_0) \quad (2.64)$$

$$\bar{J}_0^{(A)} = J_0^{(A)} / (3/E_0). \quad (2.65)$$

Then equation (2.50) can be written

$$\bar{E}_J = \frac{R_J(\gamma)}{6\bar{J}_J^{(A)}} + p(\bar{J}_J^{(A)} - \bar{J}_0^{(A)})^2 + q(\gamma - r(\bar{J}_J^{(A)} - \bar{J}_0^{(A)}))^2. \quad (2.66)$$

All the quantities in the above equation are dimensionless. The quantity  $q \geq 0$  is the  $\gamma$  softness parameter. For the extreme  $\gamma$  soft case,  $q = 0$  and the nucleus will backbend at  $J = 8$ .

To investigate the proposed correlation between backbending and  $\gamma$  softness,  $\bar{J}_0^{(A)}$ ,  $p$ , and  $r$  were given fixed values, whereas  $q$  was allowed to vary. To fit the data shown in Figure 2.8 the values chosen were


$$\bar{J}_0^{(A)} = 1, \quad p = 10, \quad r = 0.468$$

and

$$(2.67)$$

$$1.17 \leq q \leq 16.4$$

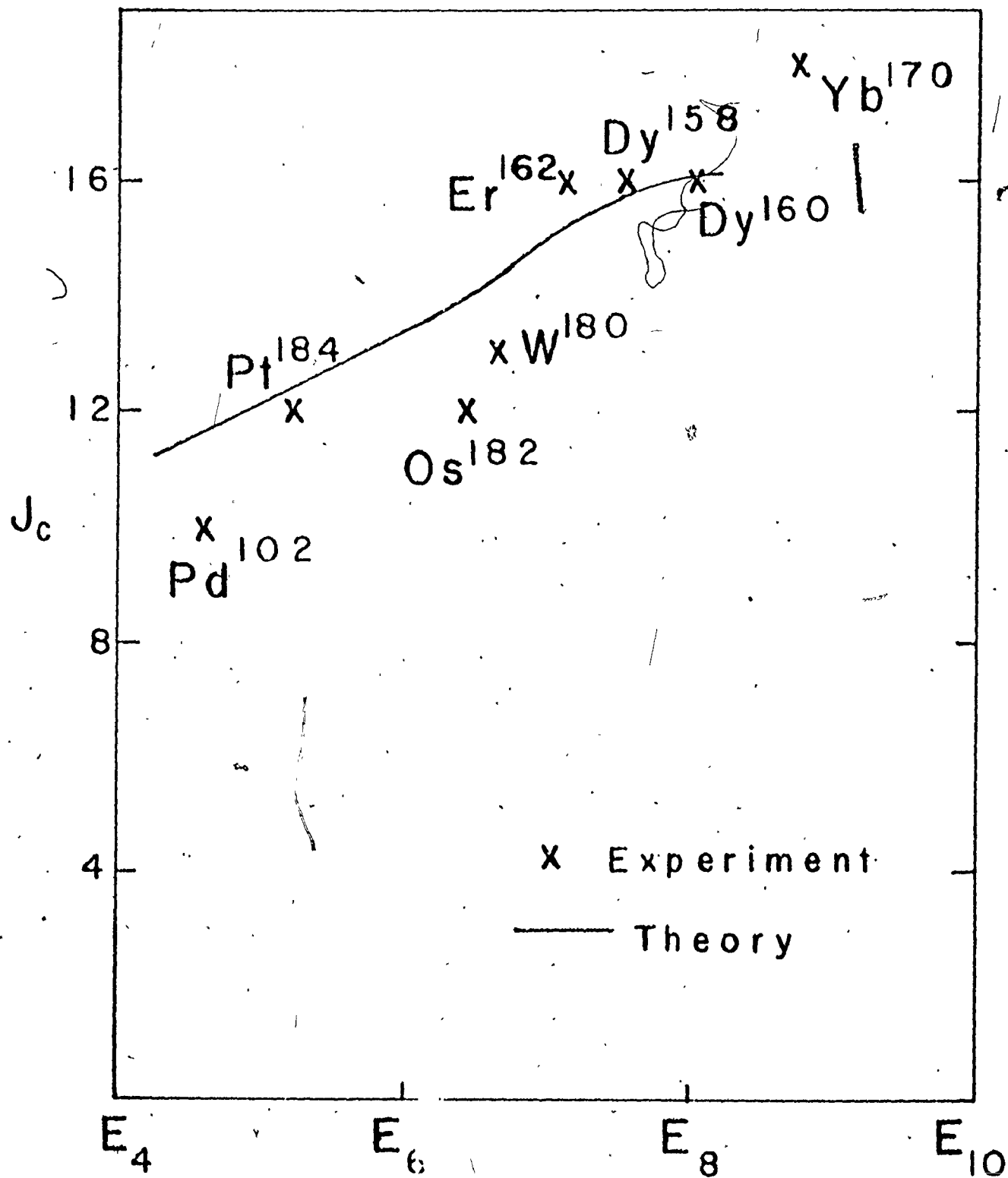
Each choice of values for  $\{\bar{J}_0^{(A)}, p, q, r\}$  was inserted into equation (2.66). This yields  $\bar{E}_J$ , for different values of  $J$ . From this sequence of energies, the critical angular momentum,  $J_c$ , as well as the  $\gamma$  "softness" (see caption to Figure 2.8) can be calculated. Then in Figure 2.8,  $J_c$  is plotted as a function of  $\gamma$  "softness". Each choice of  $q$  corresponds to a different point on the theoretical curve. The experimental  $J_c$  is plotted against the experimental  $\gamma$  "softness" on the same curve. Although there is considerable scatter, the proposed correlation does seem to be valid. It would be interesting to investigate whether or not microscopic theories give this result.



Correlation between critical angular momentum and "γ stiffness". On the vertical axis is plotted the critical angular momentum at which the nucleus either backbends or at least displays an irregularity in the  $J$  versus  $\omega^2$  curve. The energy of the  $\gamma$  bandhead relative to the ground state band energies is plotted on the horizontal axis.



Figure 2.8



## CHAPTER 3

### BOHR'S COLLECTIVE MODEL: THEORY

#### I. Introduction.

##### 1. Motivation

A collective model of nuclear rotations and vibrations was proposed by Aage Bohr (Boh 52) over two decades ago. The theory was refined in a subsequent paper (BM 53) co-authored by Ben Mottelson and in later papers. However it proved very difficult to solve the Schroedinger equation resulting from the model. As a result several simplifications to the model had to be made. Some of these theories have been described in Chapter 2.

Necessarily these simplified models lack some of the physics contained in the original Bohr-Mottelson collective model. This model treats rotations and vibrations on an equal footing whereas most subsequent models can handle one or the other type of motion but not both. The Bohr-Mottelson (B-M) model is able to treat rotational-vibrational coupling in a satisfactory manner. Moreover transitional nuclei can be treated in this framework. In addition the B-M model is fully quantum-mechanical. For example, zero-point motion is an important feature of this model. The B-M model is dynamic. It contains inertial as well as potential features.

The VMIA model proposed in Chapter 2 suggests that axial asymmetry is an important feature of nuclear structure at high spin. As a separate check on this prediction, the B-M model will be solved using a new numerical technique. Of crucial interest is the question of whether backbending can result in the B-M model.

## 2. Previous Attempts to Solve the Collective Hamiltonian

It has already been stated that the Bohr Hamiltonian is difficult to solve. It was not until about fifteen years after the model's inception that a proper solution for low spin states was given by Kumar and Baranger (KB 67). Using a numerical method they were able to solve the Schroedinger equation for states of angular momentum  $J = 0, 2, 3$  and  $4$ . Because the equation becomes successively more difficult to solve for the higher angular momenta, they were not able to go higher than  $J=4$ . Later Gneuss and co-workers (GMG 69, GG 71) using a different method were able to obtain solutions for  $J \leq 6$ . Subsequent solutions of the Bohr Hamiltonian generally have been based either on the method of Kumar and Baranger (K-B) or of Gneuss et al.

In the K-B method, the derivatives appearing in the Hamiltonian are treated numerically using finite difference methods. This approach leads naturally to a generalized matrix eigenvalue problem which is solved numerically. The method of Gneuss et al is quite different. The solution is

obtained by using a basis of five-dimensional harmonic oscillator functions. The matrix elements of the potential (in this basis) are calculated analytically using group theoretic techniques. Computer storage problems require that the size of the basis be limited. The allowed basis set is inadequate for  $J > 6$ .

Since these two prototype solutions, there has been considerable effort expended in extending the range of solutions. Of particular note is the work of Budnik and Seregin (BS 74). Using a method similar to that of Gneuss et al they have solved the Bohr collective Hamiltonian for  $J \leq 20$ . However they are limited to the Bohr inertial parameters and to simple collective potentials. Also they have not investigated the possibility of backbending in their model.

### 3. Outline of Method of Solution in This Work

In this chapter a completely general method of solving the Bohr Hamiltonian for  $J \leq 20$  is described. The limit  $J = 20$  was chosen for computational convenience. The method can be used for yet higher angular momentum states. The method is valid for arbitrary inertial functions and arbitrary potential surfaces. The method is based on that of Kumar and Baranger. For the higher angular momentum states, the Hamiltonian matrix becomes very large indeed (approximately  $1900 \times 1900$ ). This large a matrix has been made tractable by the resurrection of the Lanczos algorithm for obtaining a limited set of eigen-

values and eigenvectors of a matrix. The Lanczos algorithm is a relatively fast method of obtaining the extreme eigenvalues and eigenvectors of very large matrices. Since in many cases only the extreme eigensolutions are of physical interest, this method is a very useful tool in physics. In fact this method is the key to our solution of the Bohr Hamiltonian.

## II. Collective Model

### 1. Definition of Collective Co-ordinates

In the Bohr collective model, only the quadrupole modes of motion are considered. The monopole mode is neglected because it is normally at much higher energy due to the relative incompressibility of nuclear matter. The isoscalar dipole mode is forbidden because of conservation of linear momentum. The octupole modes have negative parity and so are orthogonal to the positive parity quadrupole modes. Isovector modes are normally ignored although they can be included (RGA 70).

Insofar as a collective model is being described, individual particle motion is not included explicitly. Collective states are understood to be due to the coherent motion of many nucleons which can be described by relatively few collective co-ordinates. In particular the quadrupole collective model involves five collective co-ordinates. If the nucleus is deformed, it is convenient to describe its shape in terms of "intrinsic" axes rotating with the nucleus. It is also convenient to take these body-fixed axes to be the

principal axes of the nucleus. In this case the intrinsic shape of the nucleus may be completely described by two co-ordinates. However an additional three co-ordinates are required to describe the orientation of the intrinsic axes of the nucleus.

The orientation of the nucleus is described by specifying the three Euler angles  $\theta_1$ ,  $\theta_2$  and  $\theta_3$  required to transform from the laboratory-fixed co-ordinate system to the body-fixed co-ordinate system. The shape of the nucleus is given by specifying its radius as a function of angle in the intrinsic system:

$$\begin{aligned} R(\theta, \phi) &= R_0 [1 + \beta \cos \gamma Y_{20}(\theta, \phi) + \frac{\beta \sin \gamma}{\sqrt{2}} (Y_{22}(\theta, \phi) + Y_{2-2}(\theta, \phi))] \\ &= R_0 [1 + \beta_x Y_{20}(\theta, \phi) + \frac{\beta_y}{\sqrt{2}} (Y_{22}(\theta, \phi) + Y_{2-2}(\theta, \phi))] \end{aligned} \quad (3.1)$$

Clearly a pair of intrinsic cartesian co-ordinates  $\{\beta_x, \beta_y\}$  can be used instead of the pair  $\{\beta, \gamma\}$ . The connection between pairs of co-ordinates is

$$\beta_x = \beta \cos \gamma \quad \beta_y = \beta \sin \gamma \quad (3.2)$$

or

$$\beta = \sqrt{\beta_x^2 + \beta_y^2} \quad \text{and} \quad \gamma = \tan^{-1}(\beta_y / \beta_x) \quad (3.3)$$

Both pairs of co-ordinates will be used in what follows.  $\beta$  and  $\gamma$  are more conventional; however the cartesian co-ordinates  $\beta_x$  and  $\beta_y$  are more useful for numerical calculations.

## 2. Schroedinger Equation

In the collective model, there are three contributions to the energy:

$$E = T_{\text{rot}} + T_{\text{vib}} + V. \quad (3.4)$$

The first term,  $T_{\text{rot}}$ , refers to the rotational kinetic energy due to the time rate of change of the Euler angles which represent the rotation of the nucleus. Written in terms of the dynamical variables

$$T_{\text{rot}} = \frac{1}{2} \sum_v \mathcal{J}_v(\beta_x, \beta_y) \dot{\theta}_v^2. \quad (3.5)$$

The second term,  $T_{\text{vib}}$ , refers to the vibrational kinetic energy due to the nuclear change of shape around an equilibrium shape. The vibrational energy can be written as

$$T_{\text{vib}} = \frac{1}{2} B_{xx} \dot{\beta}_x^2 + B_{xy} \dot{\beta}_x \dot{\beta}_y + \frac{1}{2} B_{yy} \dot{\beta}_y^2. \quad (3.6)$$

The last term,  $V$ , represents the potential energy due to shape changes. It is expressed in terms of the shape co-ordinates  $\beta_x$  and  $\beta_y$  but not their time derivatives:

$$V = V(\beta_x, \beta_y). \quad (3.7)$$

As Kumar and Baranger have emphasized, the seven functions  $\mathcal{J}_v(\beta_x, \beta_y)$   $v = 1, 2, 3$ ,  $B_{xx}(\beta_x, \beta_y)$ ,  $B_{xy}(\beta_x, \beta_y)$ ,  $B_{yy}(\beta_x, \beta_y)$  and  $V(\beta_x, \beta_y)$  are arbitrary except for certain symmetry conditions. K-B also note, however, that the pairing-plus-quadrupole model indicates that the most sensitive of the functions is the potential energy function  $V(\beta_x, \beta_y)$ . As a consequence we will follow the lead of most investigators and restrict

the inertial functions to those originally given by Bohr (Boh 52):

$$J_v = 4B\beta^2 \sin^2(\gamma - \frac{2\pi}{3} v) \quad (3.8)$$

and

$$B_{xx} = B_{yy} = B, \quad B_{xy} = 0. \quad (3.9)$$

Equations (3.8) and (3.9) were derived assuming small deviations from sphericity. These inertial functions are the simplest choice that satisfy all the required symmetry properties (KB 67). The main justification for using the Bohr inertial functions is simply that, for definiteness, some choice had to be made and the model has been remarkably successful in explaining a large range of data. However, ultimately it is hoped that suitable microscopic theories will be developed which will calculate these inertial functions from first principles using realistic interactions.

There is some experimental evidence in favour of a quadratic dependence of the moments of inertia on the deformation  $\beta$ . Diamond et al (DSS 64) have plotted the experimental moment of inertia (determined from  $E_{J=2}$ ) as a function of the experimental deformation  $\beta$  (determined from BE2(2+0) transitions). To a good approximation the experimental data points lie on a parabolic curve. This agrees with equation (3.8). If it is assumed that a nucleus behaves like an irrotational fluid of constant density, then it is found that  $B = \frac{1}{2} \rho R_0^5$ . The Diamond et al paper (DSS 64) demonstrates that the hydro-



dynamical estimate for B is too small by a factor of about six. An alternate method of determining B will be described in the next chapter.

The next step is to quantize the expression for the energy (equation (3.4)). To do this the Pauli (Pau 33) prescription is used. Since the details of this process are given elsewhere (KB 67, Eis 70) only the results will be represented. The classical energy expression in equation (3.4) is replaced by a collective Hamiltonian defined by

$$\hat{H}_B = \hat{T}_{\text{rot}} + \hat{T}_{\text{vib}} + \hat{V}. \quad (3.10)$$

The rotational kinetic energy operator is

$$\hat{T}_{\text{rot}} = \frac{1}{2} \sum_{v=1}^3 \frac{\hat{J}_v^2}{2J_v} \quad (3.11)$$

where the operators  $\hat{J}_1$ ,  $\hat{J}_2$  and  $\hat{J}_3$  are the usual angular momentum operators with respect to the body-fixed co-ordinate system. The vibrational kinetic operator is

$$\hat{T}_{\text{vib}} = -\frac{1}{2B} \frac{1}{Q(\beta_x, \beta_y)} \left[ \frac{\partial}{\partial \beta_x} Q(\beta_x, \beta_y) \frac{\partial}{\partial \beta_x} + \frac{\partial}{\partial \beta_y} Q(\beta_x, \beta_y) \frac{\partial}{\partial \beta_y} \right] \quad (3.12-i)$$

$$= -\frac{1}{2B} \left[ \frac{1}{\beta^4} \frac{\partial}{\partial \beta} \beta^4 \frac{\partial}{\partial \beta} + \frac{1}{\beta^3 \sin 3\gamma} \frac{\partial}{\partial \gamma} \sin 3\gamma \frac{\partial}{\partial \gamma} \right]. \quad (3.12-ii)$$

The first form of  $\hat{T}_{\text{vib}}$  is more convenient and will be used in this work. The volume element becomes

$$d\tau = \sin \theta_2 Q(\beta_x, \beta_y) d\theta_1 d\theta_2 d\theta_3 d\beta_x d\beta_y \quad (3.13)$$

where the integration density is

$$Q(\beta_x, \beta_y) = 2 B^{5/2} \beta_y (3\beta_x^2 - \beta_y^2) \quad (3.14)$$

Written in terms of  $\beta$  and  $\gamma$  the volume element is

$$d\tau = \sin\theta_2 Q'(\beta, \gamma) d\theta_1 d\theta_2 d\theta_3 d\beta d\gamma \quad (3.15)$$

where  $Q'(\beta, \gamma) = 2 B^{5/2} \beta^4 \sin 3\gamma$ .

Ignoring for the moment rotational degrees of freedom a vibrational wavefunction  $\psi(\beta_x, \beta_y)$  is normalized by

$$\int \psi^*(\beta_x, \beta_y) \psi(\beta_x, \beta_y) d\tau = \int \psi^*(\beta_x, \beta_y) \psi(\beta_x, \beta_y) Q(\beta_x, \beta_y) d\beta_x d\beta_y = 1 \quad (3.16)$$

Using the Bohr Hamiltonian the Schroedinger equation

$$\hat{H}_B \psi = E \psi \quad (3.17)$$

must be solved. Most of the rest of this chapter will be devoted to explaining how equation (3.17) is solved.

### 3. Matrix Elements of the Rotational Kinetic Energy

A conventional set of basis states for the operator  $\hat{T}_{\text{rot}}$  will be given. First the operator  $\hat{T}_{\text{rot}}$  can be written as

$$\hat{T}_{\text{rot}} = p \hat{J}^2 + (q-p) \hat{J}_3^2 + \frac{1}{2} r (\hat{J}_+^2 + \hat{J}_-^2) \quad (3.18)$$

where

$$p = \frac{1}{4} \left( \frac{1}{J_1} + \frac{1}{J_2} \right), \quad q = \frac{1}{2} \frac{1}{J_3}, \quad r = \frac{1}{4} \left( \frac{1}{J_1} - \frac{1}{J_2} \right) \quad (3.19-i, ii, iii)$$

and

$$\hat{J}_+ = \hat{J}_1 + i \hat{J}_2, \quad \hat{J}_- = \hat{J}_1 - i \hat{J}_2 \quad (3.20)$$

A normalized basis state for  $\hat{T}_{\text{rot}}$  is

$$(\theta_1 \theta_2 \theta_3 | JMK) = \sqrt{\frac{2J+1}{8\pi^2}} D_{MK}^J(\theta_1, \theta_2, \theta_3) \quad (3.21)$$

Here  $D_{MK}^J$  is the usual Wigner rotational transformation matrix according to the convention used by Davydov (Dav 66). In this basis the matrix elements for the angular momentum operators are well known (Dav 66):

$$(JMK | \hat{J}_3 | JMK) = K \quad (3.22-i)$$

$$(JMK | \hat{J}_+ | JMK+1) = (JMK+1 | \hat{J}_- | JMK) = \sqrt{(J+K+1)(J-K)} \quad (3.22-ii)$$

$$(JMK | \hat{J}^2 | JMK) = J(J+1) \quad (3.22-iii)$$

(See also Appendix B, Equation (B.3)). All other matrix elements are zero.

Again the rotational wavefunctions are symmetrized according to the A representation of the  $D_2$  group. In equation (B.12) the symmetrized and normalized function  $|\phi_{MK}^J\rangle$  is defined. It can be written

$$|\phi_{MK}^J\rangle = \frac{1}{\sqrt{2(1+\delta_{K0})}} [ |JMK\rangle + (-1)^J |JM-K\rangle ] \quad (3.23)$$

where K must be even. Combining equations (3.18), (3.19), (3.22) and (3.23) we finally obtain

$$\langle \phi_{MK}^J | \hat{T}_{\text{rot}} | \phi_{MK}^J \rangle = p J(J+1) + (q-p)K^2 \quad (3.24)$$

$$\langle \phi_{MK-2}^J | \hat{T}_{\text{rot}} | \phi_{MK}^J \rangle = \langle \phi_{MK}^J | \hat{T}_{\text{rot}} | \phi_{MK-2}^J \rangle$$

$$= \frac{1}{2} r \sqrt{(1+\delta_{K2})(J+K-1)(J-K+2)(J+K)(J-K+1)} \quad (3.25)$$

All other matrix elements are zero.

#### 4. Separation of Variables

Equation (3.17) is a linear partial differential equation in five variables:  $\theta_1, \theta_2, \theta_3, \beta_x$  and  $\beta_y$ . Since the eigenfunctions of  $\hat{T}_{\text{rot}}$  form a complete set of states, it is convenient to expand the most general solution of equation (3.17) as

$$\psi = \sum_{J,K,M} a_{KM}^J \phi_{MK}^J. \quad (3.26)$$

The quantities  $a_{KM}^J$  do not depend on  $\vec{\theta} = (\theta_1, \theta_2, \theta_3)$  because  $\vec{\theta}$  appears only in  $\hat{T}_{\text{rot}}$  and not in  $\hat{T}_{\text{vib}}$  or  $\hat{V}$ . The  $a_{KM}^J$ 's do, however, depend on  $\beta_x$  and  $\beta_y$ . Since  $\hat{H}_B$ ,  $\hat{J}^2$  and  $\hat{J}_z$  (the component of  $\hat{J}$  along the space-fixed z-axis) all commute, an eigenstate of  $\hat{H}_B$  can be written as  $\psi_{\lambda JM}$  where  $J$  and  $M$  indicate eigenvalues of  $\hat{J}^2$  and  $\hat{J}_z$  and  $\lambda$  labels all additional quantum members. In co-ordinate representation the solution to equation (3.17) can be written

$$\psi_{\lambda JM}(\beta_x, \beta_y, \vec{\theta}) = \sum_{K=0(2)}^J A_{\lambda JK}(\beta_x, \beta_y) \phi_{MK}^J(\vec{\theta}). \quad (3.27)$$

The notation  $\sum_{K=0(2)}^J$  is explained in Appendix B. A summation over  $K$  is necessary because  $\hat{J}_3$  does not, in general, commute with  $\hat{H}_B$ . The intrinsic wavefunctions  $A_{\lambda JK}(\beta_x, \beta_y)$  are integrated with respect to the integration density  $Q(\beta_x, \beta_y)$ . Thus the normalization of the wavefunction in equation (3.27) becomes

$$\sum_{K=0(2)}^J \int |A_{\lambda JK}(\beta_x, \beta_y)|^2 Q(\beta_x, \beta_y) d\beta_x d\beta_y = 1. \quad (3.28)$$

Equation (3.27) is reminiscent of the technique of separation of variables used to solve partial differential

equations. Since  $\hat{T}_{\text{rot}}$  is coupled to the rest of  $\hat{H}_B$  through its dependence on  $\beta_x$  and  $\beta_y$ , the solution of equation (3.17) can not be separated into a single product of a function of  $\theta$  and a function of  $(\beta_x, \beta_y)$ .

### 5. Expectation Value of the Hamiltonian

Equation (3.17) is equivalent to solving the variational problem (KB 67)

$$\delta \langle \psi | \hat{H}_B | \psi \rangle = 0 \quad (3.29-i)$$

subject to the constraint

$$\langle \psi | \psi \rangle = 1 \quad (3.29-ii)$$

for an arbitrary variation of the state  $|\psi\rangle$ . For angular momentum  $J$  it is necessary to evaluate

$$\begin{aligned} \langle \psi_{\lambda JM} | \hat{H}_B | \psi_{\lambda JM} \rangle &= \langle \psi_{\lambda JM} | \hat{T}_{\text{rot}} | \psi_{\lambda JM} \rangle + \langle \psi_{\lambda JM} | \hat{T}_{\text{vib}} | \psi_{\lambda JM} \rangle \\ &+ \langle \psi_{\lambda JM} | \hat{V} | \psi_{\lambda JM} \rangle. \end{aligned} \quad (3.30)$$

Using the form of equation (3.27) as well as equation (3.12-i),

$$\begin{aligned} \langle \psi_{\lambda JM} | \hat{T}_{\text{vib}} | \psi_{\lambda JM} \rangle &= -\frac{1}{2B} \int d\beta_x d\beta_y d\theta_1 d\theta_2 d\theta_3 \sin\theta_2 Q(\beta_x, \beta_y) \sum_K A_{\lambda JK}^* \Phi_{MK}^{J*} \\ &\times \frac{1}{Q(\beta_x, \beta_y)} \sum_{s=x,y} \frac{\partial}{\partial \beta_s} Q(\beta_x, \beta_y) \frac{\partial}{\partial \beta_s} \sum_K A_{\lambda JK} \Phi_{MK}^J \\ &= -\frac{1}{2B} \sum_K \int \int d\beta_x d\beta_y A_{\lambda JK}^*(\beta_x, \beta_y) \sum_{s=x,y} \frac{\partial}{\partial \beta_s} Q(\beta_x, \beta_y) \\ &\times \frac{\partial}{\partial \beta_s} A_{\lambda JK}(\beta_x, \beta_y) \end{aligned} \quad (3.31)$$

by orthogonality of the rotation functions. Integrating by parts yields (KB 67)

$$\langle \psi_{\lambda JM} | \hat{T}_{\text{vib}} | \psi_{\lambda JM} \rangle = \frac{1}{2B} \sum_K' \iint d\beta_x d\beta_y Q(\beta_x, \beta_y) \sum_{s=x,y} \left| \frac{\partial A_{\lambda JK}(\beta_x, \beta_y)}{\partial \beta_s} \right|^2. \quad (3.32)$$

The advantage of integrating by parts is that there is no longer a mixture of first and second derivatives in  $\beta_s$ . Instead there are squares of first derivatives. A second advantage will be demonstrated later: any matrix representation of  $\hat{T}_{\text{vib}}$  is manifestly symmetric.

The other two terms in equation (3.30) are simpler:

$$\begin{aligned} \langle \psi_{\lambda JM} | \hat{T}_{\text{rot}} | \psi_{\lambda JM} \rangle &= \sum_{K,K'}' \iint d\beta_x d\beta_y Q(\beta_x, \beta_y) A_{\lambda JK}^*(\beta_x, \beta_y) \\ &\quad \times \langle \phi_{MK}^J | \hat{T}_{\text{rot}} | \phi_{MK'}^J \rangle A_{\lambda JK}(\beta_x, \beta_y). \end{aligned} \quad (3.33)$$

Finally

$$\langle \psi_{\lambda JM} | \hat{V} | \psi_{\lambda JM} \rangle = \sum_K' \iint d\beta_x d\beta_y Q(\beta_x, \beta_y) |A_{\lambda JK}(\beta_x, \beta_y)|^2 V(\beta_x, \beta_y). \quad (3.34)$$

### III. Numerical Methods: Vibrational and Potential Energies

#### 1. Grid in $\beta$ - $\gamma$ Space

The integrations over  $\beta_x$  and  $\beta_y$  in equations (3.32), (3.33) and (3.34) are each done numerically. The region of integration is shown in Figure 3.1. The theoretical range of  $\beta$  is given by  $0 \leq \beta < \infty$ . Because of symmetry reasons it is sufficient to consider  $\gamma$  in the range  $0 \leq \gamma \leq \pi/3$ . When written in terms of  $\beta_x$  and  $\beta_y$ , these relations become

$$0 \leq \beta_x < \infty, \quad 0 \leq \beta_y \leq \sqrt{3} \beta_x. \quad (3.35-i, ii)$$

Because the integrations are done numerically, it is necessary to restrict the region of integration to a finite area. The integration region is chosen to be an equilateral triangle whose sides are along the  $\gamma=0$  ( $\beta_y=0$ ) and  $\gamma=\pi/3$  ( $\beta_y=\sqrt{3} \beta_x$ ) lines. The length of the sides of the triangle determine a maximum  $\beta$  value denoted as  $\beta_m$ . It is assumed that for  $\beta > \beta_m$ , the wavefunction is sufficiently small that it can be ignored. The validity of this assumption will be checked later.

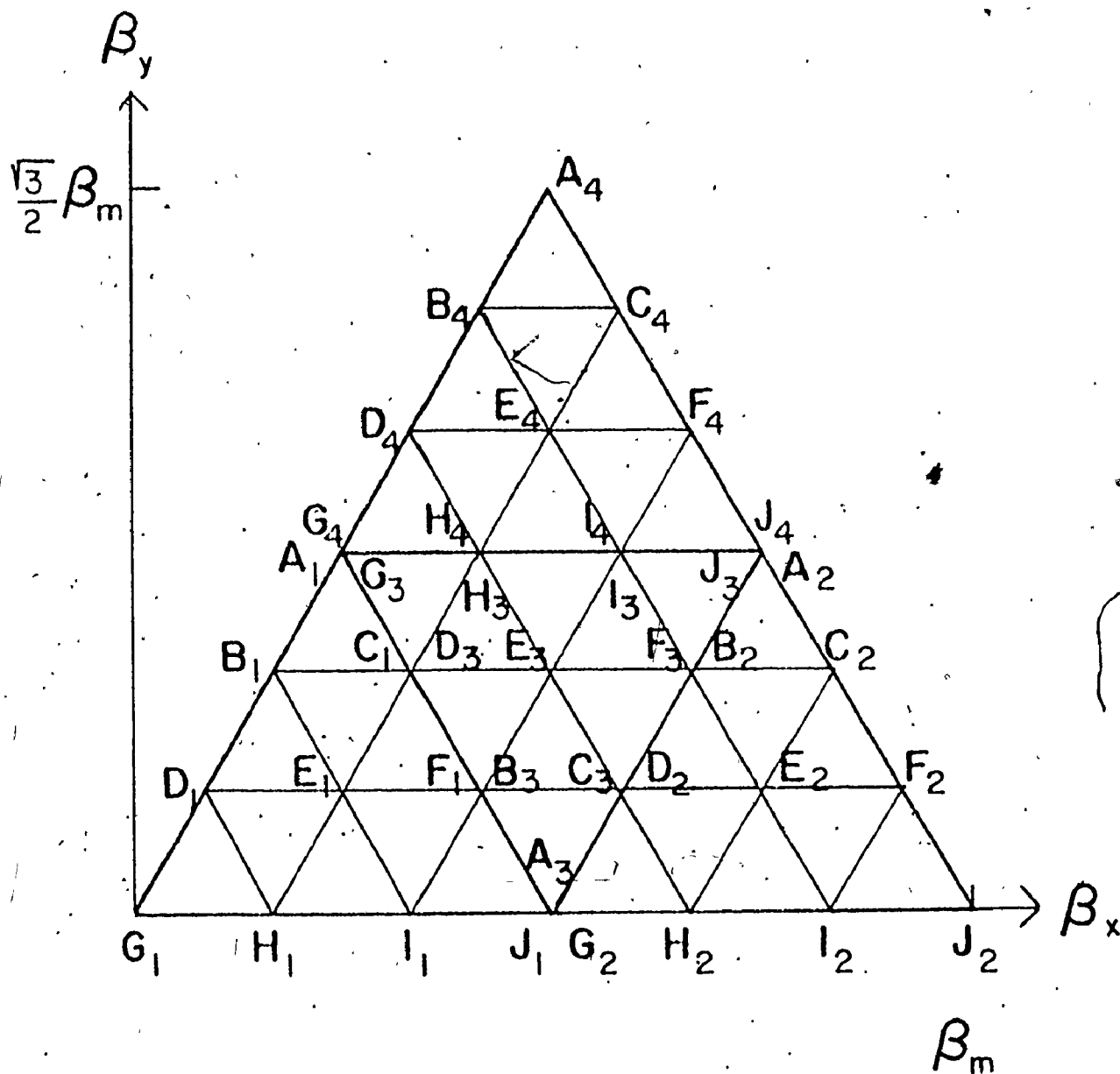
The functions to be integrated are characterized by their values on a triangular grid. This grid is illustrated in Figure 3.1. There are only 28 grid points in the diagram. In the actual calculation a finer grid with 190 grid points is used.

## 2. Integration Weights

The simplest method of integrating a function defined on the mesh in Figure 3.1 is to sum the value of the function over all the grid points and then multiplying by a suitable normalization constant. However this pseudo-trapezoidal procedure would be rather inaccurate. Instead the following method is used to calculate suitable integration weights.

The integration region in Figure 3.1 is composed of small triangles which will be referred to as minor triangles. The minor triangles are grouped to form four major triangles

Figure 3.1



Grid points in  $\beta$ - $\gamma$  plane showing 4 major triangles. This figure illustrates a relatively coarse grid for performing the numerical integration. Each of the four major triangles has associated with it ten grid points, A, B, C, ..., J.



each containing nine minor triangles. An example of a major triangle is the triangle  $A_2 G_2 J_2$ . Over each major triangle, the integrand is approximated by a cubic polynomial in appropriate variables. A diagram of one major triangle is shown in Figure 3.2. Each of the 10 grid points in this figure is given cartesian co-ordinates relative to a system of co-ordinates centred at the point E. A convenient unit of length for this co-ordinate system is chosen to be the side of a minor triangle. Thus, the point A has co-ordinate  $(0, \sqrt{3})$ ; the point B has co-ordinates  $(-1/2, \sqrt{3}/2)$ ; etc.

If the values of the integrand  $f(\beta_x, \beta_y)$  at each of the 10 grid points A, B, ..., J are  $f_A, f_B, \dots, f_J$  respectively, then a 10 parameter cubic polynomial in x and y,

$$P_3(x, y) \equiv ax^3 + bx^2y + cxy^2 + dy^3 + ex^2 + fxy + gy^2 + hx + jy + k \quad (3.36)$$

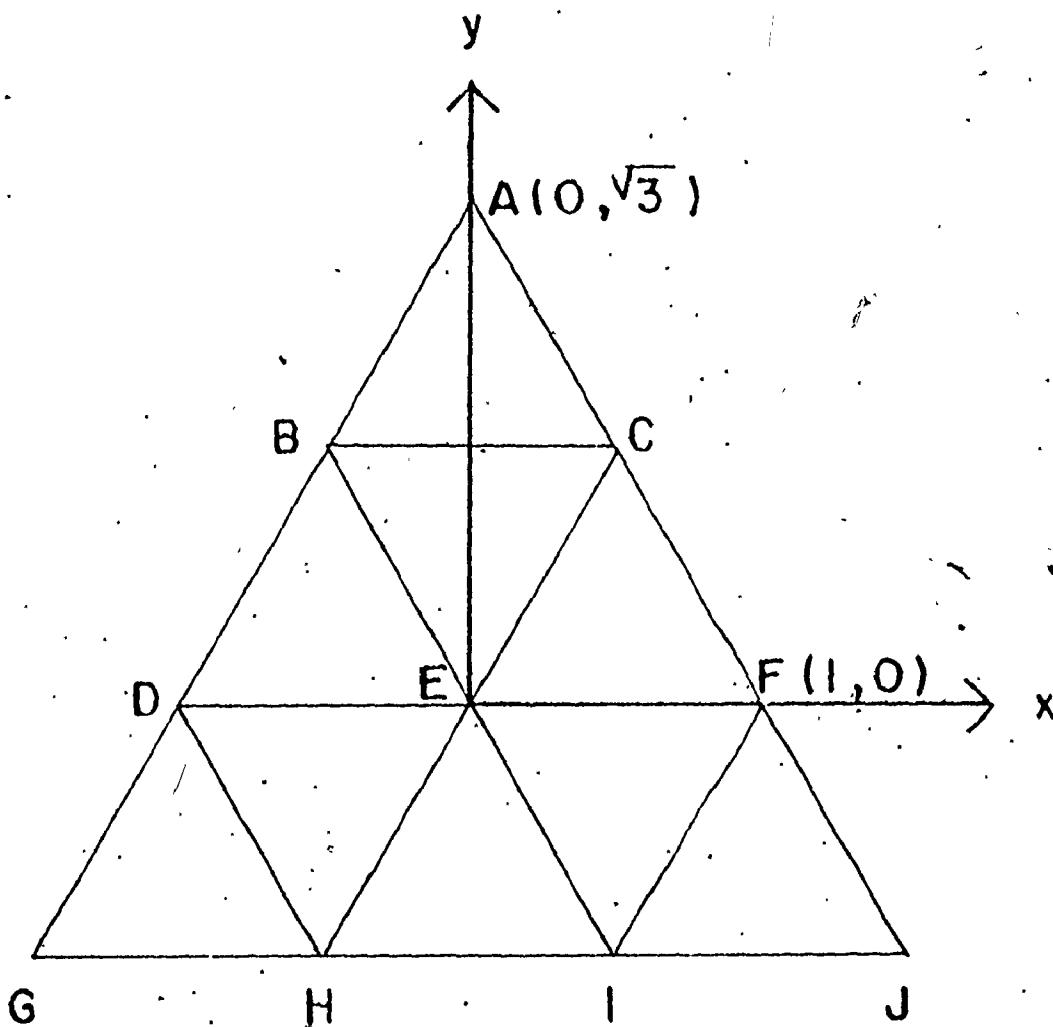
can be determined which takes on the same values as the integrand  $f(\beta_x, \beta_y)$  at the 10 grid points. If the integrand is a fairly smooth function, then  $P_3(x, y)$  should be a reasonable approximation to  $f(\beta_x, \beta_y)$  between the grid points.

There are 10 conditions on  $P_3(x, y)$ . For example, if  $f = P_3$  at the point A, then

$$3\sqrt{3}d + 3g + \sqrt{3}j + k = f_A. \quad (3.37)$$

There are 9 other similar conditions. Since the polynomial  $P_3$  has exactly 10 coefficients, there will normally be a unique solution for the coefficients a, b, ..., k. All 10 equations of

Figure 3.2



Single major triangle with x-y co-ordinate system.  
 Each of the ten points in a given major triangle  
 can be given co-ordinates in a cartesian co-ordinate  
 system with origin located at point E.

the form of equation (3.37) as well as the solutions for the coefficients are given in Appendix E.

The cubic  $P_3$  is integrated over the region of a major triangle. The analytic result is

$$S = \iint_{\Delta} dx dy P_3(x, y) \\ = \frac{9\sqrt{3}}{160} [3\sqrt{3}(d-b) + 5(3e+3g+8k)] \quad (3.38)$$

Substituting the expressions for the coefficients given in equation (E.2) in Appendix E the integral becomes

$$S = \frac{3\sqrt{3}}{160} [4f_A + 9f_B + 9f_C + 9f_D + 54f_E + 9f_F + 4f_G + 9f_H + 9f_I + 4f_J] \quad (3.39)$$

The x-y co-ordinate system in Figure 3.2 was scaled so that each minor triangle had side 1. More generally each minor triangle has side h. For this case equation (3.39) must be modified to read

$$S = \frac{3\sqrt{3}}{160} h^2 [4f_A + 9f_B + 9f_C + 9f_D + 54f_E + 9f_F + 4f_G + 9f_H + 9f_I + 4f_J] \quad (3.40)$$

This yields the simple (as opposed to composite) cubic integration formula

$$\iint_{\Delta} d\beta_x d\beta_y f(\beta_x, \beta_y) \approx \sum_{\alpha=A, B, \dots, J} w_{\alpha} f_{\alpha} \quad (3.41)$$

where

$$w_A = \frac{3\sqrt{3} h^2 \times 4}{160} \quad (3.42-i)$$

$$w_B = \frac{3\sqrt{3} h^2 \times 9}{160} \quad \text{etc.} \quad (3.42-ii)$$

If there is more than one major triangle in the total integration region, it is necessary to add the integration weights for the grid points which belong to more than one major triangle. For the case of 4 major triangles (28 grid points) the composite cubic integration weights,  $w_\alpha$ , shown in Figure 3.3 are obtained. In this case  $h = \beta_m/6$  where  $\beta_m$  is the maximum value of  $\beta$ . Given a set of appropriate integration weights  $w_\alpha$  it is possible to integrate equation (3.34) numerically to obtain

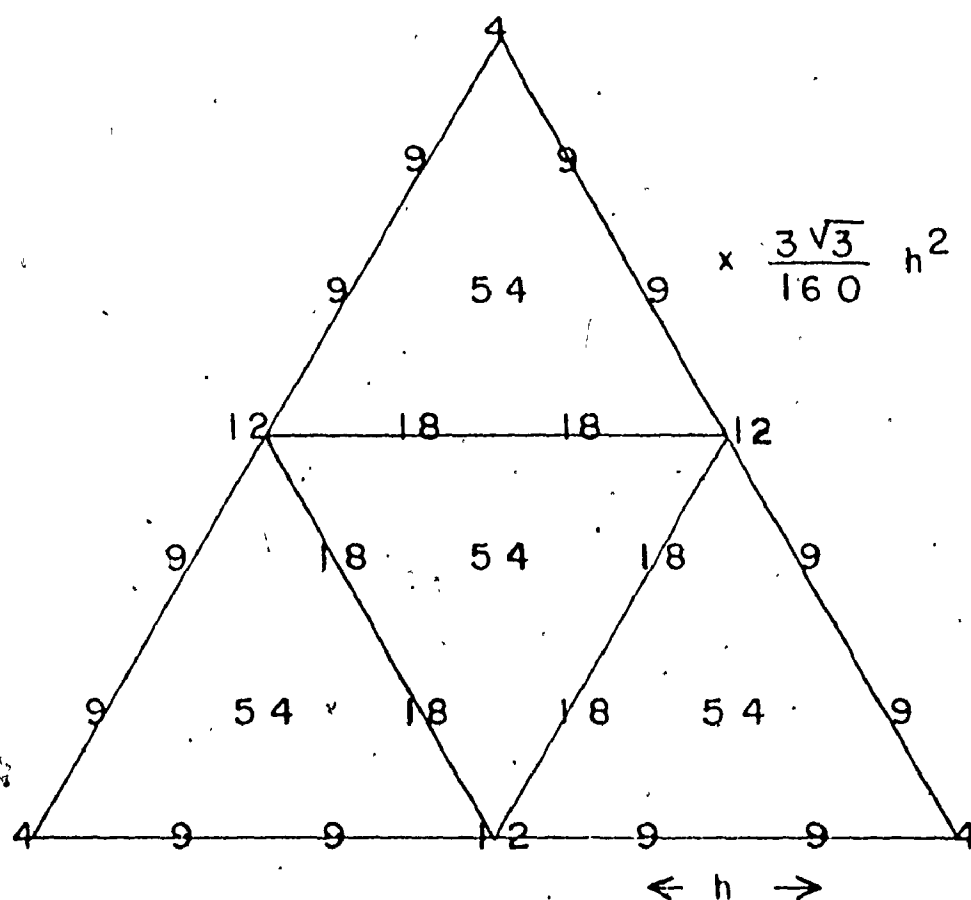
$$\langle \psi_{\lambda JM} | \hat{V} | \psi_{\lambda JM} \rangle = \sum_{\alpha} [w_{\alpha} Q_{\alpha} V_{\alpha} \sum_k |A_{\lambda JK; \alpha}|^2] \quad (3.43)$$

where  $\alpha$  labels the grid point in the mesh. The normalization condition equation (3.29-ii) becomes

$$\sum_{\alpha} [w_{\alpha} Q_{\alpha} \sum_k |A_{\lambda JK; \alpha}|^2] = 1. \quad (3.44)$$

This technique of numerical integration is similar to that used by Kumar and Baranger. The difference is that they used a quadratic polynomial whereas we have used a cubic. There are two reasons for using a cubic polynomial. The first reason is that a cubic yields a higher order integration algorithm which therefore should be more accurate than an algorithm based on a quadratic polynomial. A second reason is related to the fact that a quadratic yields integration weights of which about one quarter are exactly zero. As will be explained in section V-1, zero integration weights lead to unpleasant numerical difficulties.

Figure 3.3



Numerical integration weights. To perform an integration in the  $\beta$ - $\gamma$  plane, the value of the integrand at a point is multiplied by the corresponding weight. Here  $h$  is the separation of adjacent grid points. In this case  $h = \beta_m/6$  where  $\beta_m$  is the maximum value of  $\beta$ .

### 3. Differentiation Weights

The expectation value for  $\hat{T}_{vib}$  (see equation (3.32)) contains derivatives with respect to  $\beta_x$  and  $\beta_y$ . Both the differentiations and the integrations are to be performed numerically. For the moment it is assumed that the integration region in the  $\beta$ - $\gamma$  plane consists of only one major triangle. The function to be differentiated, namely  $g(\beta_x, \beta_y) \equiv A_{\lambda JK}(\beta_x, \beta_y)$ , is approximated in the major triangle by a cubic polynomial  $P'_3(x, y)$ . The cubic is expressed in the same  $x$ - $y$  co-ordinate system used previously, i.e.

$$P'_3(x, y) \equiv ax^3 + bx^2y + cxy^2 + dy^3 + ex^2 + fxy + gy^2 + hx + jy + k \quad (3.45)$$

(see Figure 3.2). As in the previous section, the polynomial  $P'_3$  is specified by the restriction that it take on the same value as  $g(\beta_x, \beta_y)$  at the 10 grid points. For example the condition at grid point A (see Figure 3.2) is

$$3\sqrt{3}d + 3g + \sqrt{3}j + k = g_A \quad (3.46-i)$$

As previously, equation (3.46) along with the 9 similar conditions can be inverted to give the coefficients  $a, b, \dots$  in terms of  $g_A, g_B, \dots$ .

The derivatives  $\frac{\partial P'_3(x, y)}{\partial x}$  and  $\frac{\partial P'_3(x, y)}{\partial y}$  are calculated analytically and evaluated at each of the 10 points A, B, ... . For the point A(0,  $\sqrt{3}$ ), for example,

$$\left. \frac{\partial P'_3(x, y)}{\partial x} \right|_A = 3c + \sqrt{3}f + h \quad (3.47-i)$$

and

$$\left. \frac{\partial P'_3(x,y)}{\partial y} \right|_A = 9d + 2\sqrt{3} g + j . \quad (3.47-ii)$$

Using the solution of the equations (3.46) (given by equations (E.2) in Appendix E), the derivatives in equations (3.47) are expressed in terms of  $g_A, g_B$  etc. For the point  $A(0, \sqrt{3})$ , for example, this yields the relations

$$\left. \frac{\partial P'_3(x,y)}{\partial x} \right|_A = -3g_B + 3g_C + \frac{3}{2} g_D - \frac{3}{2} g_F - \frac{1}{3} g_G + \frac{1}{3} g_J \quad (3.48-i)$$

and

$$\left. \frac{\partial P'_3(x,y)}{\partial y} \right|_A = \sqrt{3} \left( \frac{11}{9} g_A - g_B - g_C + \frac{1}{2} g_D + \frac{1}{2} g_F - \frac{1}{9} g_G - \frac{1}{9} g_J \right) . \quad (3.48-ii)$$

Equations (3.48) and the 9 pairs of similar relations are given in Appendix E, equations (E.3).

In equation (3.32), the quantity

$$\sum_{s=x,y} \left| \frac{\partial A_{\lambda JK}(\beta_x, \beta_y)}{\partial \beta_s} \right|^2$$

must be evaluated. This quantity is related to the expression

$$\Gamma(x,y) \equiv \left( \frac{\partial P'_3(x,y)}{\partial x} \right)^2 + \left( \frac{\partial P'_3(x,y)}{\partial y} \right)^2 . \quad (3.49)$$

The value of the function  $\Gamma(x,y)$  at each of the 10 grid points is given using equation (3.48). For example, at the point A

$$\begin{aligned} \Gamma_A &= (-3g_B + 3g_C + \frac{3}{2} g_D - \frac{3}{2} g_F - \frac{1}{3} g_G + \frac{1}{3} g_J)^2 \\ &+ 3 \left( \frac{11}{9} g_A - g_B - g_C + \frac{1}{2} g_D + \frac{1}{2} g_F - \frac{1}{9} g_G - \frac{1}{9} g_J \right)^2 \end{aligned}$$

$$\begin{aligned}
&= \frac{121}{27} g_A^2 + 12 g_B^2 + \dots + \frac{4}{27} g_J^2 - \frac{22}{3} g_A g_B - \frac{22}{3} g_A g_C + \dots \\
&+ 6 g_C g_D + \dots
\end{aligned} \tag{3.50}$$

Similar relations can be given for  $\Gamma_B, \Gamma_C$  etc.

The coefficients in the above equation can be used to form a matrix  $\underline{T}^{(A)}$ . If  $\underline{g}$  represents the  $10 \times 1$  column matrix with entries  $g_A, g_B, \dots, g_J$ , then equation (3.50) can be written

$$\Gamma_A = \underline{g}^T \underline{T}^{(A)} \underline{g} . \tag{3.51}$$

The matrix  $\underline{T}^{(A)}$  is taken to be symmetric. As a result the off-diagonal matrix elements are one half the coefficients in equation (3.50). For example  $T_{CD}^{(A)} = T_{DC}^{(A)} = 3$ . For each grid point B, C, ... a corresponding matrix  $\underline{T}^{(B)}, \underline{T}^{(C)}, \dots$  is formed. These matrices can all be grouped into a three-dimensional matrix  $\underline{R}$  where

$$R_{\alpha\beta\gamma} = T_{\beta\gamma}^{(\alpha)} . \tag{3.52}$$

The matrix elements of  $\underline{R}$  are listed in Table 3.1.

Equation (3.51) expresses the values of the function  $\Gamma(x,y)$  at the point A in terms of finite differences.

The integral

$$\begin{aligned}
S &= \iint_{\Delta} dx dy \Gamma(x,y) \\
&= \sum_{\alpha=A,B,\dots} w_{\alpha} \Gamma_{\alpha} = \sum_{\alpha\beta\gamma} w_{\alpha} R_{\alpha\beta\gamma} g_{\beta} g_{\gamma} .
\end{aligned} \tag{3.53}$$



Table 3.1

Matrix  $R_{\alpha\beta\gamma}$ Matrix  
Element  
( $\beta\gamma$ )  
↓Integration Point ( $\alpha$ ) →

	A	B	C	D	E	F	G	H	I	J
AA	121/27	4/27	4/27	1/27	1/27	1/27	4/27	4/27	4/27	4/27
AB	-11/3	4/9	-2/9	-2/9	-1/9	0	-2/3	-4/9	-2/9	0
AC	-11/3	-2/9	4/9	0	-1/9	-2/9	0	-2/9	-4/9	-2/3
AD	11/6	-2/9	2/9	-1/18	1/18	-1/18	4/3	4/9	0	0
AE	0	-4/9	-4/9	2/9	0	2/9	0	8/9	8/9	0
AF	11/6	2/9	-2/9	-1/18	1/18	-1/18	0	0	4/9	4/3
AG	-11/27	1/27	-2/27	1/27	-1/54	1/27	-11/27	-2/27	1/27	-2/27
AH	0	0	1/9	1/9	1/18	-1/9	-2/3	-5/9	-2/9	1/3
AI	0	1/9	0	-1/9	1/18	1/9	1/3	-2/9	-5/9	-2/3
AJ	-11/27	-2/27	1/27	1/27	-1/54	1/27	-2/27	1/27	-2/27	-11/27
BB	12	7/3	4/3	4/3	1/3	0	3	4/3	1/3	0
BC	-6	-5/3	-5/3	0	1/3	0	0	2/3	2/3	0
BD	-6	1/3	-4/3	1/3	-1/6	0	-6	-4/3	0	0
BE	0	-10/3	8/3	-4/3	0	0	0	-8/3	-4/3	0
BF	3	5/3	-2/3	1/3	-1/6	0	0	0	-2/3	0
BG	4/3	-1/18	4/9	-2/9	1/18	0	11/6	2/9	-1/18	0
BH	0	0	-2/3	-2/3	-1/6	0	3	5/3	1/3	0
BI	0	5/6	0	2/3	-1/6	0	-3/2	2/3	5/6	0
BJ	-2/3	-5/9	1/9	-2/9	1/18	0	1/3	-1/9	1/9	0
CC	12	4/3	7/3	0	1/3	4/3	0	1/3	4/3	3
CD	3	-2/3	5/3	0	-1/6	1/3	0	-2/3	0	0
CE	0	8/3	-10/3	0	0	-4/3	0	-4/3	-8/3	0
CF	-6	-4/3	1/3	0	-1/6	1/3	0	0	-4/3	-6
CG	-2/3	1/9	-5/9	0	1/18	-2/9	0	1/9	-1/9	1/3
CH	0	0	5/6	0	-1/6	2/3	0	5/6	2/3	-3/2
CI	0	-2/3	0	0	-1/6	-2/3	0	1/3	5/3	3
CJ	4/3	4/9	-1/18	0	1/18	-2/9	0	-1/18	2/9	11/6
DD	3	4/3	4/3	7/3	1/3	1/3	12	4/3	0	0
DE	0	-4/3	-8/3	-10/3	0	-4/3	0	8/3	0	0
DF	-3/2	2/3	2/3	5/6	-1/6	5/6	0	0	0	0
DG	-2/3	-2/9	-4/9	4/9	-1/9	-2/9	-11/3	-2/9	0	0
DH	0	0	2/3	-5/3	1/3	2/3	-6	-5/3	0	0
DI	0	1/3	0	5/3	-1/6	-2/3	3	-2/3	0	0
DJ	1/3	-2/9	-1/9	-5/9	1/18	1/9	-2/9	1/9	0	0
EE	0	16/3	16/3	16/3	0	16/3	0	16/3	16/3	0
EF	0	-8/3	-4/3	-4/3	0	-10/3	0	0	8/3	0
EG	0	2/9	8/9	-4/9	0	8/9	0	-4/9	2/9	0
EH	0	0	-4/3	8/3	0	-8/3	0	-10/3	-4/3	0
EI	0	-4/3	0	-8/3	0	8/3	0	-4/3	-10/3	0
EJ	0	8/9	2/9	8/9	0	-4/9	0	2/9	-4/9	0

(continued next page)

Table 3.1 (continued)

Matrix  
Element  
( $\beta\gamma$ )

Integration Point ( $\alpha$ )  $\rightarrow$

	A	B	C	D	E	F	G	H	I	J
FF	3	4/3	4/3	1/3	1/3	7/3	0	0	4/3	12
FG	1/3	-1/9	-2/9	1/9	1/18	-5/9	0	0	1/9	-2/3
FH	0	0	1/3	-2/3	-1/6	5/3	0	0	-2/3	3
FI	0	2/3	0	2/3	1/3	-5/3	0	0	-5/3	-6
FJ	-2/3	-4/9	-2/9	-2/9	-1/9	4/9	0	0	-2/9	-11/3
GG	4/27	1/27	4/27	4/27	1/27	4/27	121/27	4/27	1/27	4/27
GH	0	0	-2/9	-2/9	-1/9	-4/9	-11/3	4/9	-2/9	-2/3
GI	0	-1/18	0	2/9	1/18	4/9	11/6	-2/9	-1/18	4/3
GJ	-2/27	1/27	1/27	-2/27	-1/54	-2/27	-11/27	1/27	1/27	-11/27
HH	0	0	1/3	4/3	1/3	4/3	12	7/3	4/3	3
HI	0	0	0	-4/3	-1/6	-4/3	-6	1/3	1/3	-6
HJ	0	0	-1/18	4/9	1/18	2/9	4/3	-1/18	-2/9	11/6
II	0	1/3	0	4/3	1/3	4/3	3	4/3	7/3	12
IJ	0	-2/9	0	-4/9	-1/9	-2/9	-2/3	-2/9	4/9	-11/3
JJ	4/27	4/27	1/27	4/27	1/27	4/27	4/27	1/27	4/27	121/27

The integration weights,  $w_\alpha$ , are given by equation (3.42) with  $h = 1$ . The above equation has been derived in the case that each minor triangle has side of length 1. If instead each minor triangle has side  $h$ , equation (3.53) is modified to read

$$\iint_{\Delta} dx dy \left[ \left( \frac{\partial P_3(x,y)}{\partial x} \right)^2 + \left( \frac{\partial P_3(x,y)}{\partial y} \right)^2 \right] = \frac{1}{h^2} \sum_{\alpha\beta\gamma} w_\alpha R_{\alpha\beta\gamma} g_\beta g_\gamma \quad (3.54)$$

where  $w_\alpha$  is given in equation (3.42).

The above formula is valid if the integration region consists of a single major triangle. If there are several major triangles, some of the weights must be added as was done for Figure 3.3. The function  $g(\beta_x, \beta_y)$  has been used to represent  $A_{\lambda JK}(\beta_x, \beta_y)$ . Hence

$$\iint d\beta_x d\beta_y \sum_{s=x,y} \left| \frac{\partial A_{\lambda JK}(\beta_x, \beta_y)}{\partial \beta_s} \right|^2 = \frac{1}{h^2} \sum_{\alpha\beta\gamma} [w_\alpha R_{\alpha\beta\gamma} A_{\lambda JK; \beta}^* A_{\lambda JK; \gamma}] \quad (3.55)$$

Finally the expectation of the vibrational kinetic energy can be evaluated numerically to yield

$$\begin{aligned} \langle \psi_{\lambda JM} | \hat{T}_{vib} | \psi_{\lambda JM} \rangle &= \frac{1}{2B} \frac{1}{h^2} \sum_{\alpha} w_{\alpha} Q_{\alpha} \left\{ \sum_{\beta\gamma} R_{\alpha\beta\gamma} \right. \\ &\quad \times \sum_K (A_{\lambda JK; \beta}^* A_{\lambda JK; \gamma}) \} \end{aligned} \quad (3.56)$$

#### IV. Numerical Methods: Rotational Energy

##### 1. Boundary Conditions

The triangular grid in the  $\beta$ - $\gamma$  plane is illustrated in Figure 3.1. There are conditions on the wavefunction along each of the three sides of the triangle. First we consider the case  $J \neq 0$ . Along the line  $\gamma = 0$  (or equivalently  $\beta_y = 0$ ) the wavefunction must be zero. As a

result, the rotational part of the Hamiltonian becomes axially symmetric about the 3-axis and  $K$  becomes a good quantum number. Another way to see this is, along the line  $\gamma = 0$ , the quantity  $r$  in equation (3.19-iii) becomes equal to zero. Hence the matrix elements coupling different values of  $K$  (see equation (3.25)) are zero. The rotational energy of the wavefunction with good  $K$  becomes proportional to  $pJ(J+1) + (q-p)K^2$ . (See equation (3.24).)

However near  $\gamma = 0$  the third moment of inertia approaches zero:

$$\mathcal{I}_3(\beta, \gamma) = 4B\beta^2 \sin^2 \gamma = 4B\beta_Y^2. \quad (3.57)$$

Hence  $q = \frac{1}{2\mathcal{I}_3} \rightarrow \infty$  as  $\beta_Y \rightarrow 0^+$ . The quantity  $p$  remains well behaved. Using equation (3.33), the dominant term in the integrand of the expression for the rotational energy of a given  $K \neq 0$  component becomes

$$I = Q(\beta_x, \beta_y) |A_{\lambda JK}(\beta_x, \beta_y)|^2 \frac{K^2}{2\mathcal{I}_3(\beta_x, \beta_y)} \quad (3.58)$$

near  $\beta_y = 0$ .  $Q(\beta_x, \beta_y) = 2B^{5/2} \beta_y (3\beta_x^2 - \beta_y^2) \propto \beta_y$  near  $\beta_y = 0$ .

Also  $\mathcal{I}_3 \propto \beta_y^2$  near  $\beta_y = 0$ . Hence

$$I \propto K^2 |A_{\lambda JK}(\beta_x, \beta_y)|^2 / \beta_y \quad (3.59)$$

near  $\beta_y = 0$ . To keep the expression for the rotational energy finite it is necessary that

$$A_{\lambda JK}(\beta, \gamma=0) = 0 \quad \text{if } K \neq 0. \quad (3.60)$$

Along the line  $\gamma = \pi/3$  the moment of inertia  $\mathcal{I}_2 = 0$ .

To avoid a singularity in the energy the following conditions hold:

$$\frac{\sqrt{1+\delta_{K0}} A_{\lambda JK}(\beta, \gamma=\pi/3)}{D_{K0}^J(\pi/2, \pi/2, \pi)} = \frac{A_{\lambda JK+2}(\beta, \gamma=\pi/3)}{D_{K+20}^J(\pi/2, \pi/2, \pi)} \quad (3.61)$$

Kumar and Baranger have derived equations (3.61) (KB 67) using complicated symmetry arguments. A new and simpler derivation is given in Appendix F.

At the origin  $\beta = 0$ , equation (3.59) implies

$$A_{\lambda JK}(\beta=0, \gamma) = A_{\lambda JK}(\beta=0, \gamma=0) = 0 \text{ if } K \neq 0 \quad (3.62)$$

$$\therefore A_{\lambda JK}(\beta=0, \gamma=\pi/3) = 0 \text{ if } K \neq 0. \quad (3.63)$$

Combining this equation with equations (3.61) we obtain

$$A_{\lambda JK=0}(\beta=0, \gamma=\pi/3) = 0. \quad (3.64)$$

Summarizing;

$$A_{\lambda JK}(\beta=0, \gamma) = 0 \text{ for all } K. \quad (3.65)$$

Collecting together the above results, we obtain the following boundary conditions for  $J \neq 0$ :

$$A_{\lambda JK}(\beta, \gamma=0) = 0 \text{ if } K \neq 0 \quad (3.66-i)$$

$$\frac{\sqrt{1+\delta_{K0}} A_{\lambda JK}(\beta, \gamma=\pi/3)}{D_{K0}^J(\pi/2, \pi/2, \pi)} = \frac{A_{\lambda JK+2}(\beta, \gamma=\pi/3)}{D_{K+20}^J(\pi/2, \pi/2, \pi)} \quad (3.66-ii)$$

$$A_{\lambda JK}(\beta=0, \gamma) = 0 \text{ for all } K. \quad (3.66-iii)$$

For  $J=0$ , none of the above arguments based on the

finiteness of the energy apply. The only condition is that the wavefunction be smooth. As a result

$$\left. \frac{\partial A_{J=0}}{\partial \beta_x} \right|_{\beta=0} = \left. \frac{\partial A_{J=0}}{\partial \beta_y} \right|_{\beta=0} = 0 \quad (3.67)$$

Otherwise the wavefunction would have a cusp at the origin.

## 2. Structure of the Hamiltonian Matrix

The expressions for the expectation value of the energy, equations (3.30), (3.33), (3.43) and (3.56) are recast as follows:

$$\langle \psi_{\lambda JM} | \hat{H}_B | \psi_{\lambda JM} \rangle = \sum_{K\alpha} \sum_{K'\alpha'} A_{K\alpha}^* H_{(K,\alpha)(K',\alpha')} A_{K'\alpha'} \quad (3.68)$$

Here  $\alpha$  and  $\alpha'$  label the grid points in the  $\beta$ - $\gamma$  plane. The subscripts for the total angular momentum  $J$ ,  $z$  component  $M$  and additional quantum numbers  $\lambda$  have been dropped for the sake of compactness.

The Hamiltonian consists of three parts:

$$H_{(K,\alpha)(K',\alpha')} = T_{(K,\alpha)(K',\alpha')}^{\text{rot}} + T_{(K,\alpha)(K',\alpha')}^{\text{vib}} + V_{(K,\alpha)(K',\alpha')} \quad (3.69)$$

$$T_{(K,\alpha)(K',\alpha')}^{\text{rot}} = \delta_{\alpha\alpha'} w_\alpha Q_\alpha \langle \phi_{MK}^J | \hat{T}_{\text{rot}} | \phi_{MK}^J \rangle \quad (3.70)$$

where the moments of inertia  $\mathcal{I}_\nu(\beta_x, \beta_y)$  in  $\hat{T}_{\text{rot}}$  are evaluated at the grid point  $\alpha$ . Equation (3.70) is diagonal with respect to  $\alpha\alpha'$  since no derivative with respect to  $\beta_x$  or  $\beta_y$  are involved in this term.

$$T_{(K,\alpha)(K',\alpha')}^{\text{vib}} = \delta_{KK'} \frac{1}{2B} \frac{1}{h^2} \sum_\beta w_\beta Q_\beta R_{\beta\alpha\alpha'} \quad (3.71)$$

where this term is diagonal with respect to  $KK'$  since the vibrational term has no dependence on the Euler angles. Finally,

$$V_{(K,\alpha)(K',\alpha')} = \delta_{KK'} \delta_{\alpha\alpha'} w_{\alpha} Q_{\alpha} V_{\alpha} \quad (3.72)$$

where  $V_{\alpha}$  is the value of  $V(\beta_x, \beta_y)$  at the grid point  $\alpha$ . The normalization condition (equation (3.44)) becomes

$$\sum_{K,\alpha} \sum_{K',\alpha'} A_{K\alpha}^* F_{(K,\alpha)(K',\alpha')} A_{K'\alpha'} = 1 \quad (3.73)$$

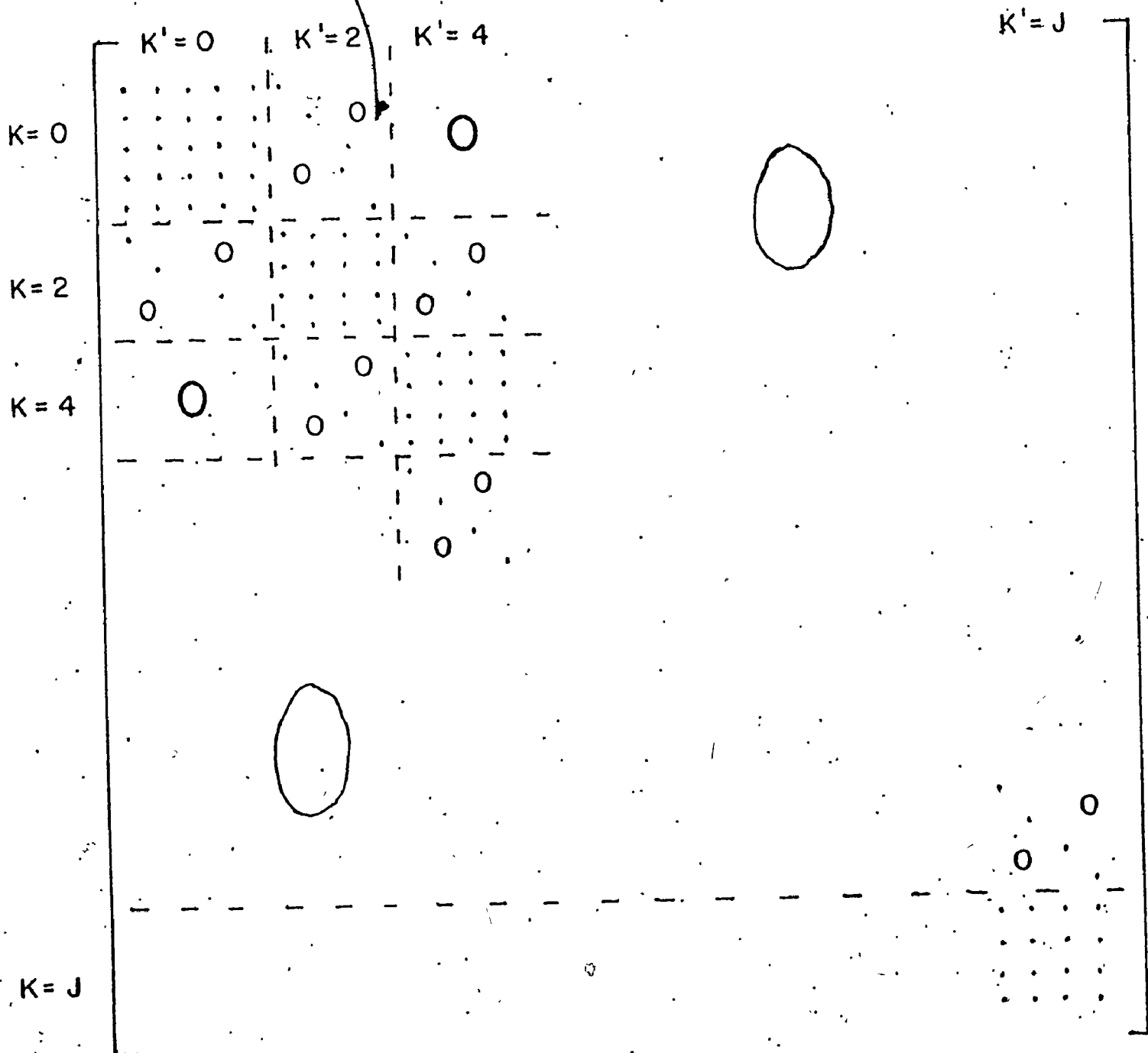
where

$$F_{(K,\alpha)(K',\alpha')} = \delta_{KK'} \delta_{\alpha\alpha'} w_{\alpha} Q_{\alpha} \quad (3.74)$$

The ordered pairs  $(K,\alpha)$  where  $\alpha$  ranges over the grid points and  $K = (0), 2, 4, 6, \dots, J$  are ordered so  $K$  varies most slowly. Then the quantities  $H_{(K,\alpha)(K',\alpha')}$  can be arranged in a matrix as in Figure 3.4. Since the matrix elements vanish unless  $K = K', K' \pm 2$ , the Hamiltonian matrix  $H$  is block tri-diagonal. The off-diagonal blocks (for which  $K = K' \pm 2$ ) are themselves diagonal blocks. They contain only rotational matrix elements. The vibrational matrix elements are contained in the diagonal blocks. The potential matrix elements all lie along the main diagonal.

The boundary conditions allow the dimensionality of  $H$  to be reduced slightly. Because of the condition given by equation (3.66-i), certain terms in the summation in equation (3.68) are zero. As a result the rows in  $H$  corresponding to grid points on the  $\gamma=0$  line can be removed. Since the matrix

Figure 3.4



Block structure of Hamiltonian matrix. Most of the matrix elements in this matrix are zero. The matrix elements which, in general, do not vanish are indicated by dots.



$\tilde{H}$  is symmetric, the corresponding columns also must be removed. Similarly the condition at the origin (equation (3.66-iii)) allows one row and one column to be removed from the  $K = K' = 0$  block. The matrix  $\tilde{H}$  could be truncated even further if the conditions in equation (3.66-ii) were used. This was not done because if it were,  $\tilde{H}$  would no longer be block tri-diagonal. It is essential for  $\tilde{H}$  to be block tri-diagonal for the methods described in the following section to be valid.

In the actual calculations, 190 grid points were used. The use of equation (3.66-iii) reduces the dimensionality of the  $K=0$  block to 189. After the use of equation (3.66-i), the dimensionalities of the  $K \neq 0$  blocks are each reduced to 171. The calculations have been limited to  $J \leq 20$ . For the worst case, namely  $J = 20$ , there are 10  $K \neq 0$  components and hence the dimensionality of  $\tilde{H}$  is  $189 + 10 \times 171 = 1899$ .

## V. Construction and Diagonalization of the Hamiltonian

### 1. Construction of the eigenvalue equation

The basic variational equation to be solved (see equation (3.29)) is

$$\delta \sum_{K, \alpha} \sum_{K', \alpha'} A_{K\alpha}^* H(K, \alpha) (K', \alpha') A_{K'\alpha'} = 0 \quad (3.75-i)$$

The normalization constraint is

$$\sum_{K, \alpha} \sum_{K', \alpha'} A_{K\alpha}^* F(K, \alpha) (K', \alpha') A_{K'\alpha'} = 1 \quad (3.75-ii)$$

where

$$F(K, \alpha) (K', \alpha') = \delta_{KK'} \delta_{\alpha\alpha'} w_{\alpha} Q_{\alpha} \quad (3.75-iii)$$

Roman letters  $i, j$  are introduced to represent the ordered pairs  $(K, \alpha)$ , ie.  $i \equiv (K, \alpha)$ . Then the above equations become

$$\delta \sum_{ij} A_i^* H_{ij} A_j = 0 \quad (3.76-i)$$

with

$$\sum_i A_i^* F_i A_i = 1 \quad (3.76-ii)$$

Use has been made of the fact that  $F_{(K, \alpha)(K', \alpha')}$  is diagonal.

Using the Lagrange multiplier technique the above two equations yield the generalized eigenvalue equation

$$\sum_j H_{ij} A_j = E F_i A_i \quad (3.77)$$

To diagonalize matrices as large as  $1899 \times 1899$  as required for the  $J = 20$  case, it is wise to use the Lanczos algorithm (Whi 72, Wil 65). However, this algorithm is used to solve the standard eigenvalue problem, not the generalized eigenvalue problem. Equation (3.77) can be converted into an ordinary eigenvalue equation with the following substitutions:

$$\bar{H}_{ij} \equiv H_{ij} / \sqrt{F_i F_j} \quad (3.78)$$

and

$$\bar{A}_i \equiv \sqrt{F_i} A_i \quad (3.79)$$

Then equations (3.77) and (3.76-ii) become respectively

$$\sum_j \bar{H}_{ij} \bar{A}_j = E \bar{A}_i \quad (3.80-i)$$

and

$$\sum_i |\bar{A}_i|^2 = 1 \quad (3.80-ii)$$

It is now clear why the Kumar and Baranger integration weights can not be used. About one quarter of the integration weights they used were exactly zero. This would cause equation (3.78) to be nonsense. Using a cubic numerical integration formula, all the weights  $w_\alpha$  are positive. Unfortunately the integration densities  $Q_\alpha$  become zero at the  $\gamma = 0$  and  $\gamma = \pi/3$  boundaries. From equation (3.75-ii) it can be seen that some of the  $F_i$  in equation (3.78) will be zero. This problem is discussed in the next section.

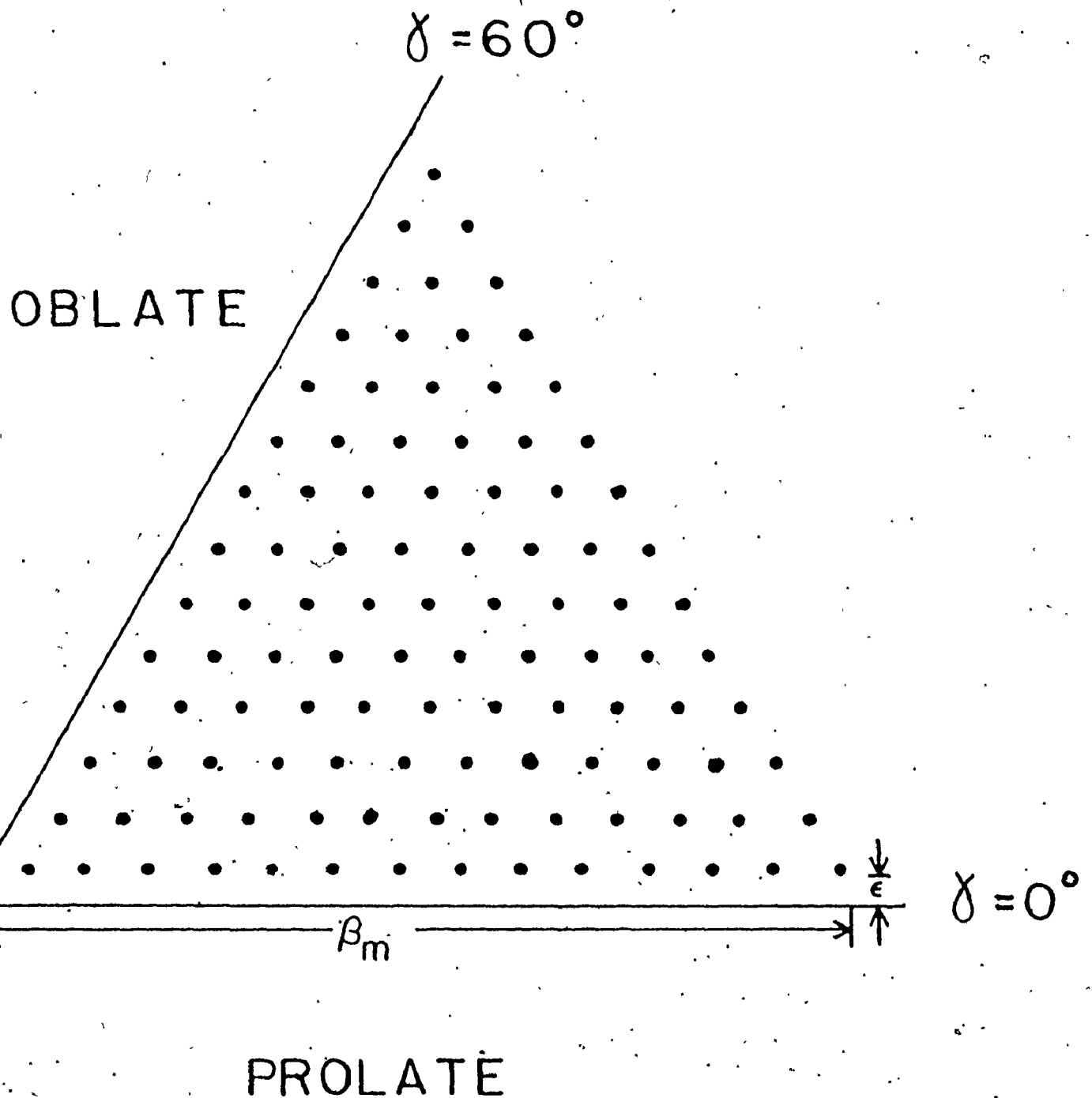
## 2. Divergence of Matrix Elements of $\bar{H}$

In the previous section it was noted that matrix elements of  $\bar{H}$ , corresponding to grid points on the  $\gamma = 0$  and  $\gamma = \pi/3$  lines, become infinite. To alleviate this problem, the integrations in the  $\beta$ - $\gamma$  plane are performed within a slightly smaller region. This triangular integration region is separated from the  $\gamma = 0$  and  $\gamma = \pi/3$  lines by an amount  $\epsilon$ . This is illustrated in Figure 3.5. Within the slightly smaller integration region, the value of the integration density at each grid point,  $Q_\alpha$ , is positive. Hence the matrix elements of  $\bar{H}$  are all finite. It is found that a reasonable value for  $\epsilon$  is  $\epsilon = 0.08 h = 0.0042 \beta_m$ .

## 3. Lanczos Algorithm

About twenty-five years ago, Lanczos (Lan 52) proposed a procedure for tri-diagonalizing ~~matrices~~. Unfortunately this procedure is numerically unstable necessitating the use

Figure 3.5



Grid points showing cut-off parameter  $\epsilon$ . This diagram is not to scale.

of reorthogonalization. Since, then, to tri-diagonalize matrices, the Lanczos algorithm (Wil 65) has been replaced by the Householder method (Hou 64) which is more efficient. Recently Sebe and Nachamkin (SN 69) and Whitehead (Whi 72) have resurrected the Lanczos algorithm for use in a slightly different context with widespread applications in science. In this new context the Lanczos procedure is used to calculate the highest few and the lowest few eigensolutions of very large matrices. Although the intermediate eigensolutions can not be calculated in this method, this is compensated for by the fact that the procedure is very fast.

The Lanczos algorithm is an iterative procedure. For a symmetric matrix this procedure, after  $r$  iterations, generates an  $r \times r$  symmetric tri-diagonal matrix  $M_r$ . The extreme few eigenvalues of  $M_r$  approximate the extreme few eigenvalues of the original matrix. The approximation improves after each iteration. The very highest and the very lowest eigenvalues converge after a small number of iteration steps. The next to the extreme eigenvalues converge after a few more iteration steps, etc. The upper and lower ends of the spectrum normally converge at about the same rate although this could be affected by the density of eigenvalues. In particular isolated eigenvalues converge rather rapidly.

It was found that the convergence of the lowest eigenvalues of the Hamiltonian matrix  $\tilde{H}$  was slow. To rectify this problem, the Lanczos procedure was used to evaluate the eigen-

solutions of the inverse matrix  $\bar{H}^{-1}$ . The eigenvalues of  $\bar{H}$  are just the reciprocals of the eigenvalues of  $\bar{H}^{-1}$  and the eigenvectors of the two matrices are identical. The states of physical interest correspond to the lowest eigensolutions of  $\bar{H}$  or the highest eigensolutions of  $\bar{H}^{-1}$ . The zero of the energy scale is given so that  $\bar{H}$  is positive definite. The spectrum of  $\bar{H}^{-1}$  is bounded below by zero and above by  $1/E_0$  where  $E_0$  is the lowest eigenvalue of  $\bar{H}$ . Then the eigensolutions of physical interest, namely the highest few eigenvalues of  $\bar{H}^{-1}$  are well separated. Hence they converge relatively rapidly. It is found that 30 iterations is sufficient to give the highest three eigenvalues of  $\bar{H}^{-1}$  accurate to six significant figures for all cases considered.

To simplify notation we define the matrix  $A = \bar{H}^{-1}$ .  $A$  can be a very large matrix; in the present work  $A$  can have dimensionality as large as  $1899 \times 1899$ . The procedure for finding the eigensolutions of the symmetric  $n \times n$  matrix is as follows. First  $|v_1\rangle$ , an arbitrary normalized vector of dimensionality  $n$ , is chosen. A new (unnormalized) vector  $|u_1\rangle$  is obtained by the matrix multiplication of  $|v_1\rangle$  with  $A$ :

$$|u_1\rangle = A|v_1\rangle. \quad (3.81)$$

But  $|u_1\rangle$  can be decomposed into two components:

$$|u_1\rangle = |v_1\rangle \langle v_1 | u_1 \rangle + \beta_1 |v_2\rangle. \quad (3.82)$$

Here  $|v_2\rangle$  has also been normalized. Clearly  $|v_2\rangle$  is orthogonal to  $|v_1\rangle$ . (We assume  $|v_1\rangle$  is not an eigenvector of  $A$ .) Defining

$\alpha_1 \neq \langle v_1 | u_1 \rangle$ , equation (3.81) can be written

$$A|v_1\rangle = \alpha_1|v_1\rangle + \beta_1|v_2\rangle. \quad (3.83,1)$$

This process can be continued, yielding for the  $i$ th iteration a new orthogonal vector  $|v_{i+1}\rangle$  and two new coefficients  $\alpha_i$  and  $\beta_i$ :

$$A|v_2\rangle = \beta_1|v_1\rangle + \alpha_2|v_2\rangle + \beta_2|v_3\rangle \quad (3.83,2)$$

where  $|v_3\rangle$  is orthogonal to  $|v_1\rangle$  and to  $|v_2\rangle$  by similar arguments.

$$A|v_3\rangle = \beta_2|v_2\rangle + \alpha_3|v_3\rangle + \beta_3|v_4\rangle. \quad (3.83,3)$$

There is no term involving  $|v_1\rangle$  because

$$\langle v_1 | A | v_3 \rangle = \langle v_3 | A | v_1 \rangle = \alpha_1 \langle v_3 | v_1 \rangle + \beta_1 \langle v_3 | v_1 \rangle = 0.$$

This process is finally terminated with the  $n$ th vector  $|v_n\rangle$  associated with the space of the  $n \times n$  matrix  $A$  to give

$$A|v_n\rangle = \beta_{n-1}|v_{n-1}\rangle + \alpha_n|v_n\rangle. \quad (3.83,n)$$

The vectors  $|v_i\rangle$  form an orthonormal basis in which  $A$  is symmetric and tri-diagonal:

$$\langle v_i | A | v_i \rangle = \alpha_i \quad \langle v_{i+1} | A | v_i \rangle = \beta_i$$

$$\langle v_{i-1} | A | v_i \rangle = \beta_{i-1}$$

$$\langle v_{i+k} | A | v_i \rangle = 0 \quad \text{if} \quad k \geq 2. \quad (3.84)$$

The crucial point of the Lanczos algorithm is that it is not necessary to carry out all  $n$  iterations given in equation (3.83) in order to find the physically interesting solutions. It is possible to stop after  $r < n$  steps yielding the tri-diagonal  $r \times r$  matrix  $M_r$  defined below.

$$M_{\approx r} = \begin{pmatrix} \alpha_1 & \beta_1 & & & \\ \beta_1 & \alpha_2 & \beta_2 & & 0 \\ 0 & \beta_2 & \alpha_3 & \beta_4 & \\ & & \dots & & \\ 0 & & & \dots & \\ & & & & \beta_{r-1} & \alpha_r \end{pmatrix} \quad (3.85)$$

If  $r$  is sufficiently large, the extreme eigenvalues of  $A$  are virtually the same as the extreme eigenvalues of  $M_{\approx r}$ . Moreover, the extreme eigenvectors of  $A$  are simply related to the extreme eigenvectors of  $M_{\approx r}$ . In actual practice  $r$  is never larger than 25. Diagonalizing a symmetric tridiagonal  $25 \times 25$  matrix is a routine task.

Whitehead (Whi 72) has suggested the following technique to speed convergence for the highest eigensolutions. A random normalized vector is chosen. Then this vector is multiplied several times by the matrix  $A$ . (It has been found that 5 such preiterations is a reasonable choice.) After normalization the resultant vector is used as vector  $|v_1\rangle$  in equations (3.83). The preiteration has the effect of building into  $|v_1\rangle$  large components of the highest few eigenvectors of  $A$ .

Because the Lanczos algorithm is numerically unstable, the sequence of vectors  $|v_1\rangle, |v_2\rangle, \dots, |v_r\rangle$  may not all be orthogonal to each other. This instability requires that each new vector  $|v_i\rangle$  be made explicitly orthogonal to all the previously calculated vectors  $|v_1\rangle, |v_2\rangle, \dots, |v_{i-1}\rangle$ . The



Gram-Schmidt process is used to obtain the required orthogonality.

The Lanczos algorithm consists of two basic procedures. The first consists of evaluation of inner products such as  $\langle v_1 | u_1 \rangle$ . To minimize round-off error, these sums must be done very carefully. The second basic procedure is the multiplication of the vector by a matrix, for example,  $|u_1\rangle = A|v_1\rangle$ . The Dirac notation of quantum mechanics has been used in the previous equations to illustrate the fact that the above equation can be regarded as an operator equation. Given an initial state  $|v_1\rangle$  it is necessary only to be able to evaluate the resultant state  $|u_1\rangle$  after the action of  $A$  on  $|v_1\rangle$ . Very often it is not necessary to do the matrix multiplication explicitly. That is, it may not be necessary to calculate  $\sum_{\alpha'=1}^n A_{\alpha\alpha'} \langle \alpha' | v_1 \rangle$ ,  $\alpha = 1, 2, \dots, n$  to obtain the components of  $|u_1\rangle$ . As a result, time and storage size is reduced. In the present work, the matrix elements  $A_{\alpha\alpha'}$  are not used, nor are they known. Moreover, they could not be conveniently calculated. Avoiding a matrix multiplication is especially useful if the matrix is sparse (contains a large number of zeroes).

In summary, the Lanczos algorithm has two main advantages. First, it can deal with very large matrices in a reasonable amount of time. Second, storage requirements are reduced since it is not necessary to deal with all  $n^2$  matrix elements.

#### 4. Solution of Linear Equations

As has been stated, the use of the Lanczos algorithm requires the evaluation of a new vector by the operation of a matrix on a given vector. In the present application, the matrix is  $\bar{H}^{-1}$ . Given a prescribed arbitrary vector  $\underline{y}$ , it is necessary to calculate

$$\underline{x} = \bar{H}^{-1} \underline{y} . \quad (3.86)$$

However the matrix inversion required to obtain  $\bar{H}^{-1}$  is an  $n^3$  process. Since  $\bar{H}$  can be as large as  $1899 \times 1899$ , the evaluation of  $\bar{H}^{-1}$  is a prohibitive task. Ko (Ko 74) has pointed out that equation (3.86) is equivalent to solving the system of linear inhomogeneous equations

$$\bar{H} \underline{x} = \underline{y} . \quad (3.87)$$

Ko (Ko, 74) has shown that since the coefficient matrix,  $\bar{H}$ , is block tri-diagonal, equations (3.87) can be readily solved using a special technique. The Lanczos algorithm is modified to use (3.87) as a basic step and then used to evaluate the highest few eigensolutions of  $\bar{H}^{-1}$ . However, at no time are the matrix elements of  $\bar{H}^{-1}$  even known or used.

Changing the notation slightly, we wish to solve equation (3.87):

$$\bar{H} \underline{x} = \underline{f} \quad (3.88)$$

where  $\underline{f}$  is one of the Lanczos vectors  $\underline{v}_i$ . The matrix  $\bar{H}$  is a

block matrix. Its block structure (for even  $J$ ) is illustrated in Figure 3.4. The first (upper-left) sub-matrix on the diagonal has dimensionality  $189 \times 189$ . It is represented by  $G_1$ . The rest of the sub-matrices on the diagonal are each  $171 \times 171$ . They are represented by  $G_m$ ,  $m = 2, 3, \dots, M$ .

The vectors  $f$  and  $x$  can each be broken up into a group of sub-vectors. Each sub-vector corresponds to a particular block. This is written

$$\tilde{x} = \begin{bmatrix} x^{(1)} \\ \tilde{x}^{(2)} \\ \vdots \\ \tilde{x}^{(M)} \end{bmatrix} \quad \text{and} \quad \tilde{f} = \begin{bmatrix} f^{(1)} \\ \tilde{f}^{(2)} \\ \vdots \\ \tilde{f}^{(M)} \end{bmatrix} \quad (3.89)$$

The sub-vectors  $x^{(1)}$  and  $f^{(1)}$  each have 189 components. The rest of the sub-vectors each have 171 components. The only other sub-matrices with non-vanishing elements are those adjacent to the diagonal sub-matrices. The super-diagonal sub-matrices are represented by  $C_m$ ,  $m=1, 2, \dots, M$  with  $C_1$  adjacent to  $G_1$ ,  $C_2$  adjacent to  $G_2$ , etc. The first such matrix is not square: it has dimensionality  $189 \times 171$ . The rest of the matrices  $C_m$ ,  $m=2, 3, \dots, M-1$  are square and are also diagonal. They each have dimensionality  $171 \times 171$ . Although  $C_1$  has more rows than columns, it closely resembles a diagonal matrix. Each column in  $C_1$  contains exactly one non-zero matrix element. For these

non-zero matrix elements, the row index increases monotonically with increasing column index. This kind of sub-matrix can be described as "pseudo-diagonal".

The system of linear equations in equation (3.88) is solved using block matrix techniques. Since the matrix  $\bar{H}$  is block tri-diagonal, considerable simplification results. The method of solution is analogous to that used for an ordinary (non-block) tri-diagonal matrix: Gaussian elimination followed by back substitution. The manipulations are performed on the sub-matrices intact instead of on individual matrix elements. This block matrix technique is described by Isaacson and Keller (IK 66) for a non-symmetric block tri-diagonal matrix with square sub-matrices on the main diagonal. The matrix  $\bar{H}$  is much less general than the block matrix considered by Isaacson and Keller. First,  $\bar{H}$  is symmetric. Second, the super and sub-diagonal sub-matrices are either diagonal or "pseudo-diagonal". These two factors cause even more simplification.

A sequence of matrices  $D_m$  and  $E_m$  are defined as follows:

$$(189 \times 189) \quad D_1 = G_1 \quad (3.90)$$

$$(189 \times 189) \quad E_1 = D_1^{-1} \quad (3.91)$$

$$(171 \times 171) \quad D_2 = G_2 - C_1^T E_1 C_1 \quad (3.92)$$

$$(171 \times 171) \quad E_m = D_m^{-1} \quad (3.93)$$

$$(171 \times 171) \quad D_{m+1} = G_{m+1} - C_m^T E_m C_m \quad (3.94)$$

$$(171 \times 171) \quad E_M = D_M^{-1} \quad (3.95)$$

The dimensionalities of the above matrices are given at the left. Next a sequence of auxiliary sub-vectors is defined:

$$(189) \quad \underline{y}^{(1)} = \underline{E}_1 \underline{f}^{(1)} \quad (3.96-i)$$

$$(171) \quad \underline{y}^{(2)} = \underline{E}_2 (\underline{f}^{(2)} - \underline{C}_1^T \underline{y}^{(1)}) \quad (3.96-ii)$$

$$(171) \quad \underline{y}^{(m)} = \underline{E}_m (\underline{f}^{(m)} - \underline{C}_{m-1} \underline{y}^{(m)}), \quad m = 3, 4, \dots, M \quad (3.96-iii)$$

The dimensionalities of the above sub-vectors is given at left.

Finally the solution is obtained:

$$(171) \quad \underline{x}^{(M)} = \underline{y}^{(M)} \quad (3.97-i)$$

$$(171) \quad \underline{x}^{(m)} = \underline{y}^{(m)} - \underline{E}_m \underline{C}_m \underline{x}^{(m+1)}, \quad m = M-1, M-2, \dots, 2 \quad (3.97-ii)$$

$$(189) \quad \underline{x}^{(1)} = \underline{y}^{(1)} - \underline{E}_1 \underline{C}_1 \underline{x}^{(2)} \quad (3.97-iii)$$

In terms of computer time, the most costly part of the whole process is the evaluation of the sub-matrix inverses in equations (3.90) to (3.95). For the most cumbersome case, namely  $J = 20$ , there are eleven inverses to be calculated. Fortunately these inverses depend only on  $\underline{H}$ . They do not depend on the Lanczos vector  $\underline{f}$  which will be different for each iteration of the Lanczos procedure. As a result, the matrix inverses are calculated and stored once before the iteration process begins. For each iteration, the quantities  $\underline{y}^{(m)}$  and  $\underline{x}^{(m)}$  have to be calculated. However this involves only vector addition, multiplication of sub-matrices by sub-vectors and the evaluation of inner products. It does not involve multiplication of two matrices or even worse, matrix inversion. Hence each iteration step can be done relatively quickly.

## VI. Electromagnetic Multipole Moments

### 1. Electric Quadrupole Moments

Information on the nuclear wavefunction can be gained by measuring the electromagnetic properties of the nucleus. Lifetimes of states which are unstable to gamma-ray emission can be measured. The magnitude and sometimes the sign of the electric moments can be measured. It is also possible to deduce the average nuclear shape from measurements of transition rates (C1i 71).

Since the Bohr collective model is based on quadrupole shape co-ordinates, the electric quadrupole moment is particularly easy to calculate. The electric quadrupole moment operator is

$$\hat{Q}_{2\mu} = \sum_p e_p r_p^2 Y_{2\mu}(\theta_p, \phi_p) \quad (3.98)$$

where the sum is over the co-ordinates of the protons with the co-ordinates expressed in polar co-ordinates in the laboratory system. It is convenient to express the electric quadrupole operator in terms of quadrupole operators  $\hat{Q}$  defined in the body-fixed principal axis system. If a collective wavefunction has definite  $\beta$  and  $\gamma$ , then it has definite quadrupole moments. Assuming a uniform charge distribution they are, to first order in  $\beta$ ,

$$Q_0'(\beta, \gamma) \equiv \langle \beta\gamma | \hat{Q}_{20}' | \beta\gamma \rangle = \frac{3}{4\pi} e Z R_0^2 \beta \cos \gamma \quad (3.99-i)$$

$$Q_1'(\beta, \gamma) \equiv \langle \beta\gamma | \hat{Q}_{2\pm 1}' | \beta\gamma \rangle = 0 \quad (3.99-ii)$$

$$Q_2'(\beta, \gamma) \equiv \langle \beta\gamma | \hat{Q}_{2\pm 2}' | \beta\gamma \rangle = \frac{3}{4\pi} e Z R_0^2 \frac{\beta \sin \gamma}{\sqrt{2}} \quad (3.99-iii)$$

Using the well known transformation properties of spherical tensors the expectation value of  $\hat{Q}_{2\mu}$  can be expressed in terms of  $Q'_0(\beta, \gamma)$  and  $Q'_2(\beta, \gamma)$ . The result is (KB 67)

$$\langle \lambda J M | \hat{Q}_{2\mu} | \lambda' J' M' \rangle = \begin{Bmatrix} J & 2 & J' \\ -M & \mu & M' \end{Bmatrix} \langle \lambda J || \hat{Q}_2 || \lambda' J' \rangle \quad (3.100)$$

where the reduced matrix element is defined as

$$\langle \lambda J || \hat{Q}_2 || \lambda' J' \rangle = (-1)^J \sqrt{(2J+1)(2J'+1)} \quad (3.101)$$

$$\begin{aligned} & \times \sum_K \begin{Bmatrix} J & 2 & J' \\ -K & 0 & K \end{Bmatrix} \langle A_{\lambda J K} | Q'_0 | A_{\lambda J' K} \rangle + \sqrt{1+\delta_{K0}} \\ & \times \left[ \begin{Bmatrix} J & 2 & J' \\ -K-2 & 2 & K \end{Bmatrix} \langle A_{\lambda J K+2} | Q'_2 | A_{\lambda J' K} \rangle + (-1)^{J+J'} \begin{Bmatrix} J & 2 & J' \\ K & 2 & -K-2 \end{Bmatrix} \right. \\ & \left. \langle A_{\lambda J K} | Q'_2 | A_{\lambda J' K+2} \rangle \right] \end{aligned}$$

Of experimental interest is the spectroscopic quadrupole moment. It is defined as follows:

$$Q(\lambda J) \equiv \sqrt{\frac{16\pi}{5}} \langle \lambda J M=J | \hat{Q}_{20} | \lambda J M=J \rangle. \quad (3.102)$$

Using equations (3.100) and (3.101) and inserting explicit algebraic expressions for the 3-j symbols, the spectroscopic quadrupole moment can be written

$$\begin{aligned} Q(\lambda J) &= \sqrt{\frac{16\pi}{5}} \begin{Bmatrix} J & 2 & J \\ -J & 0 & J \end{Bmatrix} \langle \lambda J || \hat{Q}_2 || \lambda J \rangle \\ &= \sqrt{\frac{16\pi}{5}} [(2J+3)(J+1)]^{-1} \sum_K [(3K^2 - J(J+1))] \langle A_{\lambda J K} | Q'_0 | A_{\lambda J K} \rangle \\ &+ \sqrt{6(1+\delta_{K0})} (J-K-1)(J-K)(J+K+1)(J+K+2) \langle A_{\lambda J K+2} | Q'_2 | A_{\lambda J K} \rangle \quad (3.103) \end{aligned}$$

## 2. Gamma-ray Transition Rates

Another quantity of experimental interest is the lifetime of a state. The lifetime is merely the reciprocal of the transition rate. A very important transition in the collective model is the transition  $J+2 \rightarrow J$  where initial and final states have positive parity. This transition is of E2 multipolarity. The following expression gives the transition rate:

$$T_{J+2 \rightarrow J} = \frac{4\pi}{75\hbar} \left(\frac{\omega}{c}\right)^5 B(E2; \lambda' J+2 \rightarrow \lambda J) \quad (3.104)$$

where  $\omega$  is the angular frequency of the emitted photon. The symbol  $B(E2; \lambda' J+2 \rightarrow \lambda J)$  represents the reduced transition probability. It is defined by

$$B(E2; \lambda' J' \rightarrow \lambda J) = \frac{1}{2J'+1} \sum_{M, M'} |\langle \lambda J M | \hat{Q}_{2r} | \lambda' J' M' \rangle|^2 \quad (3.105)$$

Combining equations (3.100) and (3.105), the reduced transition probability can be written in terms of the reduced matrix element as follows:

$$B(E2; \lambda' J' \rightarrow \lambda J) = \frac{1}{2J'+1} |\langle \lambda' J' || \hat{Q}_2 || \lambda J \rangle|^2 \quad (3.106)$$

Using equation (3.101), the reduced transition probability is given by (KB 67)

$$\begin{aligned} B(E2; \lambda' J+2 \rightarrow \lambda J) = & [(2J+2)(2J+3)(2J+4)(2J+5)]^{-1} \cdot (3.107) \\ & \times \left( \sum_K \left[ \sqrt{6(J+K+2)(J+K+1)(J-K+1)(J-K+2)} \langle A_{\lambda JK} | Q_0' | A_{\lambda' JK} \rangle \right. \right. \\ & + \sqrt{1+\delta_{KO}} \left\{ \sqrt{(J-K-1)(J-K)(J-K+1)(J-K+2)} \langle A_{\lambda JK+2} | Q_2' | A_{\lambda' J+2K} \rangle \right. \\ & \left. \left. + \sqrt{(J+K+1)(J+K+2)(J+K+3)(J+K+4)} \langle A_{\lambda JK} | Q_2' | A_{\lambda' J+2K+2} \rangle \right\} \right) \end{aligned}$$



The integrations over  $\beta$  and  $\gamma$  in equations (3.101), (3.103) and (3.107) are done numerically. For example

$$Q'_O(\beta, \gamma) \equiv \frac{3}{4\pi} e Z R_O^2 \beta \cos \gamma = \frac{3}{4\pi} e Z R_O^2 \beta_x. \quad (3.108)$$

Hence

$$\begin{aligned} & \langle A_{\lambda JK} | Q'_O | A_{\lambda' J' K'} \rangle \\ & \equiv \int d\beta_x d\beta_y Q(\beta_x, \beta_y) A_{\lambda JK}^*(\beta_x, \beta_y) \frac{3}{4\pi} e Z R_O^2 \beta_x A_{\lambda' J' K'}(\beta_x, \beta_y) \\ & = \frac{3}{4\pi} e Z R_O^2 \sum_{\alpha} [w_{\alpha} Q_{\alpha} A_{\lambda JK; \alpha}(\beta'_x)_{\alpha} A_{\lambda' J' K'; \alpha}] \end{aligned} \quad (3.109)$$

The numerical integration weights  $w_{\alpha}$  are given in Figure 3.3.

In the case that the rotor Hamiltonian is axially symmetric,  $K$  becomes a good quantum number. Then for an intra-band transition, equation (3.107) simplifies to

$$B(E2; J+2, K+JK) = \frac{3(J+K+2)(J+K+1)(J-K-1)(J-K+2)}{(J+1)(2J+3)(2J+4)(2J+5)} |Q_{JK}|^2 \quad (3.110-i)$$

where

$$Q_{JK} = \langle A_{\lambda JK} | Q'_O | A_{\lambda JK} \rangle. \quad (3.110-ii)$$

If the limiting case of a rigid rotor is assumed, then  $Q_{JK}$  becomes independent of  $J$ . This is the usual approximation made for a rotational band. The transition rates within the band have the simple dependence on  $J$  given by equation (3.110-i). An important special case of this model involves the ground state band. The transitions within a  $K=0$  band of an axially symmetric rigid rotor are

$$B(E2; J+2 \rightarrow J) = \frac{3}{2} \frac{(J+1)(J+2)}{(2J+3)(2J+5)} |Q_{J0}|^2 \quad (3.111)$$

where  $Q_{J0}$  does not depend on  $J$ . In the next chapter, equation (3.111) will be compared with the more general case given by equation (3.107).

So far very little has been said about magnetic dipole transitions.  $M1$  transitions are forbidden for purely collective transitions of second order in even-even nuclei because of the high degree of symmetry present (WJ 56).

## CHAPTER 4

### BOHR'S COLLECTIVE MODEL: RESULTS

#### I. Test of Method: Spherical Harmonic Oscillator

##### 1. Energy Levels

To test the accuracy of the numerical method outlined in the previous chapter, the Bohr collective Hamiltonian is solved for two extreme cases: a spherical oscillator and a well-deformed prolate rotor. In both cases the Bohr inertial functions are used. The two cases are distinguished by the choice of the collective potential energy  $V(\beta, \gamma)$ .

An idealized model of a "vibrational" nucleus is obtained by substituting into the Bohr collective Hamiltonian the potential

$$V(\beta, \gamma) = \frac{1}{2} C \beta^2 \quad (4.1)$$

The resulting energies, wavefunctions and electromagnetic moments are known analytically (Bes 59). These analytic results are given here to allow a comparison with the numerical method.

The Yrast energies for even  $J$  are given by

$$E_J = \left( \frac{J+3}{2} + m + (m-1)\delta_{J0} \right) \omega \quad (4.2)$$

where  $\omega = \sqrt{C/B}$  (4.3)

and  $m = 1, 2, 3$  for the Yrast state, first excited state and second excited state respectively. The stiffness parameter  $C$

is defined in equation (4.1). The inertial parameter  $B$  is defined in equations (3.8) and (3.9). Following Kumar and Baranger the values  $B = 100 \text{ Mev}^{-1}$  and  $C = 100 \text{ Mev}$  were chosen.

In addition to  $B$  and  $C$ , there are three numerical parameters:  $\epsilon$ ,  $N_g$  and  $\beta_m$ .  $\epsilon$  is the cut-off parameter defined in Chapter 4, Section V-2. Since the solutions are rather insensitive to  $\epsilon$ , no further discussion of this parameters is presented.  $N_g$  is the number of grid points used in the mesh. Energies of a harmonic oscillator for different angular momenta are plotted in Figure 4.1. It is found that a mesh consisting of 190 grid points is fine enough. Normally the deviation from the exact value is largest for the first excited state above the Yrast state. The maximum deviation from the analytic result is 1.5%.  $\beta_m$  is the maximum value of  $\beta$  used in the mesh in the  $\beta$ - $\gamma$  plane. For each  $J$ , the optimal value of  $\beta$  is different. This point is illustrated in Figure 4.2.

Analytic expressions for the wavefunctions can be given (KB 67). For example the intrinsic wavefunctions for  $J = 0$ ,  $J = 0'$  respectively are

$$A_{J=0}(\beta, \gamma) = \left(\frac{4\omega^5}{\pi}\right)^{1/4} \exp\left(-\frac{1}{2} \frac{\beta^2}{b^2}\right) \quad (4.4)$$

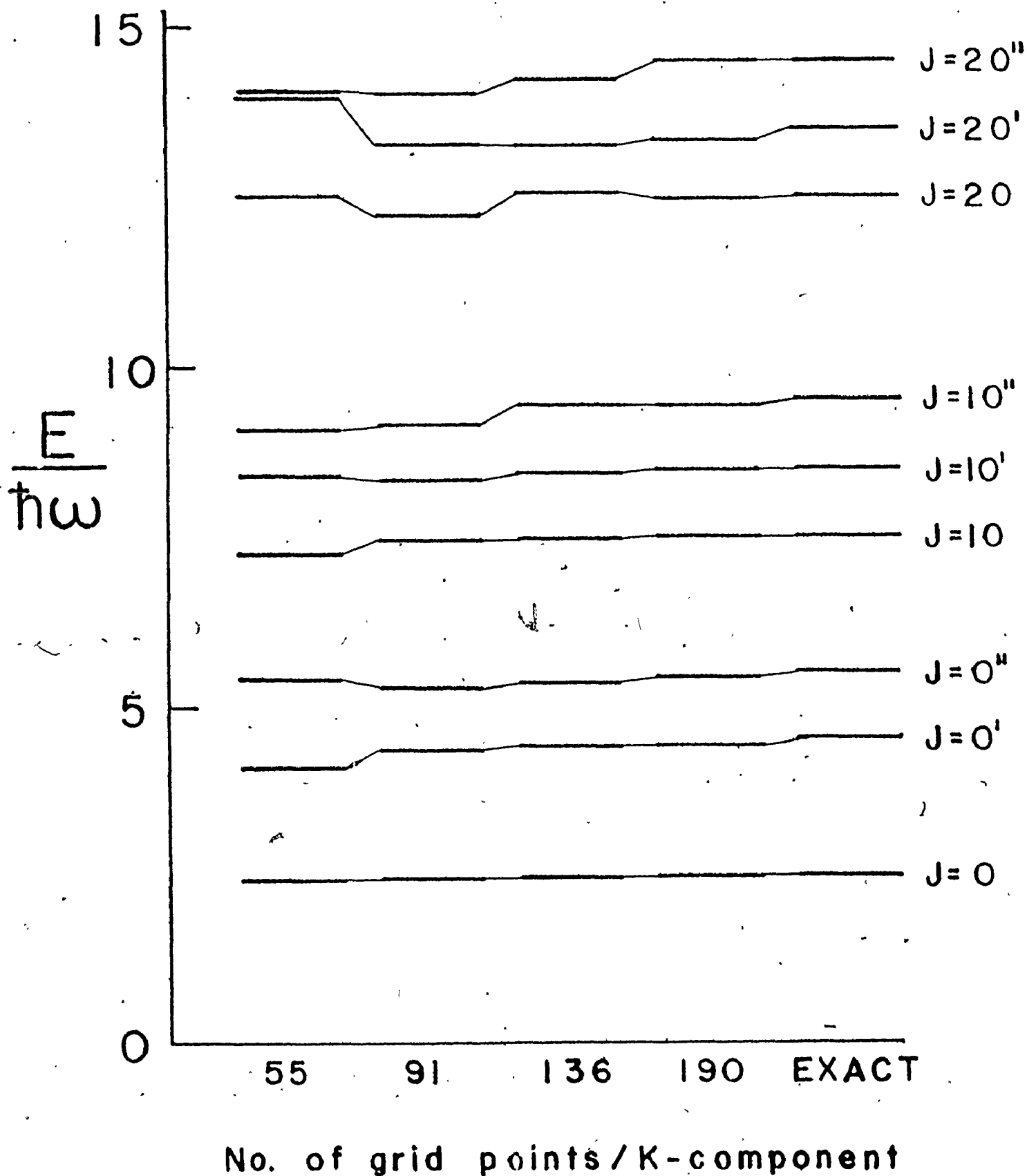
$$A_{J=0'}(\beta, \gamma) = \left(\frac{25\omega^5}{\pi}\right)^{1/4} \left(1 - \frac{2}{5} \frac{\beta^2}{b^2}\right) \exp\left(-\frac{1}{2} \frac{\beta^2}{b^2}\right) \quad (4.5)$$

where

$$b = (BC)^{-1/4}. \quad (4.6)$$

The plot of these expressions are compared with the plot of the wavefunctions obtained numerically in figures 4.3 and 4.4.

Energy levels of a harmonic oscillator. The three lowest energies for  $J = 0, 10,$  and  $20$  are calculated using meshes of different fineness. The analytically known exact result is also given.



Energy levels of a harmonic oscillator. The same energy levels as in Figure 4.1 except the maximum value of  $\beta$ ,  $\beta_m$  is varied while the number of grid points is kept constant (= 190). The arrows mark the optimal value of  $\beta_m$  for  $J = 0, 10, 20$ .

Figure 4.2

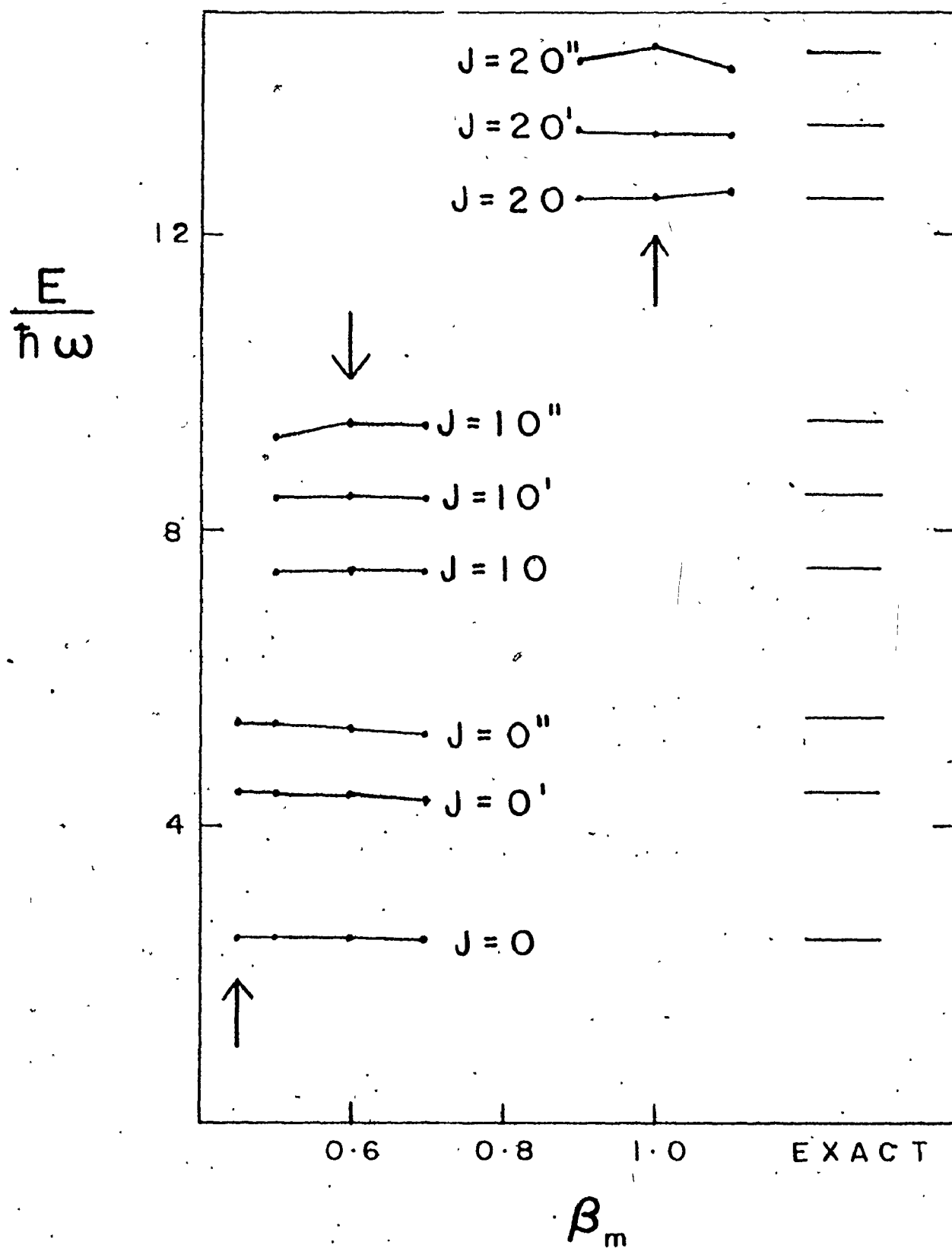
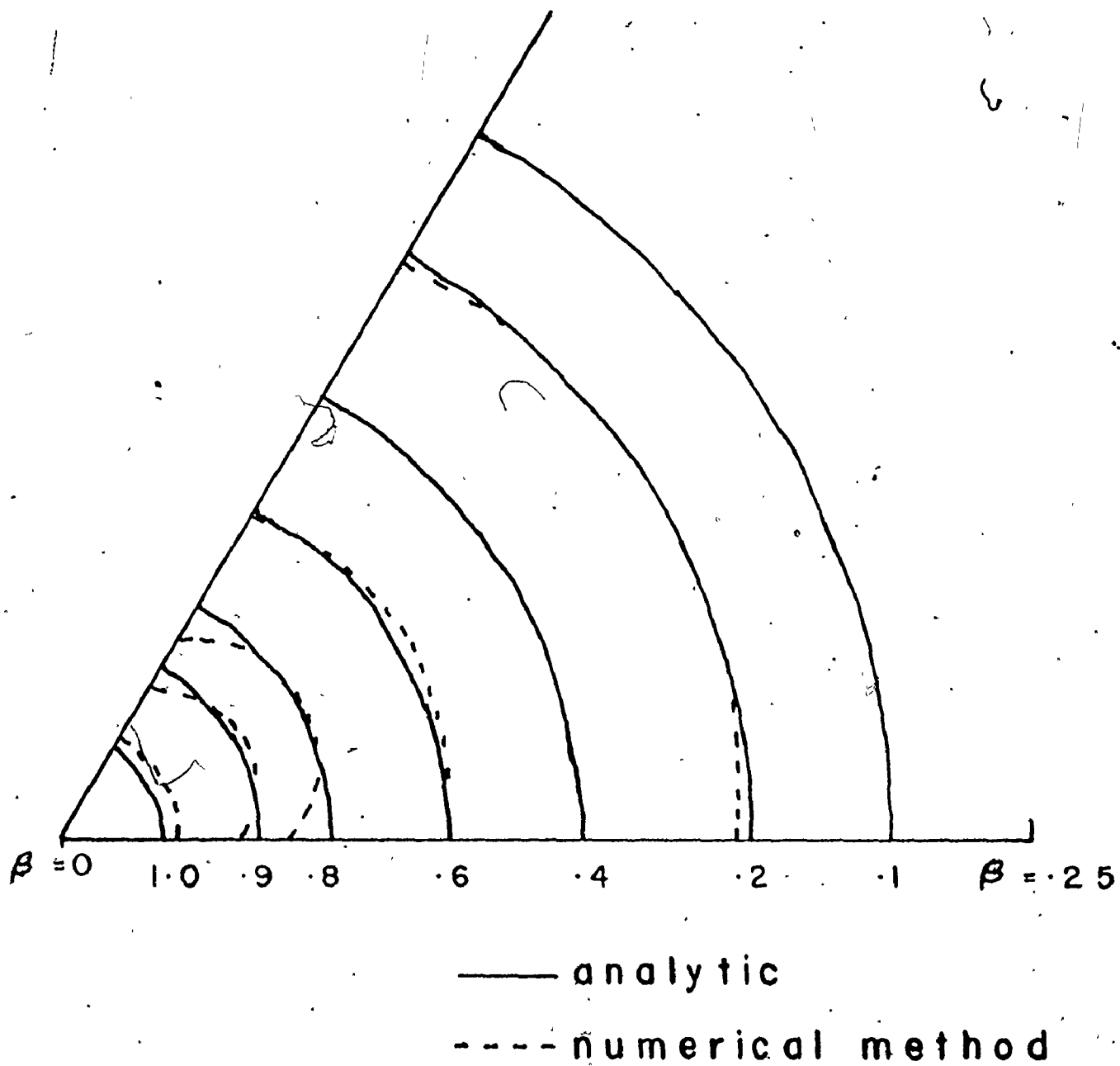


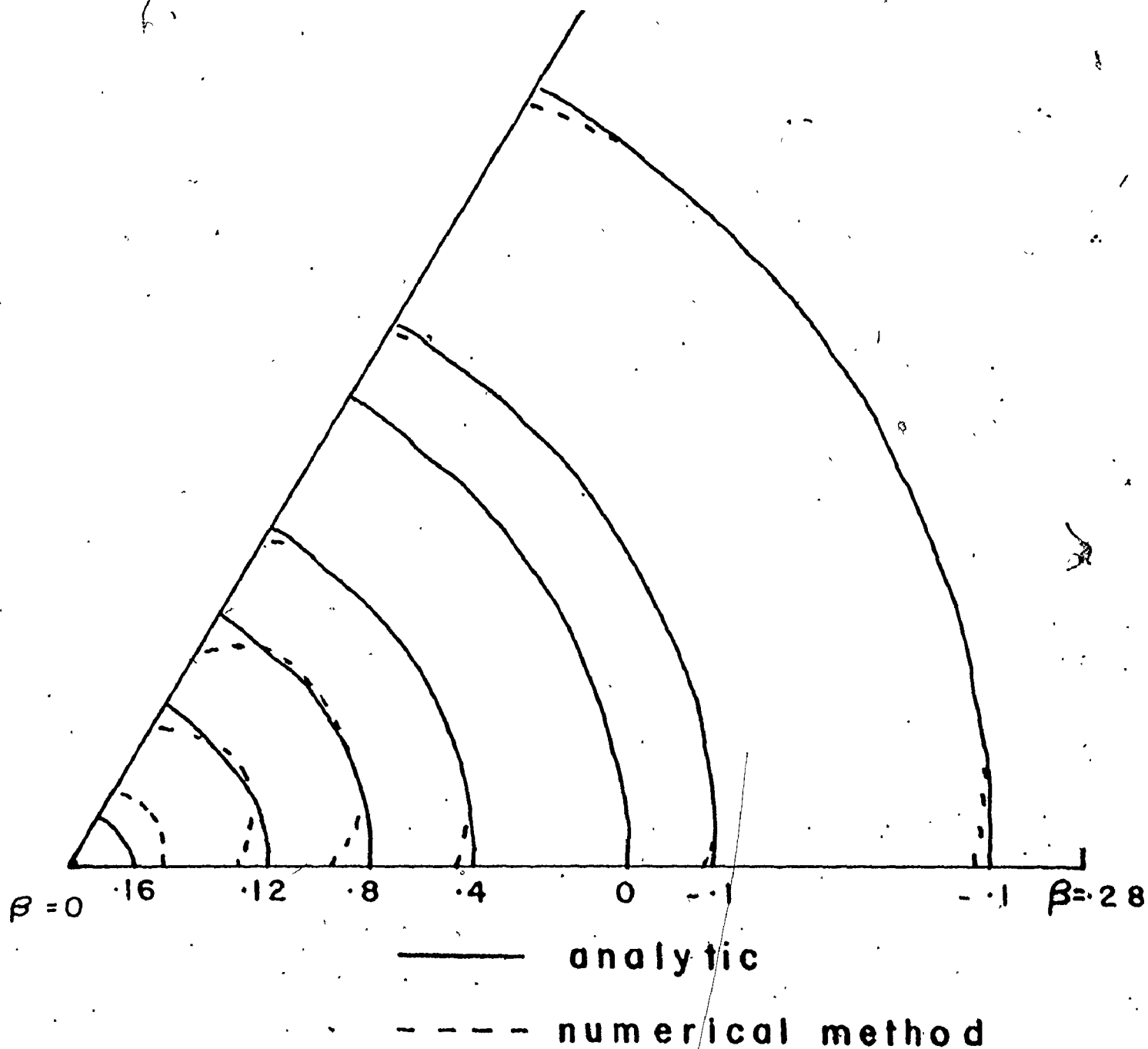


Figure 4.3



Wavefunction of  $J=0$  state of harmonic oscillator. This is a contour plot of  $A_{J=K=0}(\beta, \gamma)$

Figure 4.4



Wavefunction of  $J=0$  state of harmonic oscillator. As in Figure 4.3, this is a contour plot of  $A_{J=0}(\beta, \gamma)$ .

Again values of  $B = 100 \text{ Mev}^{-1}$  and  $C = 100 \text{ Mev}$  were chosen.

This gives an oscillator length of  $b = 0.1$ . In both cases  $\beta_m$  was taken to be 0.45 although not all the  $\beta$ - $\gamma$  sector is shown. The deviation of the numerical wavefunction from the corresponding analytic wavefunction is most severe near the  $\gamma = 0$  and  $\gamma = \pi/3$  boundaries, especially when  $\beta$  is small. It is clear that energies are obtained more reliably than wavefunctions.

Finally, analytic expressions for the  $B(E2)$ 's can be given. Some examples are

$$B(E2; 2 \rightarrow 0) = \frac{9}{32\pi^2} e^2 z^2 R_0^4 b^2 \equiv T \quad (4.7-i)$$

$$B(E2; 2 \rightarrow 0') = \frac{2}{5} T \quad (4.7-ii)$$

$$B(E2; 2 \rightarrow 2') = 2T \quad (4.7-iii)$$

$$B(E2; 4 \rightarrow 2) = 2T \quad (4.7-iv)$$

To compare our results with those of KB, we have considered the same situation; namely  $Z = 50$ ,  $R_0 = 6 \text{ fm}$  and, as before,  $b = 0.1$ . Table 4.1 gives the results:

Table 4.1

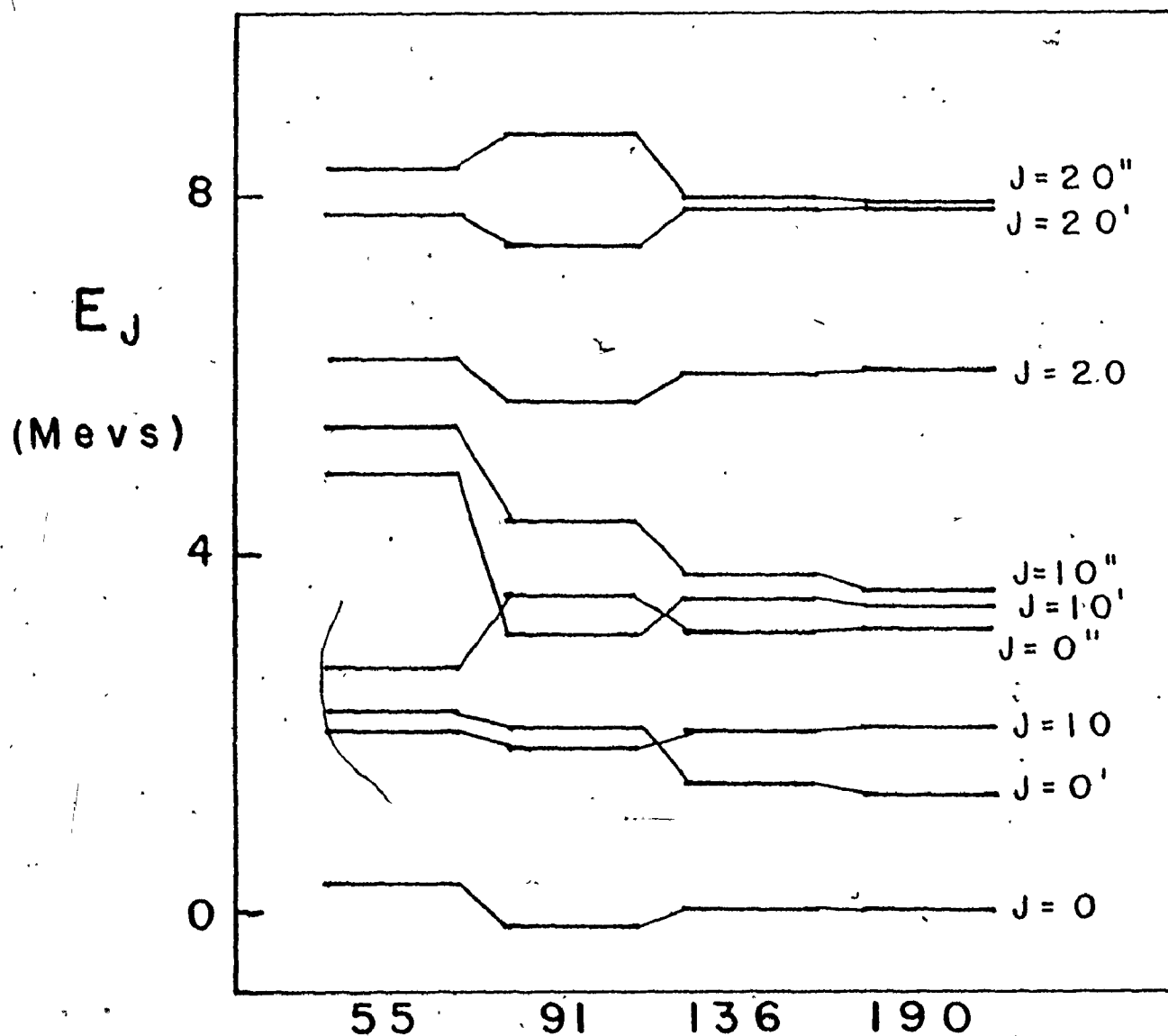
Transition	<u>B(E2)'s for Harmonic Oscillators</u>		
	This method ( $e^2 \text{-barn}^2$ )	KB ( $e^2 \text{-barn}^2$ )	Exact ( $e^2 \text{-barn}^2$ )
$2 \rightarrow 0$	0.0910	0.0915	0.0923
$2 \rightarrow 0'$	0.0375	0.0382	0.0369
$2' \rightarrow 2$	0.1836	0.1854	0.1847
$4 \rightarrow 2$	0.1836	0.1854	0.1847

The maximum deviation of our results from the analytic result is 1.6%. It is fortunate that the quantities of direct experimental interest, namely energies and transition rates, are obtained much more accurately than the wavefunction. The inaccuracies in the wavefunction are, in some sense, "smeared out" in evaluating expectation values such as energies and electromagnetic moments.

## II. Test of Method: Deformed Prolate Rotor

The other test case investigated is that of a well-deformed prolate rotor. The collective potential has a fairly deep minimum at  $\beta = 0.314$  and  $\gamma = 0$ . This is a stringent test on the accuracy of our procedure for the following reason. A common method of solving the Bohr collective Hamiltonian includes expanding the wavefunction in the basis of eigenstates of a harmonic oscillator. Because the wavefunction of a well-deformed rotor is quite different from a harmonic oscillator, a large number of basis states is required. For computational reasons there is a maximum size for the basis. If the solution has not converged by the time that the size of the basis has increased to its computational limit, the method has failed. Our numerical method does not suffer from this specific convergence difficulty. However there is a related difficulty. If the rotor is well-deformed, it is necessary to use a large  $\beta_m$ . Since the maximum number of grid points is 190, this means that the mesh becomes relatively coarse. If the intrinsic wavefunc-

Figure 4.5



Energy levels of a prolate rotor. The lowest three energies for  $J = 0, 10$  and  $20$  are calculated as a function of the number of grid points per K component. Reasonable convergence is obtained for the finest mesh.

tion has a lot of structure, the numerical differentiations and integrations will be inaccurate.

The actual potential used is similar to that of Myers and Swiatecki (MS 66).

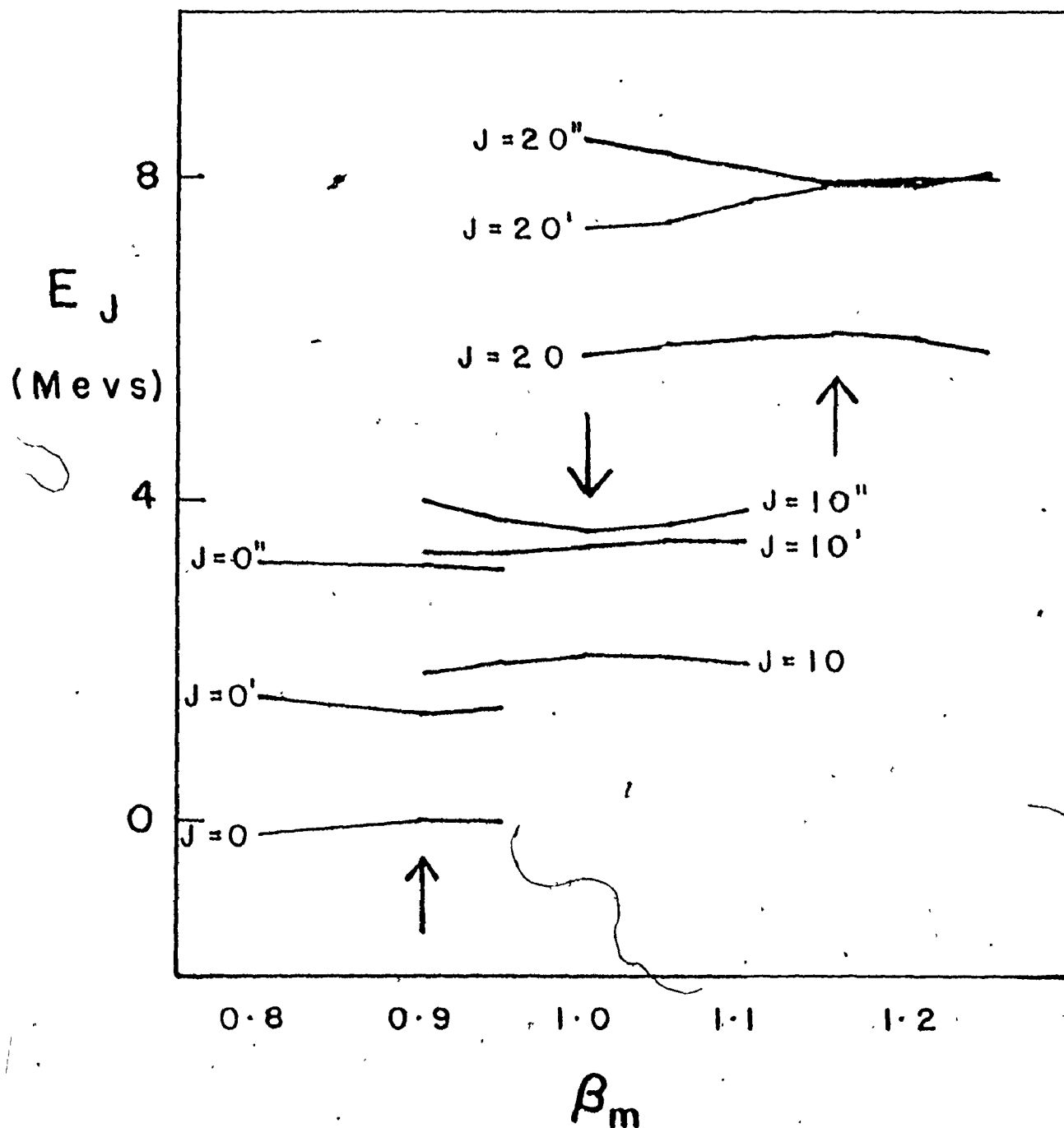
$$V(\beta, \gamma) = \frac{1}{2} C \beta^2 + (h_0 - h_1 (\beta/a)^3 \cos 3\gamma) \exp(-\beta^2/a^2) - V_1 \beta^3 \cos 3\gamma \quad (4.8)$$

where  $C = 150$  Mev,  $h_0 = 13$  Mev,  $h_1 = 11$  Mev,  $V_1 = 20$  Mev and  $a = 0.3$  fm. The Bohr inertial parameters are used with  $B = 100$  Mev<sup>-1</sup>.

The energy levels are plotted in Figure 4.5 as a function of grid size. It can be seen that 190 grid points give reasonable convergence. The energies also depend, to a certain extent, on the value of  $\beta_m$ . This is shown in Figure 4.6.

For even angular momentum  $J$ , the intrinsic wavefunction has components with  $K = 0, 2, 4, \dots, J$ . For odd  $J$ , the components are  $K = 2, 4, 6, \dots, J-1$ . If the collective potential favours a prolate solution, the probability that the wavefunction has a large  $K$  is small. As a result, it is a good approximation to restrict the wavefunction to having  $K$  components no higher than some maximum  $K$ , say  $K_{\max}$ . In all the results presented in this section,  $K_{\max} = 8$  (instead of  $J$ ). That this is a good approximation can be seen by examining Table 4.2.

Figure 4.6



Energy levels of a prolate rotor. The same energy levels as in Figure 4.5 except the maximum value of  $\beta$ ,  $\beta_m$ , is varied while the number of grid points is kept constant (=190).

Table 4.2

Probability that Wavefunction Has  $J_3 = K$

$J \backslash K$	0	2	4	6	8
10	0.9181	0.0810	0.0009	0.0000	0.0000
10'	0.2732	0.7088	0.0178	0.0002	0.0000
10''	0.7718	0.2236	0.0046	0.0000	0.0000
20	0.6753	0.3031	0.0208	0.0008	0.0000
20'	0.7781	0.1942	0.0256	0.0020	0.0001
20''	0.3723	0.4646	0.1517	0.0110	0.0004

### III. Features of Band Crossing

Practically, all theories of backbending involve a crossing of the ground state band with another band having a larger effective moment of inertia. Such theories differ in their interpretation of the nature of this second band. The severity of the irregularity at the backbending point (on an  $I-\omega^2$  plot) is increased when the difference between the effective moments of inertia of the two bands is increased. The severity of the backbending is also enhanced if there is very little mixing between the two bands. The amount of mixing is also connected with the transition rate (for emission of gamma rays) as the nucleus de-excites along the Yrast states at the band crossing. It is expected that very little mixing will result in a retardation of the transition rate.



There are several different explanations of the nature of the ~~second~~ band. It is difficult to choose between these theories because of the paucity of data on the low spin members of this postulated second band. It is expected that such states will be weakly fed by a gamma cascade after a (HI,xn) reaction because of the  $(\Delta E)^5$  factor in the E2 transition rate. Andrews et.al. (AWG+ 74) have argued that backbending is an artifact of the feeding following (HI,xn) reactions. If it were possible to measure the energies of all the states in both bands, each band would be well behaved (with no backbending) on an  $\sqrt{-\omega^2}$  plot. Since the so-called Yrast band is not a band at all but is in fact two bands, backbending is observed.

The above arguments are complicated somewhat by the presence of the  $\beta$ -band. Backbending in the  $\beta$ -band has been observed in  $Gd^{154}$  and  $Dy^{156}$  (WGG+ 73, KBB+ 73, AWG+ 74, LBD+ 74). It is hypothesized that the backbending in the  $\beta$ -band is caused by a crossing of the  $\beta$ -band with a higher "third band" or "super band". Unfortunately the states in this band below the crossing point are not observed. This "three band theory" also postulates that the super band first crosses the  $\beta$ -band and then, at higher spin, crosses the ground state band. Because the super band and the ground state band intersect at a slight angle, states in both bands both above and below the crossing are fed. Hence it is possible to trace the ground state band through the crossing. As a result, the ground state band does not backbend.

Most theories describe the second band (in the case of  $Gd^{154}$ ,  $Dy^{156}$  the third band) in microscopic terms. In this thesis, we investigate a possible collective nature to this band. Central to the whole concept is the role of gamma deformation (deviation from axial symmetry).

#### IV. Choice of Inputs

##### 1. Inertial Parameter

The Bohr collective Hamiltonian has, as inputs, several inertial functions as well as a potential function. As stated before, this investigation has used the Bohr inertial functions which contain a single parameter  $B$ . To obtain a value for  $B$ , use is made of a semi-empirical relation developed by Grodzins (Gro 62). Grodzins observed that throughout the periodic table for even-even nuclei, there is a relationship between the transition rate of the gamma decay  $J = 2 \rightarrow J = 0$  and the excitation energy of the  $J = 2$  state. Stated mathematically, this relationship is

$$T(2 \rightarrow 0) = ((3 \pm 1) \times 10^{10} E^4 Z^2 / A) \quad (4.9)$$

where the excitation energy  $E$  is in Mev's and the transition rate in  $\text{sec}^{-1}$ . For the rare earth nuclei, a better value is

$$T(2 \rightarrow 0) = ((3.5 \pm 0.5) \times 10^{10} E^4 Z^2) / A. \quad (4.10)$$

Assuming that the nucleus behaves as an axially symmetric rigid rotor, the Bohr model predicts the transition rate. Using equations (3.104), (3.111) and (3.99-i), we have

$$T(2 \rightarrow 0) = \frac{3}{500\pi} \frac{e^2}{\hbar} \left( \frac{E}{\hbar c} \right)^5 Z^2 R_0^4 \beta^2. \quad (4.11)$$

Comparing equations (4.10) and (4.11) yields

$$E = \frac{1190}{\beta^2 A^{7/3}}. \quad (4.12)$$

Since the excitation energy of a rigid axially symmetric rotor is  $E = \frac{2 \times 3}{6B^2}$ , we finally obtain

$$B = \frac{A^{7/3}}{1190} \text{ Mev}^{-1} \quad (4.13)$$

This equation is used to define B in all the results that follow.

## 2. Potential Surface

For the specific nuclei discussed in the next few sections, collective potential surfaces have been determined so as to give a qualitative fit to the available data. It is difficult in practice to find the potential which should give an almost exact fit to the data although such a potential should exist in principle. For each nucleus, the important data are the energies of the  $J=2$ ,  $J=4$ ,  $J=2'$  and  $J=0'$  states as well as the critical angular momentum,  $J_c$ , at which the nucleus displays backbending. In this model, backbending is ascribed to a sudden shape change resulting from the crossing of two collective bands. In order for backbending to take place, it is necessary that there not be a great deal of mixing between the two bands. In order for this to be the case, it was found necessary to use a potential surface with two minima.

In most cases, the data indicates approximate axial symmetry for the lowest states in the ground state band. This suggests the potential surface has a minimum on either the prolate or oblate axis. The Bohr Hamiltonian has the symmetry that if  $V(\beta, \gamma)$  is replaced by  $V(\beta, \pi/3 - \gamma)$ , the eigenenergies are unchanged. This means that it is impossible to distinguish between even-even prolate or oblate nuclei in this model. Hence

there is no loss of generality to take one of the two minima to lie along the prolate axis.

For the second minimum, two possibilities are investigated. In one case the second minimum is taken to lie in the region of maximal axial asymmetry ( $\gamma = \pi/6$ ). The rationale for this comes from the study of the VMIA model. By becoming axially asymmetric, the nucleus can take advantage of the  $3/4$  factor in the energy described in equation (2.48). The argument against such a choice for the second minimum is that normal Strutinsky calculations do not predict a minimum here. However more modern Strutinsky calculations (which include the Coriolis field using a term  $\omega J_1$ ) indicate the possibility of an asymmetric minimum.

The other situation investigated is a potential having a second minimum on the oblate axis. In this case there is no factor of  $3/4$  to encourage the nucleus to move over to the second minimum. Hence to get backbending, it is necessary that the second (oblate) minimum have a larger  $\beta$  associated with it than the first minimum. A situation similar to this has already been investigated by Ross and Nogami (RN 73). In their simple stretching model there was a  $\beta$  degree of freedom but no  $\gamma$  degree of freedom. By using a two minima potential, they obtained backbending. However to avoid quantum-mechanical mixing between the two minima, the two minima had to be well separated. As a result, unrealistically large transition rates were predicted between states above the backbending point. This problem is not

as serious in our work because the two minima can be well separated in the  $\gamma$  direction. In fact, using a second oblate minimum was suggested by Ross and Nogami.

The  $\beta$  corresponding to the first minimum is mainly determined by the energy of the  $J=2$  state. The energy of the  $\beta$  bandhead gives information about the curvature of the potential in the  $\beta$  direction. Information on the "stiffness" of the potential is also obtained by the slope of the experimental  $I-\omega^2$  at  $\omega = 0$ . The energy of the  $\gamma$  bandhead gives information on the curvature of the potential in the  $\gamma$  direction. Finally the  $\beta$  of the second minimum is determined so that the two bands cross at the experimentally known critical angular momentum. The data puts strong constraints on the potential surface. However it is still not uniquely determined.

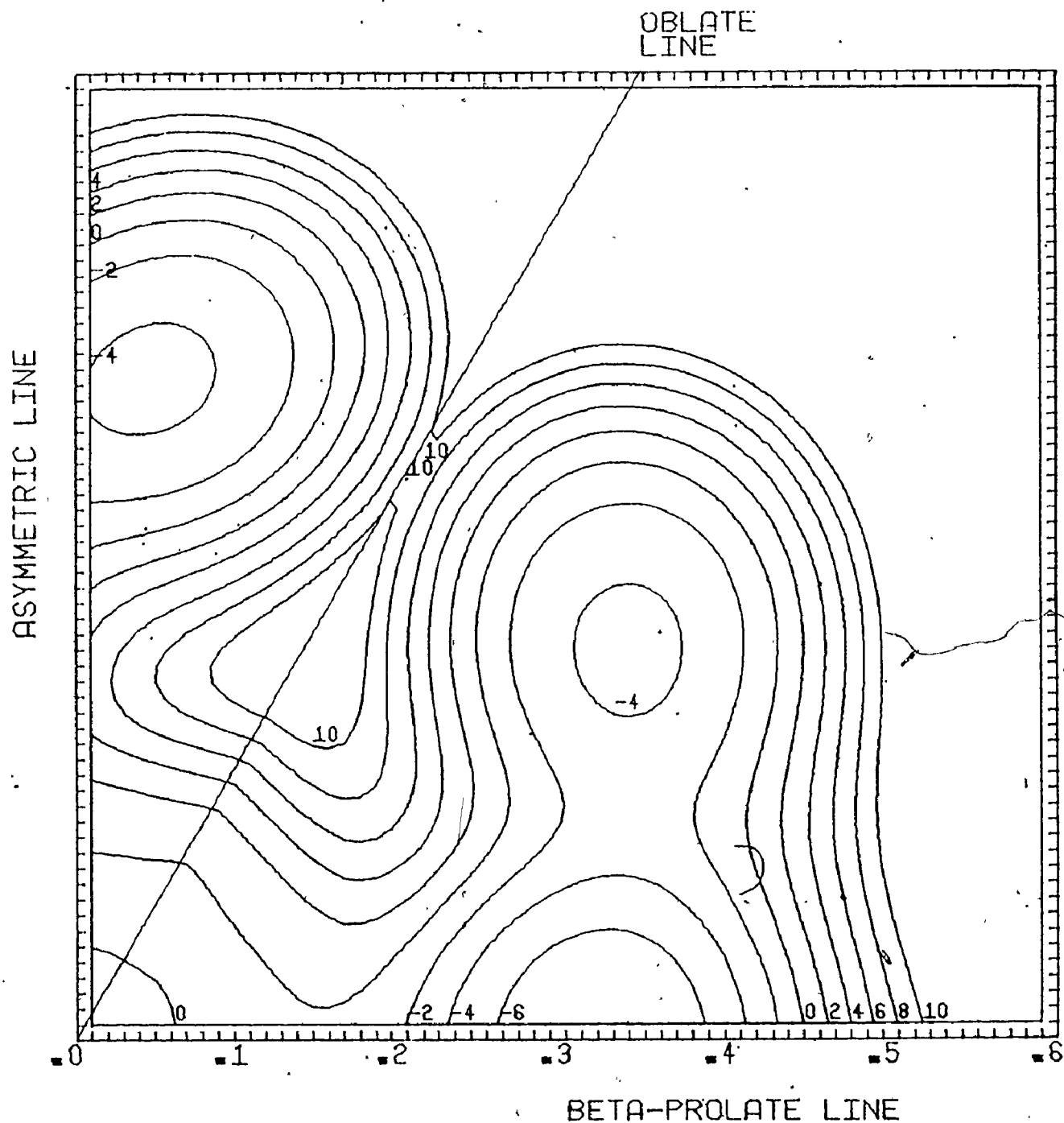
## V. Er<sup>164</sup>

### 1. Energy Levels

Er<sup>164</sup> is investigated in this work because there is a large amount of experimental data available on this nucleus. The "Yrast band" is known as high as  $J = 18$  (LKD 73). (Backbending occurs at  $J_c = 14$ .) Also the energies of the lowest few members of both the  $\gamma$  and  $\beta$ -bands have been measured (Sak 70).

The two minima potential surface illustrated in Figure 4.7 was used in the collective Hamiltonian. One minimum lies on the prolate axis and the second minimum lies in the region of maximum asymmetry. The calculated energies of certain members of the ground,  $\gamma$  and  $\beta$  bands are compared with experiment in

Figure 4.7



Collective potential energy for  $\text{Er}^{164}$ . Contour map of the potential energy as a function of  $\beta$  and  $\gamma$ .

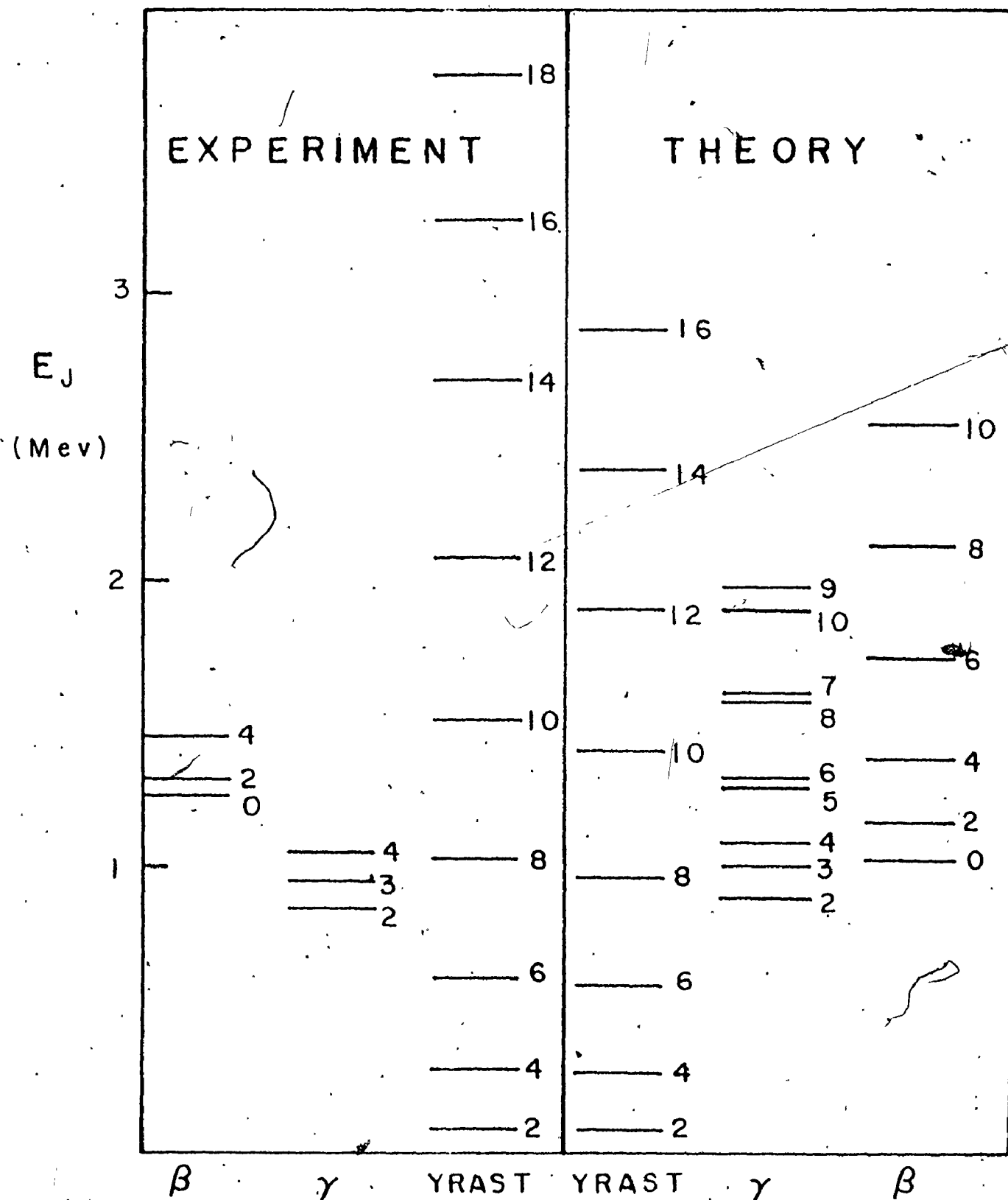
Figure 4.8. On the whole, the agreement is reasonably good. The  $\gamma$  band head energy is well reproduced. However the even spin members of the  $\gamma$  band are displaced slightly downward relative to the odd spin members. This is due to repulsion between members of the  $\gamma$  and  $\beta$  bands having the same angular momentum. The calculated excitation energies of the  $\beta$  band members are lower than the experimental energies.

In Figure 4.9, the energies of the three bands are plotted as a function of  $J(J+1)$ . On this kind of a plot, a rigid rotor yields a straight line. It can be seen that the  $\gamma$  band crosses the ground state band between  $J = 12$  and  $J = 14$ . As was explained in Section III, the crossing is due to the fact that the asymmetric shape becomes energetically more favorable than the prolate shape at sufficiently high spin. A second reason for the crossing is that in the  $\beta$ - $\gamma$  plane the asymmetric minimum is located at a larger  $\beta$  than the prolate minimum. For example, the  $J = 2$  state of the ground state band has an expectation value  $\sqrt{\langle \beta^2 \rangle} = 0.339$ . The  $J = 2$  state of the  $\gamma$  band has  $\sqrt{\langle \beta^2 \rangle} = 0.388$ . The staggering of the even and odd spin members of the  $\gamma$  band is greatly enhanced above the backbending point. In fact for  $J \geq 7$  and  $J$  odd,  $E_J > E_{J+1}$  in the  $\gamma$  band. Hence if an even  $J$  state in the  $\gamma$  band above the backbending point is populated this state will decay via a  $\Delta J = 2$  cascade resulting in the emission of "stretched" E2 photons since a transition to a lower odd state would be of multipolarity E4. Furthermore, if a high odd state is populated, it will preferentially decay to an even state with  $\Delta J = \pm 1$ , by an E2 transition.

Energy levels of  $\text{Er}^{164}$ . The energy levels obtained by solving the Bohr Hamiltonian with the collective potential shown in Figure 4.7 are given and compared to experiment. Only states belonging to the "Yrast band", the  $\beta$  band or the  $\gamma$  band are shown.



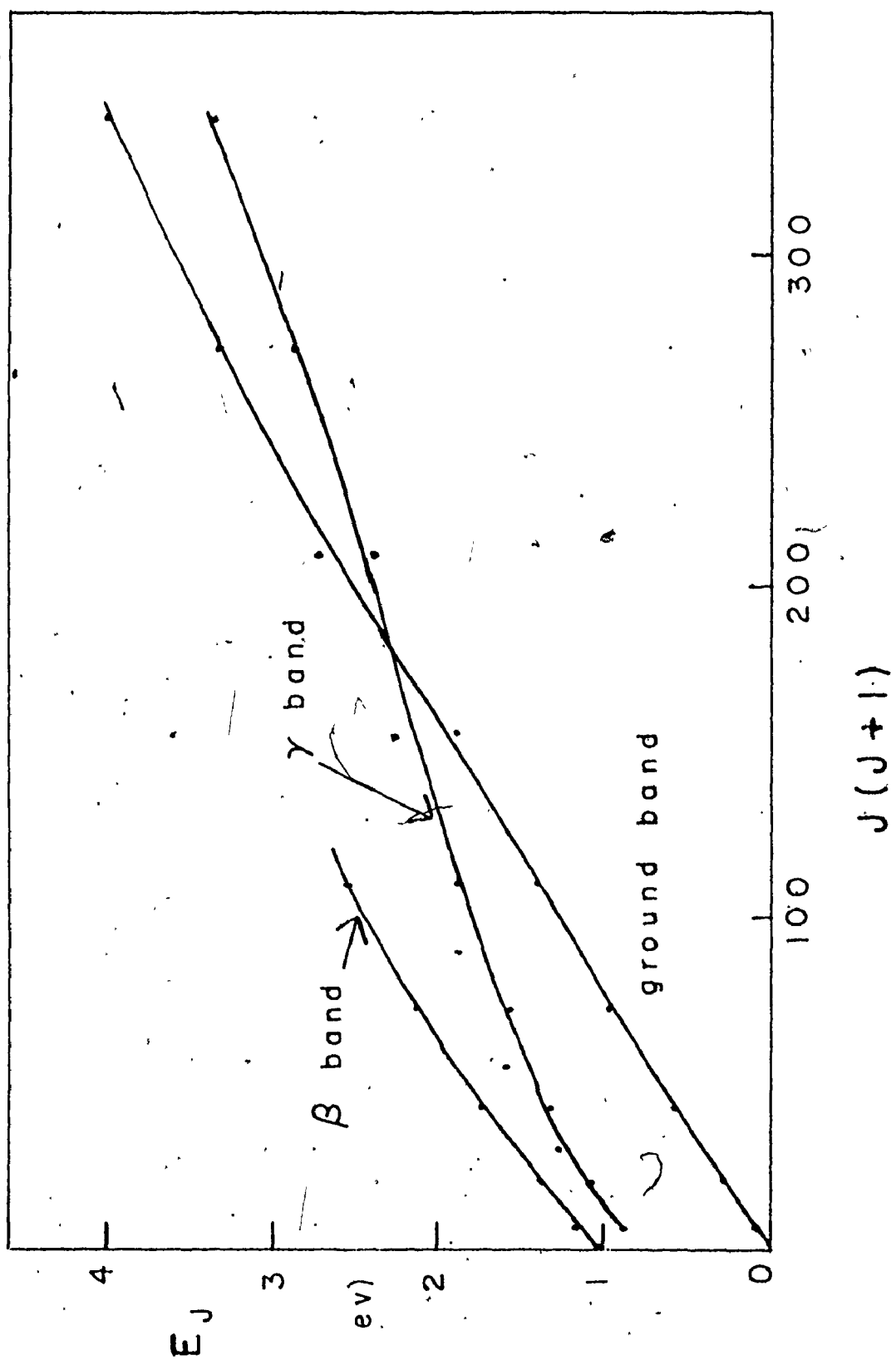
Figure 4.8



Band crossing in  $\text{Er}^{164}$ . The same calculated energies shown in Figure 4.8 are plotted as a function of  $J(J+1)$ .

On this kind of plot, an axially symmetric rigid rotor appears as a straight line. It can be seen that the  $\gamma$  band and the ground band cross.

Figure 4.9



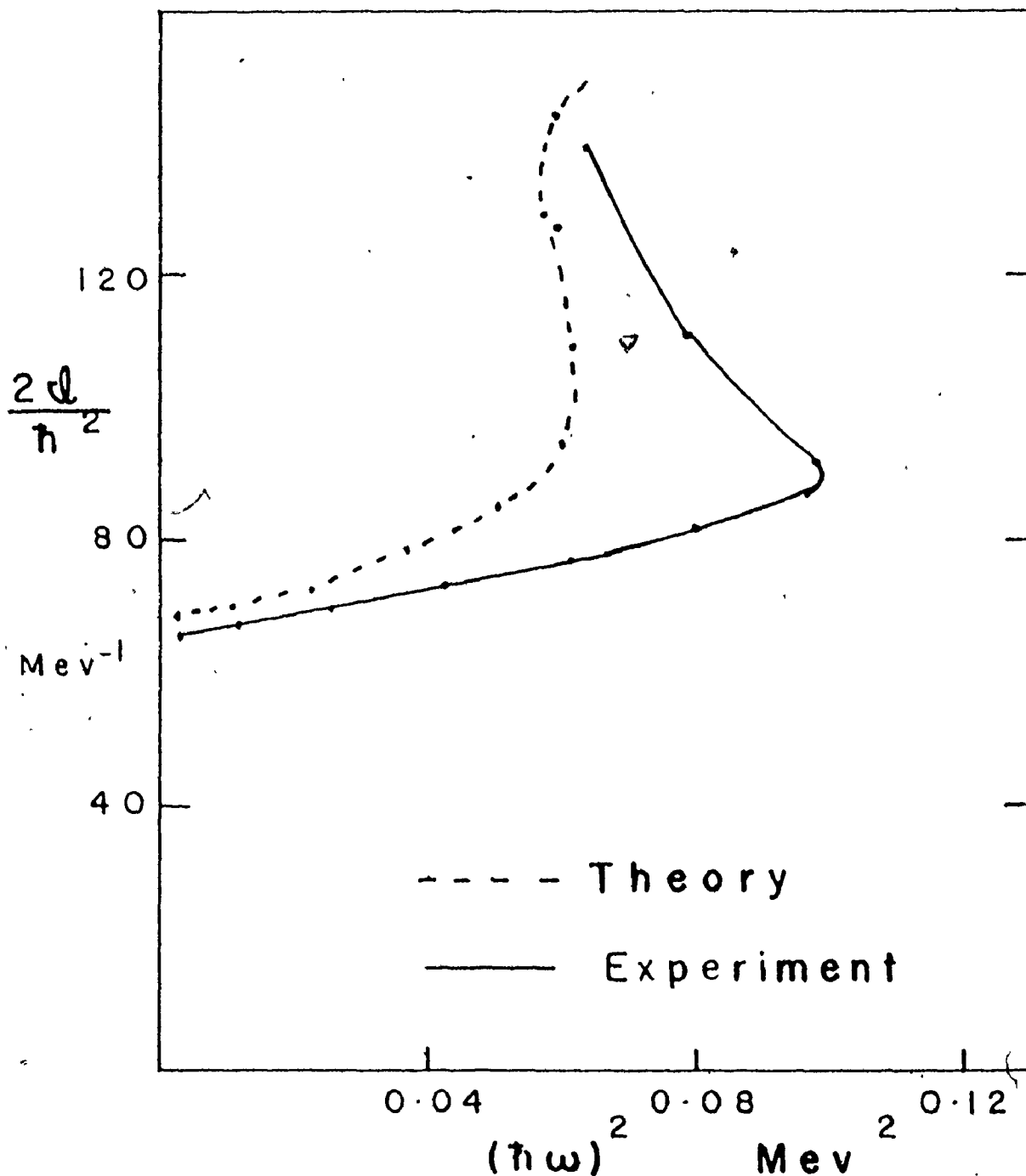
The energies of the Yrast states are shown on an  $\mathcal{J}-\omega^2$  plot in Figure 4.10. The backbending is predicted to occur at the correct angular momentum,  $J = 14$ . However the theoretical backbending is not as pronounced as the experimental backbending. In all the results for  $\text{Er}^{164}$ , the wavefunction has been limited to having K-components no higher than  $K_{\text{max}} = 10$ . (See Section II.) To check the accuracy of this approximation, some of the calculations were repeated but with  $K_{\text{max}} = 8$ . In each case the results differ by no more than the width of an ink line on the plot. The only exception to this is the case  $J = 16$ . The point corresponding to  $J = 16$ ,  $K_{\text{max}} = 8$  is added to the graph in Figure 4.10.

## 2. Wavefunctions and Transition Rates

In our model, backbending results from a sudden change of the shape of the nucleus in the "Yrast band". This can be seen by comparing, for Yrast states above and below the backbending point, the distribution of probability of the nucleus having the shape given by  $(\beta, \gamma)$ . The probability distribution is given for Yrast states  $J = 14$  and  $J = 16$  in Figures 4.11 and 4.12.

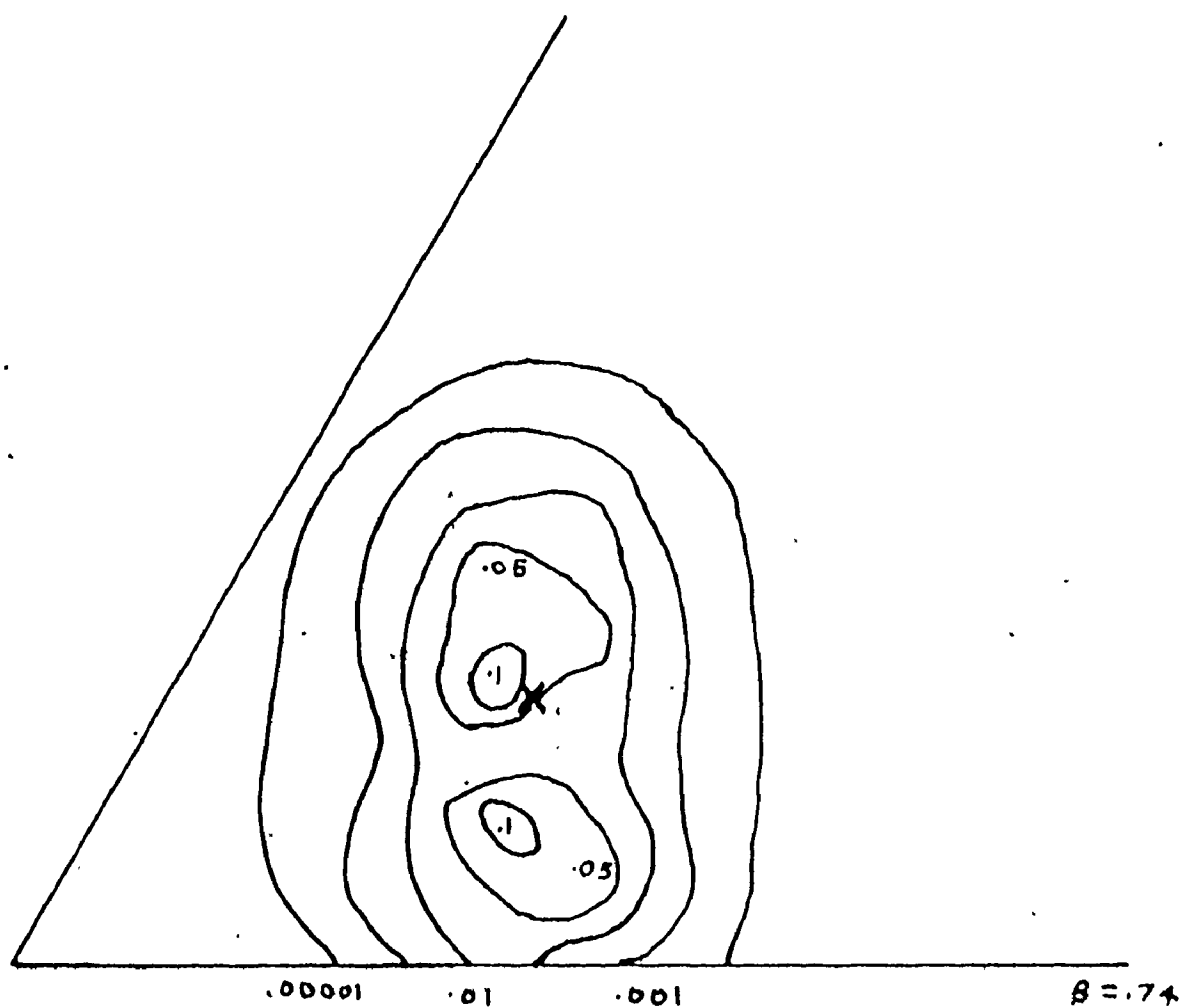
The  $B(E2)$ 's in the Yrast band are shown in Figure 4.13. For comparison, the corresponding  $B(E2)$ 's for a rigid rotor are given. It can be seen that the calculated  $B(E2)$  does increase faster than the  $B(E2)$  of a rigid rotor, especially above  $J_c = 14$ . However for all  $J$ , the  $B(E2)$ 's agree to within a factor of 2.

Figure 4.10



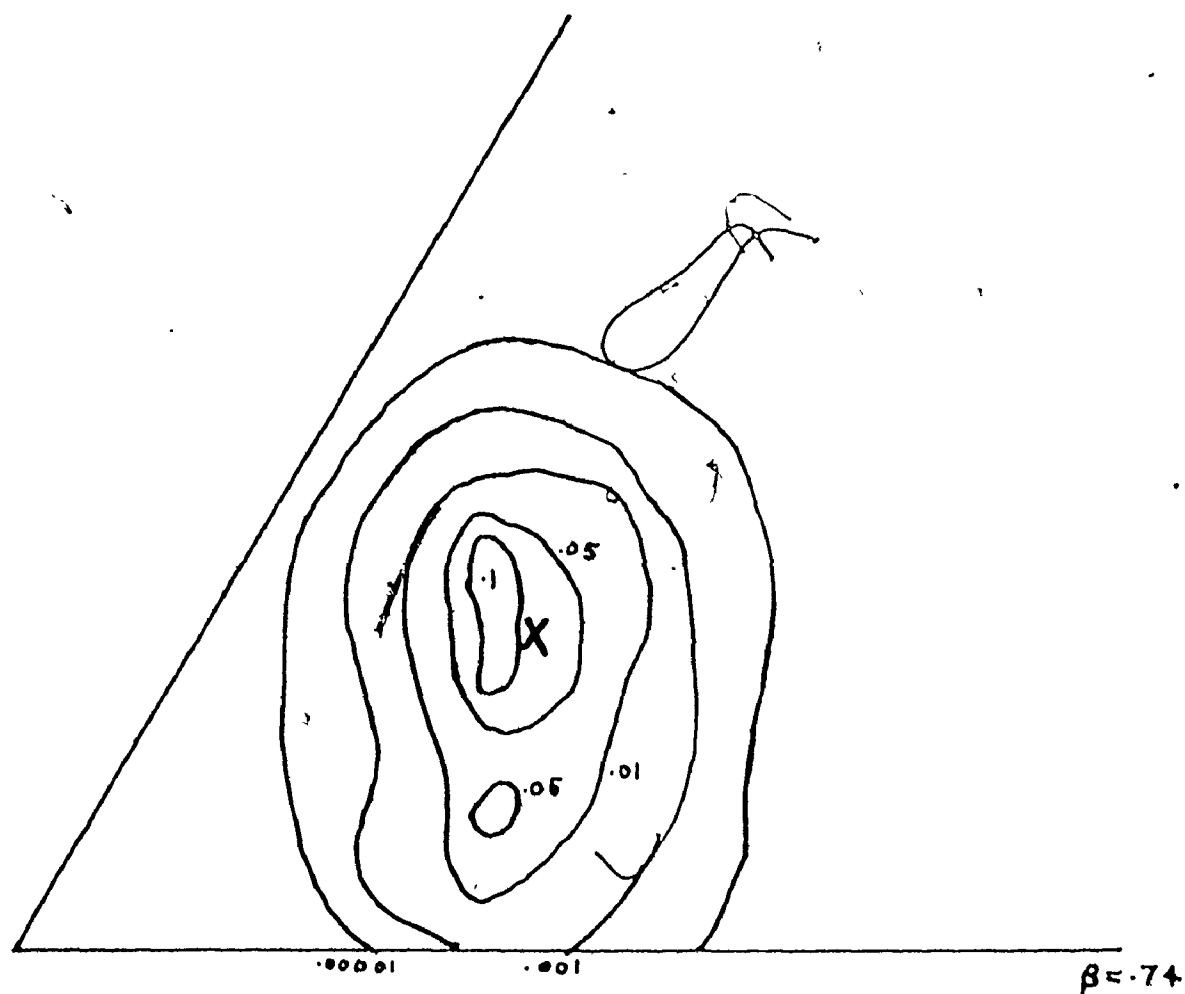
$\mathcal{J}-\omega^2$  plot for  $\text{Er}^{164}$ . The same energies as in Figure 4.8 are plotted on an  $\mathcal{J}-\omega^2$  plot. The isolated point corresponds to the calculation in which the wavefunction is limited to  $K \leq K_{\text{max}} = 8$ . For the rest of the calculated points,  $K_{\text{max}} = 10$ .

Figure 4.11



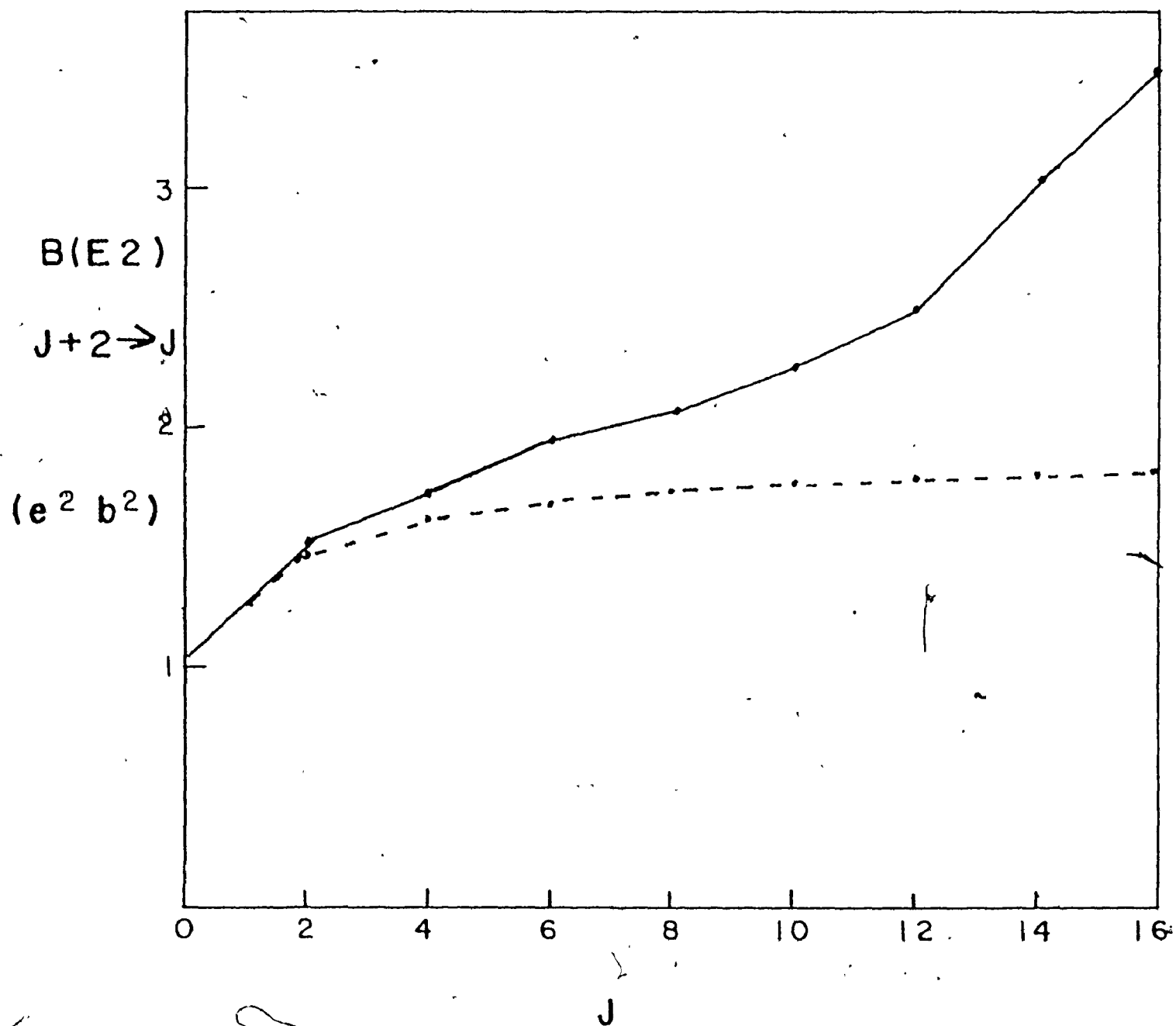
Shape probability for  $J = 14$  state of  $\text{Er}^{164}$ . Contour plot of the square of the modulus of the wavefunction times the integration density as a function of  $\beta$  and  $\gamma$ . An integration has been performed over the three Euler angles. The X marks the expectation value of  $(\beta, \gamma)$ .

Figure 4.12



Shape probability for  $J = 16$  state of  $\text{Er}^{164}$ . See caption to Figure 4.11.

Figure 4.13



$B(E2)$ 's for  $Er^{164}$ . The calculated  $B(E2)$ 's are given by the solid line. The dashed line gives the  $B(E2)$ 's for a rigid rotor.



## VI. Er<sup>162</sup>

Er<sup>162</sup> is the first nucleus for which backbending behaviour was observed. Energies are known experimentally as high as  $J = 20$  (SHJ+ 73). The  $\gamma$  bandhead is also known (Sak 70). A contour map of the potential surface used in this calculation is shown in Figure 4.14. Again a two minima potential is used: one minimum on the prolate axis and a second minimum in the axially asymmetric region. The calculated and experimental energies of the Yrast states and the lowest few members of the  $\gamma$  band are given in Figure 4.15. In the calculations for Er<sup>162</sup>,  $K_{\max} = 8$ . Finally an  $J-\omega^2$  plot for Er<sup>162</sup> is given in Figure 4.16.

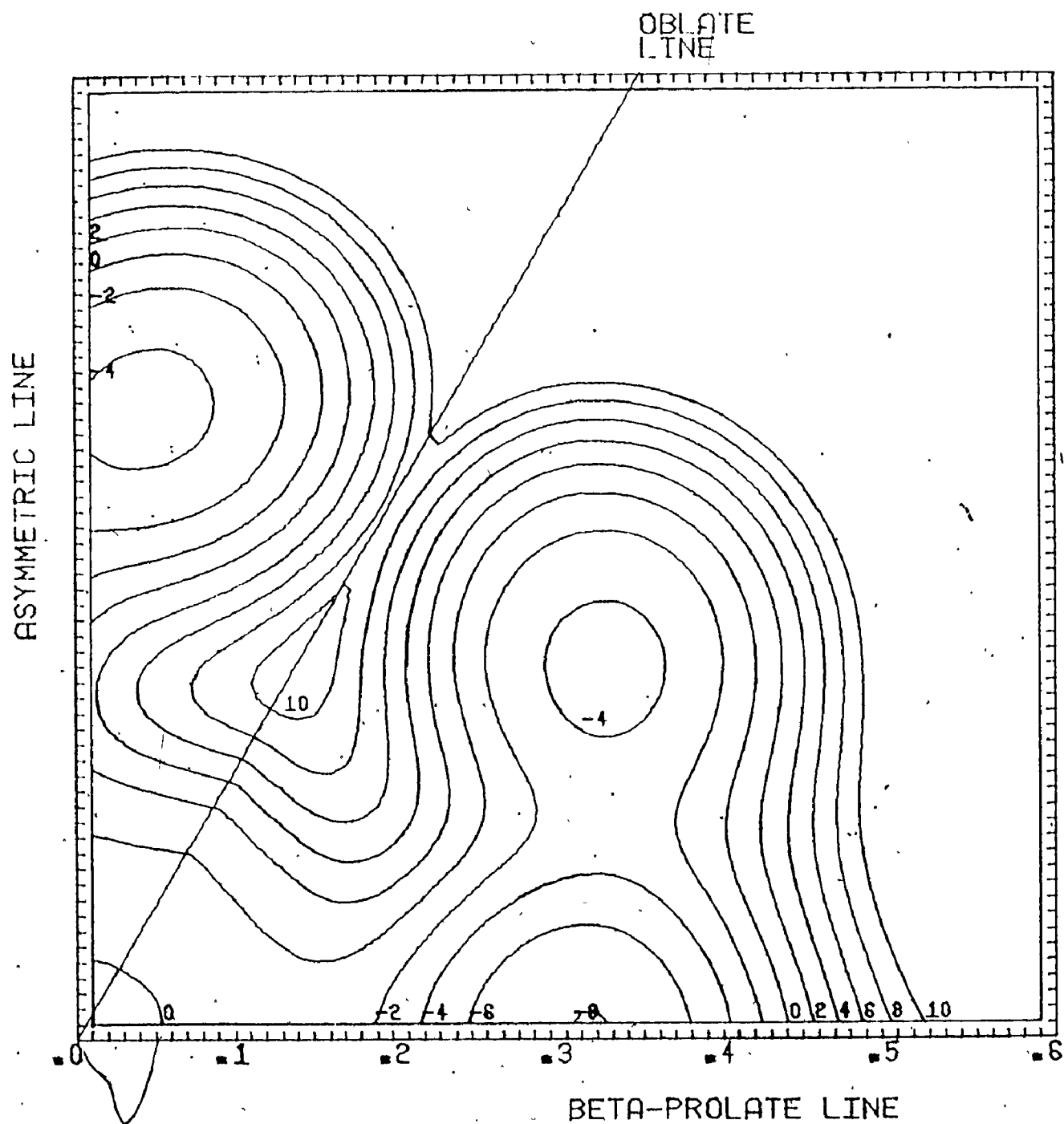
## VII. Os<sup>182</sup>

### 1. Energy Levels

In the Os region, nuclei are less deformed and more transitional in nature. This is indicated by low-lying  $\gamma$  bands (GG 71). For this reason, a two minima potential for which the second minimum is on the oblate axis has been employed. A contour map of this potential is given in Figure 4.17. In order for backbending to occur, it is necessary that the oblate minimum be located at a considerably larger  $\beta$  than the prolate minimum. This has important implications for the transition rates (as will be shown later).

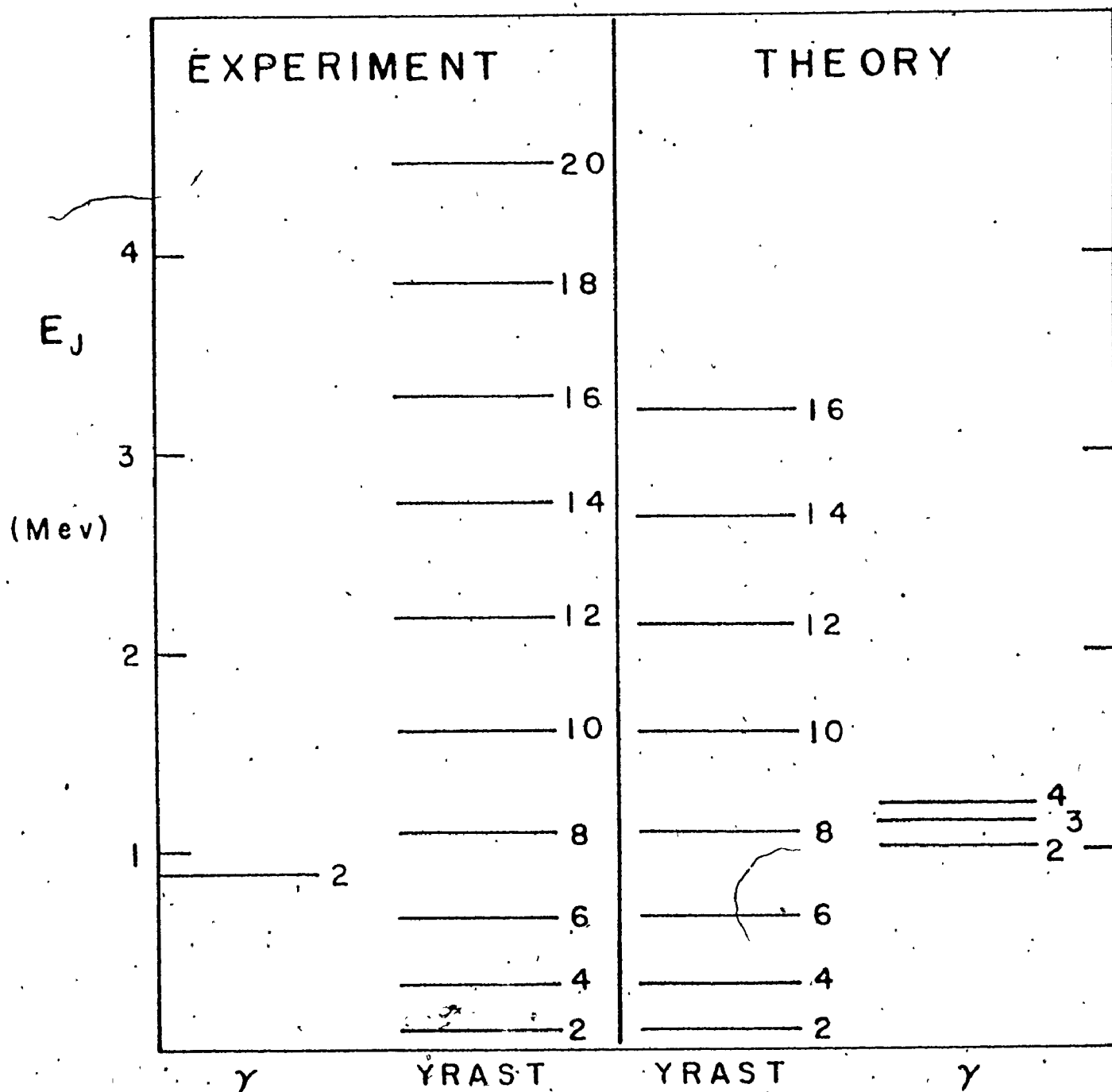
Calculated and experimental levels are given in Figure 4.18. For angular momentum  $J \geq 12$ , the band based on the oblate minimum lies lower. The Yrast band agrees reasonably well with

Figure 4.14



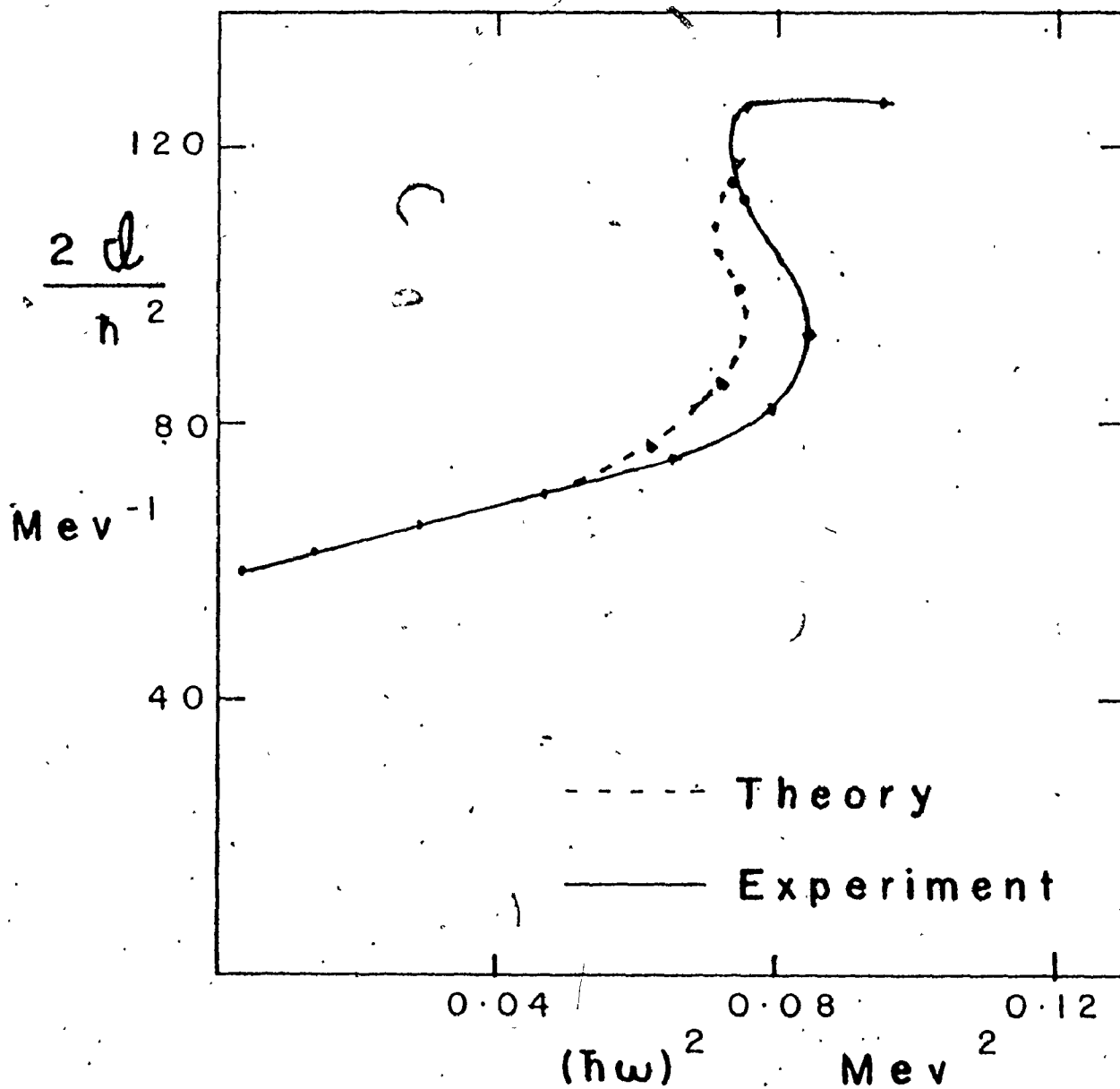
Collective potential energy for  $\text{Er}^{162}$ . Contour map of the potential energy as a function of  $\beta$  and  $\gamma$ .

Figure 4.15



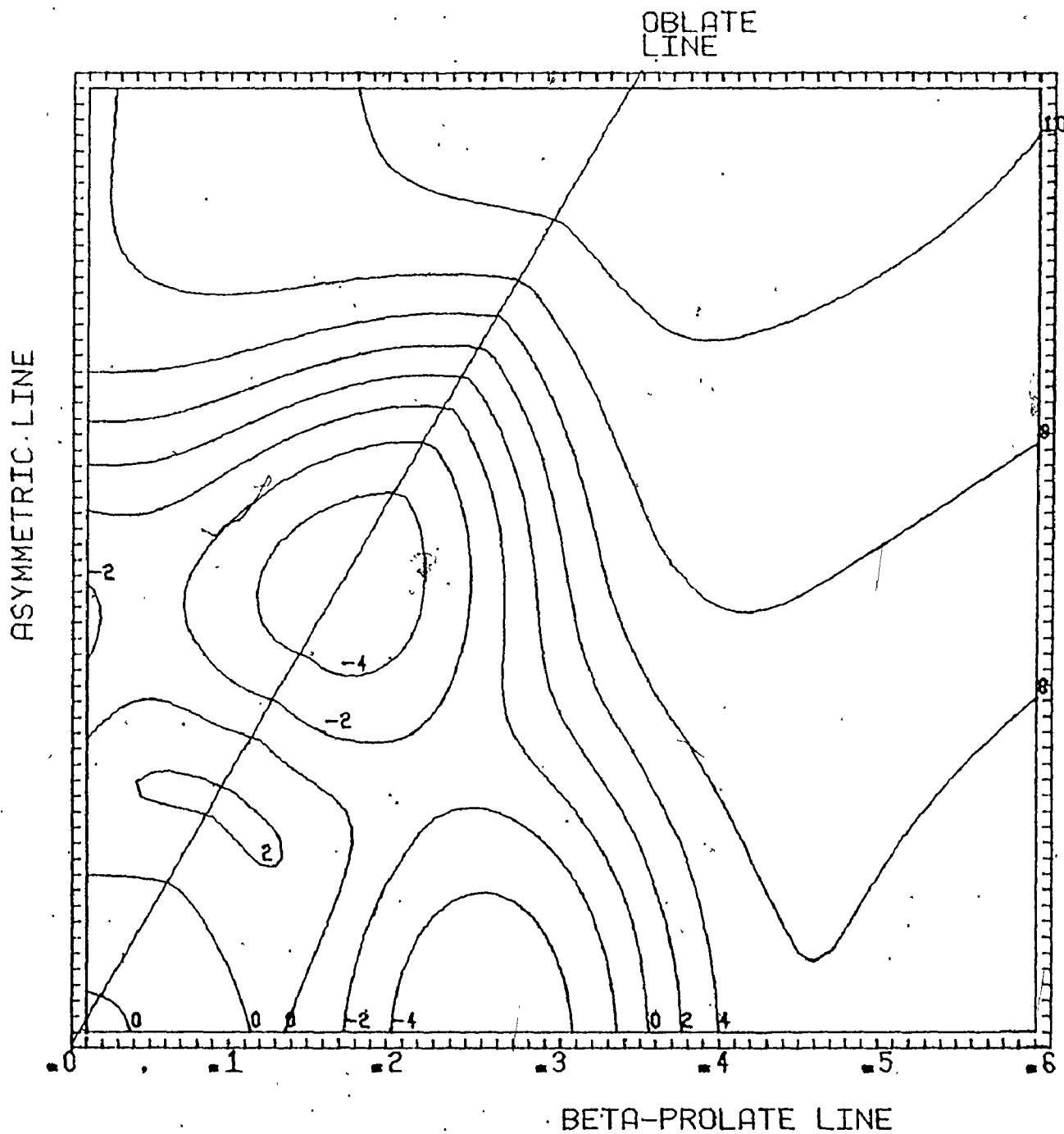
Energy levels of  $\text{Er}^{162}$ . See caption to Figure 4.8.

Figure 4.16



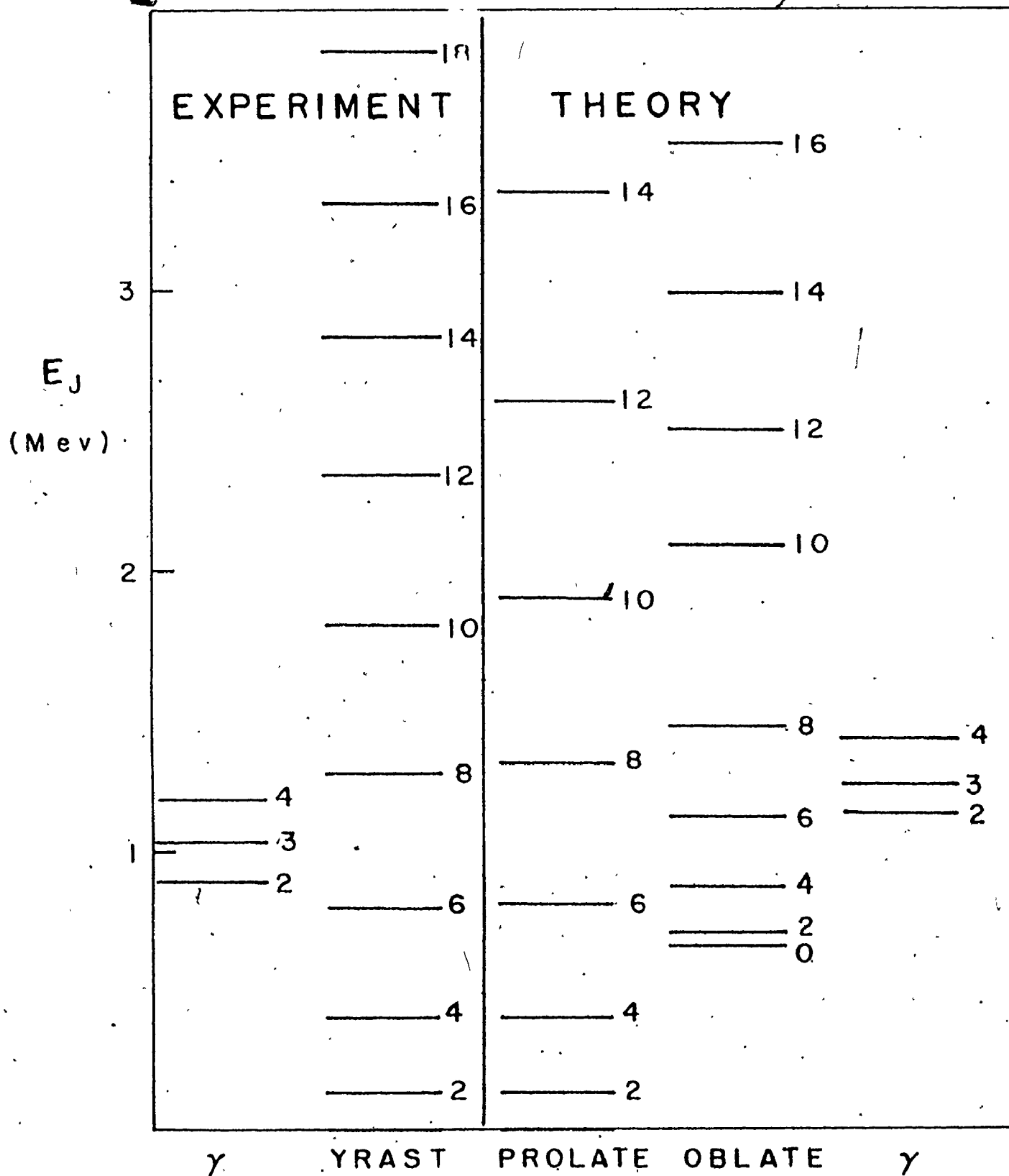
$J-\omega^2$  plot for  $\text{Er}^{162}$ . The same energies as Figure 4.15 are plotted on an  $J-\omega^2$  plot.

Figure 4.17



Collective potential energy for  $\text{Os}^{182}$ . Contour map of the potential energy as a function of  $\beta$  and  $\gamma$ .

Figure 4.18



Energy levels of  $Os^{182}$ . See caption to Figure 4.8.

data. However the  $\gamma$  band is predicted to lie at too high an energy.

The band crossing is also illustrated in Figure 4.19. The results are also shown on an  $\sqrt{J-\omega^2}$  plot in Figure 4-20. Because the wavefunction may be concentrated in the oblate region, it was found that the number of K components to the wavefunction could not be limited. Hence in all cases for Os<sup>182</sup>,  $K_{\max} = J$ .

## 2. Transition Rates

The  $B(E2)$ 's between even Yrast states are calculated and plotted in Figure 4.21. The remarkable feature of the graph is the sharp drop in the  $B(E2; 12 \rightarrow 10)$  transition. This is due to the fact that the  $J = 10$  state is primarily prolate whereas the  $J = 12$  state is primarily oblate. Although experimental measurements of lifetimes in high spin states have large uncertainties associated with them, there does not seem to be any systematic evidence for a dramatic drop in the  $B(E2)$ 's at the backbending point. This is evidence against a prolate-oblate minima potential. If a slightly different potential with a lower barrier between prolate and oblate minima were to be used, the drop in  $B(E2)$  would be less pronounced. An examination of the spectra in Figure 4.18 shows that lowering the oblate-prolate potential barrier in the  $\gamma \neq 0$  region would improve the results. Thus the Yrast levels which are calculated to be too high for  $J \geq 8$  would be pushed down by more mixing. Furthermore, the  $\gamma$  band-

Band crossing in  $\text{Os}^{182}$ . The same calculated energies as in Figure 4.18 are plotted as a function of  $J(J+1)$ . The band based on the oblate minimum crosses the band based on the prolate minimum.



Figure 4.19

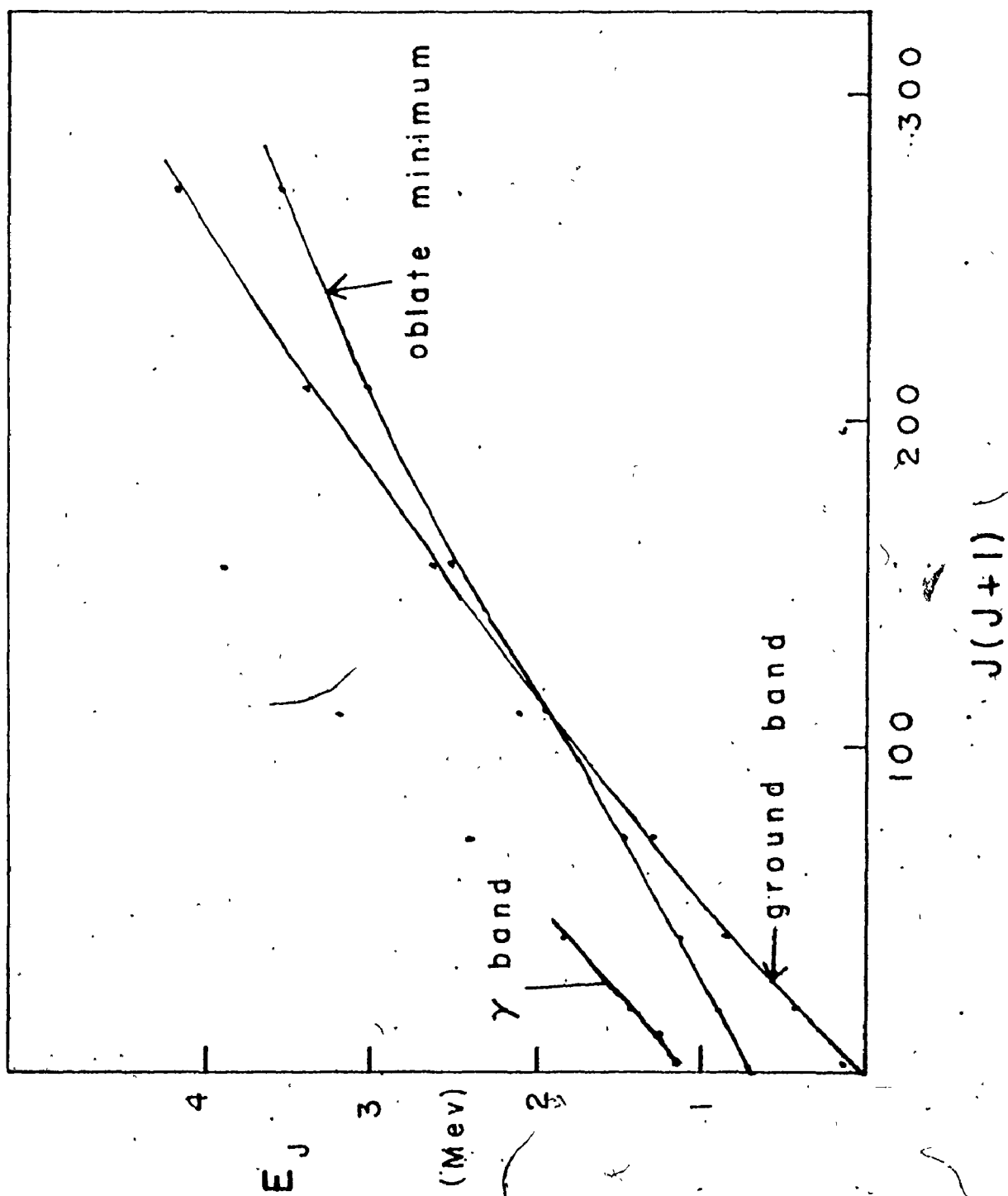
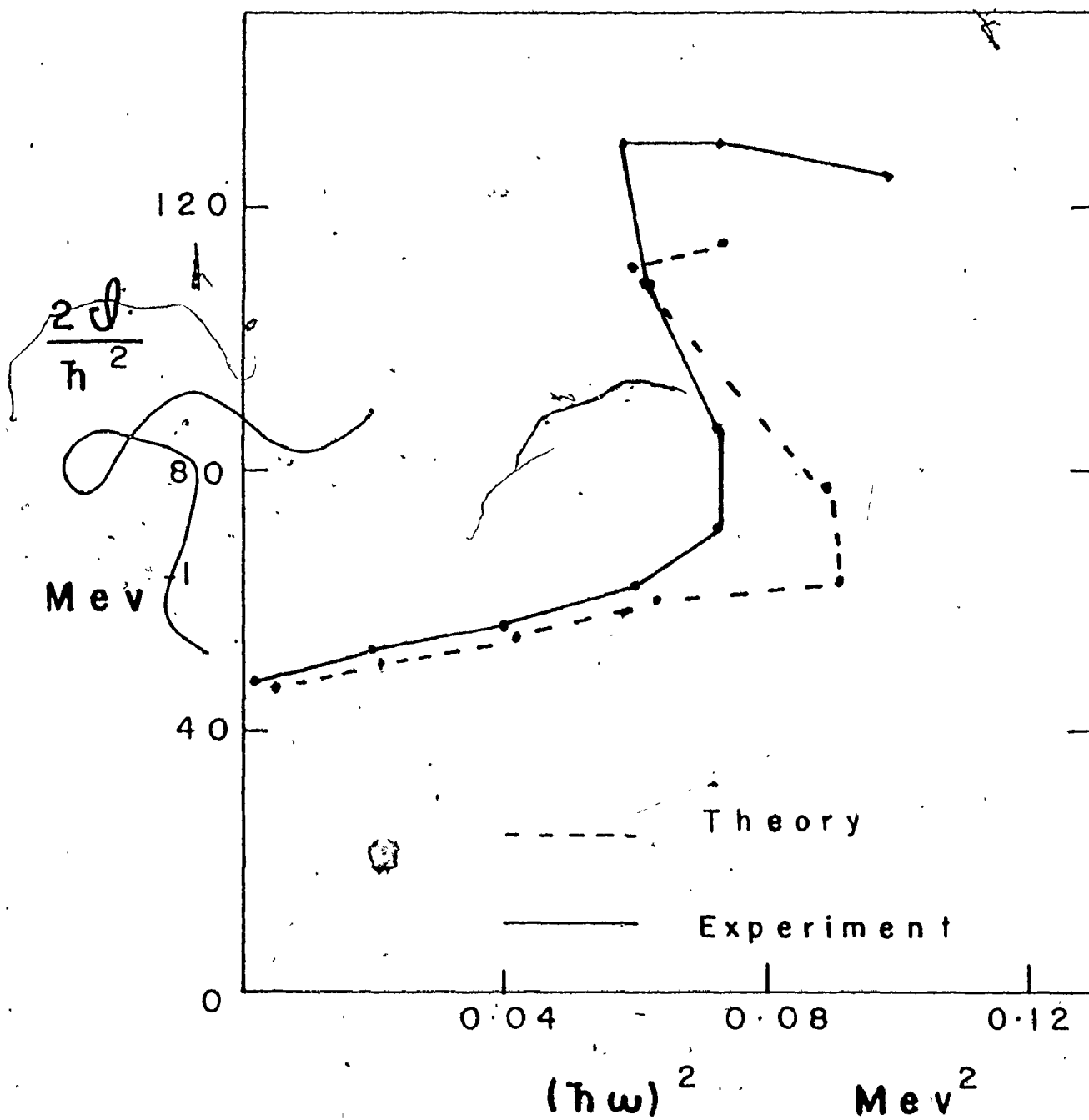
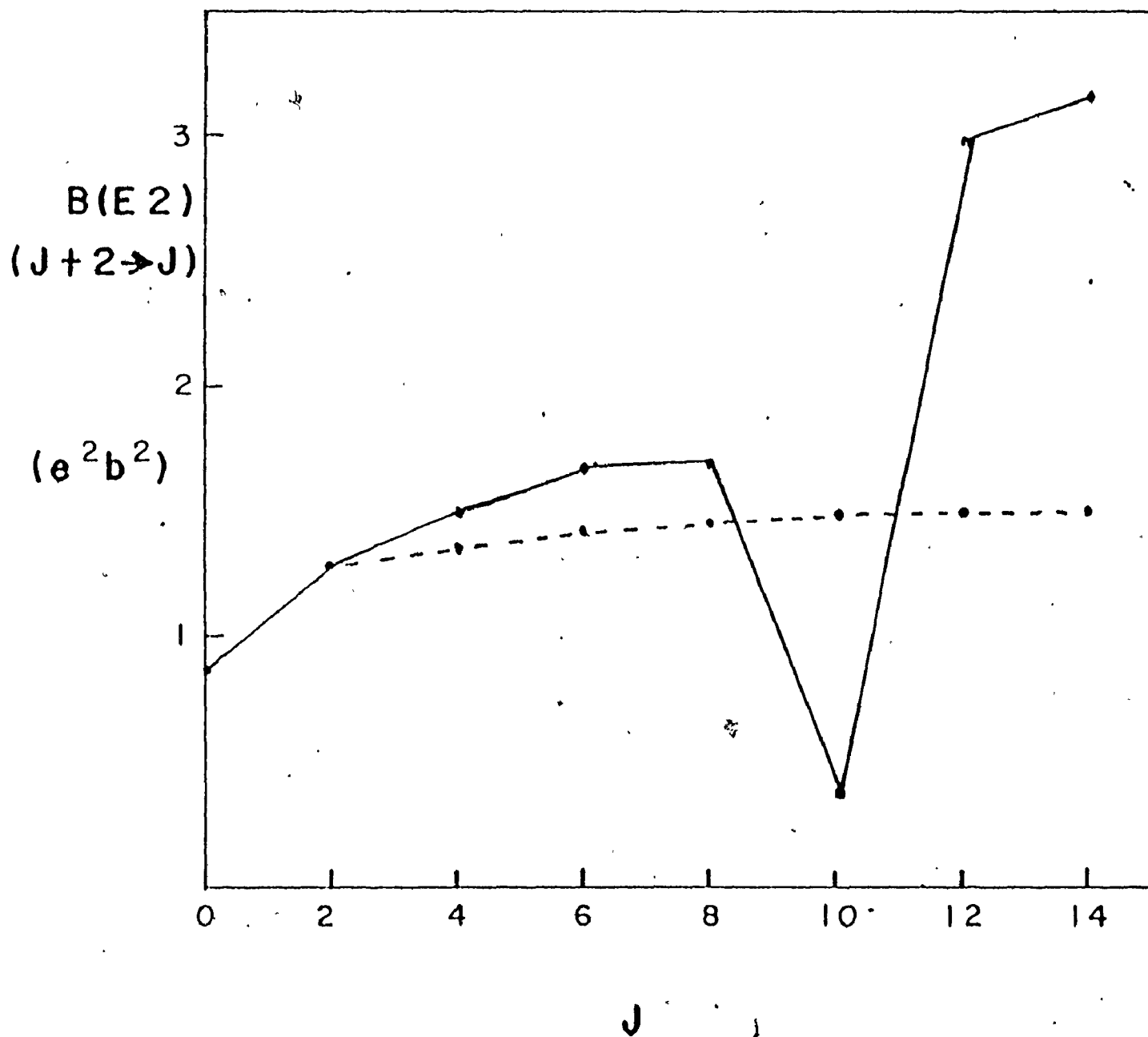


Figure 4.20



$J-\omega^2$  plot for  $^{182}\text{Os}$ . The same energies as in Figure 4.18 are plotted on an  $J-\omega^2$  plot.

Figure 4.21



$B(E2)$ 's for  $Os^{182}$ . See caption to Figure 4.13.

head energy which is calculated to be too high would also be lowered if the  $\gamma$  barrier height were lowered.

### VIII. Comparison of Variable Moment of Inertia Models with Bohr's Collective Model

#### 1. Mathematical Statement of VMI Model

The conventional statement of the VMIS model has been given in equations (2.9). However certain conceptual difficulties arise from this statement of the model when the Thieberger prescription is used. (The Thieberger prescription is a method of determining the VMIS potential  $V(J)$ . It will be described later in this section.) Hence it is necessary to give a more mathematical statement of the VMIS model.

First we define a function  $f$  mapping ordered pairs into the real numbers:

$$f: (J^{(S)}, J) \rightarrow f(J^{(S)}, J) = \frac{J(J+1)}{2J^{(S)}} + V(J^{(S)}) \quad (4.14)$$

The goal is to define the energy as a function of angular momentum. Hence we define

$$E: J \rightarrow E(J) = \frac{J(J+1)}{2J_J^{(S)}} + V(J_J^{(S)}) \quad (4.15)$$

where  $J_J^{(S)}$  is the root of the equation

$$h_J(J^{(S)}) = 0 \quad (4.16)$$

where  $h_J(J^{(S)})$  is defined by

$$h_J(J^{(S)}) \equiv \left. \frac{\partial f}{\partial J^{(S)}} \right|_J (J^{(S)}, J). \quad (4.17)$$

Equations (4.16) and (4.17) define a function

$$\mathcal{J} : J \rightarrow \mathcal{J}_J^{(S)} = \mathcal{J}(J) . \quad (4.18)$$

Define the function  $g$  to be the inverse function of the function  $\mathcal{J}$ :

$$g = \mathcal{J}^{-1} . \quad (4.19)$$

We also define a vector valued function  $\vec{u}$  mapping the real numbers into ordered pairs. That is, we define

$$\vec{u} : J \rightarrow (\mathcal{J}_J^{(S)}, J) = (\mathcal{J}(J), J) = \vec{u}(J) . \quad (4.20)$$

Finally we can properly define the energy as a function of angular momentum as the composition of  $f$  with  $\vec{u}$  as follows:

$$E(J) = f \circ \vec{u}(J) . \quad (4.21)$$

This equation corresponds to equation (2.9-i). Equation (4.16) corresponds to the equilibrium condition given in equation (2.9-ii).

## 2. Thieberger (Thi 72) Prescription for Obtaining $V(J)$

From the expression for the VMIS energy, it is possible to derive an auxiliary quantity  $\omega$ , which can be interpreted as the angular frequency. It should be noted that so far,  $J$  is simply a real number; it has not yet been restricted to integer values. We define a function

$$\tilde{E} : x \rightarrow \tilde{E}(x) \text{ so that } \tilde{E}(\sqrt{J(J+1)}) = E(J) . \quad (4.22)$$

Then we define a function  $\omega: J \rightarrow \omega(J)$  so that

$$\omega(J) = \left. \frac{dE}{dx} \right|_x = \sqrt{J(J+1)} . \quad (4.23)$$

Combining equations (4.22) and (4.23),

$$\omega(J) = \frac{dE(J)}{dJ} \frac{dJ}{d\sqrt{J(J+1)}} \quad (4.24)$$

from equations (4.20) and (4.21) we obtain

$$\frac{dE(J)}{dJ} = \left[ \left. \frac{\partial f}{\partial J^{(S)}} \right|_{J} (J_J^{(S)}, J) \right] \times \frac{dJ_J^{(S)}}{dJ} + \left. \frac{\partial f}{\partial J} \right|_{J_J^{(S)}} (J_J^{(S)}, J) . \quad (4.25)$$

However the quantity in square brackets is zero from equations (4.16) and (4.17). Hence

$$\begin{aligned} \omega(J) &= \left. \frac{\partial f}{\partial J} \right|_{J_J^{(S)}} (J_J^{(S)}, J) \frac{dJ}{d\sqrt{J(J+1)}} \\ &= \frac{1}{2J_J^{(S)}} \frac{d[J(J+1)]}{dJ} \times \frac{dJ}{d\sqrt{J(J+1)}} \\ &= \frac{\sqrt{J(J+1)}}{J_J^{(S)}} . \end{aligned} \quad (4.26)$$

Equations (4.16) and (4.17) can be written

$$-\frac{J(J+1)}{2(J_J^{(S)})^2} + \left. \frac{dV(J_J^{(S)})}{dJ_J^{(S)}} \right|_{J_J^{(S)}} = 0 . \quad (4.27)$$

Combining this with equation (4.26) yields the interesting relation

$$\left. \frac{dV(J_J^{(S)})}{dJ_J^{(S)}} \right|_{J_J^{(S)}} = \frac{1}{2} [\omega(J)]^2 . \quad (4.28)$$

Substituting equation (4.19) we obtain

$$\frac{dv(J^{(S)'})}{dJ^{(S)'}} = \frac{1}{2}[\omega(g(J^{(S)'}))]^2 \quad (4.29)$$

This equation can be integrated to yield the VMIS potential energy

$$v(J^{(S)}) - v(J_0^{(S)}) = \int_{J_0^{(S)}}^{J^{(S)}} \frac{1}{2}[\omega(g(J^{(S)'}))]^2 dJ^{(S)'} \quad (4.30)$$

In chapter 2, section II-2, the quantities  $J$  and  $\omega$  appearing in the  $J-\omega^2$  plot were defined. For purposes of reference we repeat equation (2.10-i):

$$h\omega = \frac{dE}{d\sqrt{J(J+1)}} \quad (2.10-i)$$

In this equation  $E$  is the experimental energy. Equation (2.10-i) is equivalent to equation (4.23) (with  $K$  set equal to 1). As a result, the following procedure due to Thieberger (Thi 72) can be followed.  $\omega$  as a function of angular momentum can be determined from the experimental energy levels. This function is then inserted into equation (4.30) to yield the VMIS potential energy. In principle this process is exact. If the VMIS potential is inserted into the VMIS equations (equations (2.9), or, equivalently, equations (4.20) and (4.16)) the predicted energies should agree exactly with experiment. It should also be noted that equation (4.26) agrees with the definition for  $J$  given in equation (2.11).

However there is a difficulty in that the experimental energy levels are known only for discrete angular momentum  $J$ . This problem was mentioned in chapter 2, section II-2. It is necessary to perform some interpolation before the derivative in equation (2.10-i) can be evaluated.

In the original statement of the VMIS model (MSB 69) the simple quadratic potential  $V(J^{(S)}) = \frac{1}{2} C (J^{(S)} - J_0^{(S)})^2$  was used. Using equation (4.29) we obtain

$$C (J^{(S)} - J_0^{(S)}) = \frac{1}{2} [\omega(g(J^{(S)}))]^2 \quad (4.31)$$

or written less carefully

$$J^{(S)} = J_0^{(S)} + \frac{1}{2C} \omega^2. \quad (4.32)$$

Hence the simple quadratic VMIS model predicts a straight line on an  $J - \omega^2$  plot. If the energy levels of a nucleus can be accurately described by the quadratic VMIS model, then when the experimentally determined moment of inertia (see equation (2.11)) is plotted as a function of the square of the experimentally determined angular velocity (see equation (2.10-i)) a straight line should result. This assumes the derivative in equation (2.10-i) is evaluated exactly. If the Stockholm interpolation prescription is used (see equations (2.12)-(2.14)), only an approximate straight line is obtained on an  $J - \omega^2$  plot.

### 3. Comparison of VMIS $V(J^{(S)})$ to the Potential Energy in the Collective Model

For each angular momentum  $J$ , the Bohr collective model has been solved yielding  $\psi_J$  and  $E_J$ . It is thus possible to cal-



calculate the expectation value of the potential energy  $\langle \psi_J | \hat{V} | \psi_J \rangle$ .

The zero of the energy scale has been chosen to be the expectation value of the potential energy for the  $J=0$  state. Hence we define the quantities  $V_J$  by

$$V_J = \langle \psi_J | \hat{V} | \psi_J \rangle - \langle \psi_{J=0} | \hat{V} | \psi_{J=0} \rangle. \quad (4.33)$$

Another quantity of interest is the expectation value of the sum of the potential energy and vibrational energy. Hence we define  $U_J$  by

$$U_J = \langle \psi_J | \hat{T}_{\text{vib}} + \hat{V} | \psi_J \rangle - \langle \psi_{J=0} | \hat{T}_{\text{vib}} + \hat{V} | \psi_{J=0} \rangle. \quad (4.34)$$

The quantities  $V_J$  and  $U_J$  are compared with  $V(\sqrt{J(J+1)})^{(S)}$  where  $V(\sqrt{J(J+1)})^{(S)}$  is obtained using the Thieberger prescription. To obtain  $V(\sqrt{J(J+1)})^{(S)}$ , first the Bohr Hamiltonian is solved for each angular momentum to yield  $E_J$ ,  $J = 0, 2, 4, \dots$ . Then  $E_J$  is plotted as a function of  $\sqrt{J(J+1)}$ . Using a spline function (see Appendix D) these discrete points are interpolated yielding a smooth curve. The spline function is differentiated analytically and the derivative evaluated at each point  $\sqrt{J(J+1)}$  where  $J$  is integral. This yields  $\omega_J$  as can be seen from equation (4.24). (This method is different from the conventional procedure in which the derivative  $dE/d\sqrt{J(J+1)}$  is evaluated half-way between the discrete angular momenta.)

Using equation (4.30) the VMIS potential can be written as

$$V(\sqrt{J(J+1)})^{(S)} = \sum_{\text{even } J'=2}^J \Delta V_{J'}, \quad (4.35)$$

where

$$\begin{aligned}\Delta V_J &\equiv V(\mathcal{J}_J^{(S)}) - V(\mathcal{J}_{J-2}^{(S)}) \\ &= \int_{Y_{J-2}}^{Y_J} \frac{1}{2} \omega^2 \frac{d\mathcal{J}^{(S)}}{dy} dy\end{aligned}\quad (4.36)$$

and

$$Y_J \equiv \sqrt{J(J+1)} . \quad (4.37)$$

After some algebra we obtain

$$\Delta V_J = E_J - E_{J-2} - \frac{1}{2} (\omega_J Y_J - \omega_{J-2} Y_{J-2}) . \quad (4.38)$$

Since  $\omega_J$  was calculated previously, we can now calculate  $V(\mathcal{J}_J^{(S)})$  by using equation (4.35). The quantities  $\omega_J$  are also used to calculate the moment of inertia at discrete  $y (= \sqrt{J(J+1)}, J$  integral) by

$$\mathcal{J}_J^{(S)} = \sqrt{J(J+1)} / \omega_J . \quad (4.39)$$

In Chapter II it was explained that the variable moment of inertia  $\mathcal{J}^{(S)}$  described all changes in the intrinsic wavefunction including microscopic degrees of freedom.  $\mathcal{J}^{(S)}$  is not simply proportional to  $\beta^2$ . Hence it is misleading to think of  $V(\mathcal{J}^{(S)})$  as giving information on the potential surface. To obtain some insight into  $V(\mathcal{J}^{(S)})$ , it will be compared with the quantities  $V_J$  and  $U_J$  (equations (4.33) and (4.34)) obtained from the solution of the Bohr Hamiltonian. The collective potential used in the Bohr Hamiltonian corresponds to a qualitative fit to  $E_r^{164}$ . It is plotted in Figure 4.7. The quantities

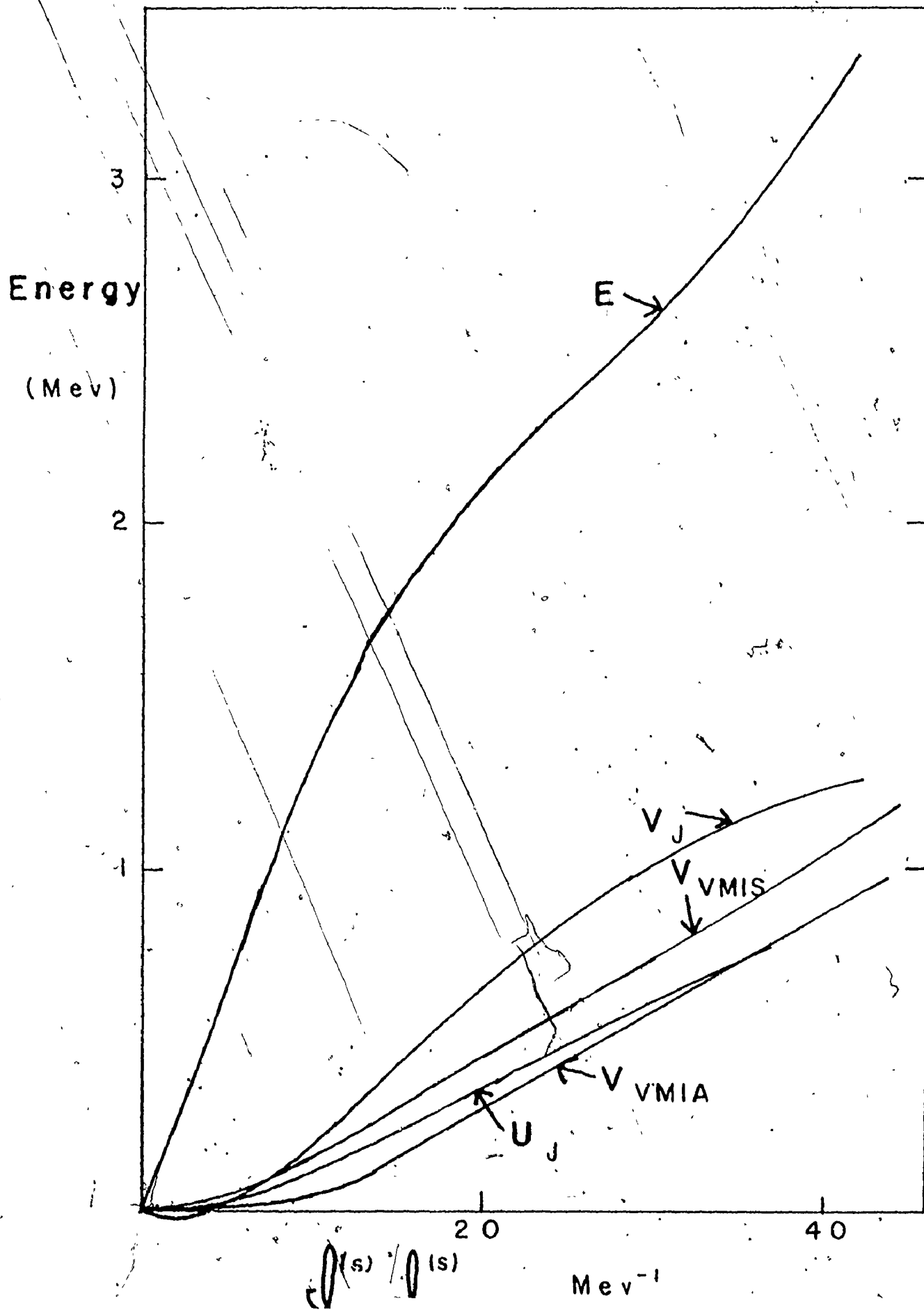
$E_J$ ,  $V_J$ ,  $U_J$  and  $V(J^{(S)})$  are plotted as a function of  $J^{(S)}$  in Figure 4.22. On the graph,  $V(J^{(S)})$  has been labeled  $V_{VMIS}$ . It can be seen that the expectation value of the collective potential,  $V_J$ , is not at all well approximated by  $V_{VMIS}$ . In fact, for small  $J$ ,  $V_J$  is slightly negative. However the expectation value of the sum of the vibrational kinetic energy and the potential energy,  $U_J$ , is reasonably well approximated by  $V_{VMIS}$ , especially at lower spins. Hence it can be concluded that  $V(J^{(S)})$  in the VMIS model represents not only potential energy but also vibrational energy (vibrational energy resembles somewhat zero-point energy).

#### 4. "Potential Energy" in the VMIA Model

In this subsection the  $V(J^{(A)}, \gamma)$  appearing in the VMIA model will be calculated. The Thieberger prescription does not apply in this case. In fact, there is a whole class of potential surfaces  $V(J^{(A)}, \gamma)$  which will predict the same energy levels. An example is a potential which is identical to the  $V(J^{(S)})$  in the  $J^{(S)}$  direction but having a deep minimum in the  $\gamma$  direction at  $\gamma = 0$ . That is,  $V(J^{(S)})$  is essentially a special case of  $V(J^{(A)}, \gamma)$ .

To allow a comparison between  $V(J^{(A)}, \gamma)$  and the expectation of the collective potential, the following restriction is applied. For each angular momentum  $J$ , the equilibrium value of  $\gamma$ ,  $\gamma_J$ , is taken to be the same as the effective value of  $\gamma$  obtained from the solution  $\psi_J$  of the Bohr Hamiltonian.

VMI-type "potential energies".  $V_J$ ,  $U_J$ ,  $V_{VMIS}$ ,  $\varphi^{(S)}$  and  $V_{VMIA}$  are defined by equations (4.33), (4.34), (4.35), (4.39) and (4.46) respectively.



In what follows, mathematical rigor will be sacrificed for brevity. We recall that the VMIA model gives an energy

$$E_J = \frac{R_J(\gamma_J)}{2J_J^{(A)}} + V(J_J^{(A)}, \gamma_J) \quad (4.40)$$

The equilibrium conditions (see equations (2.51), (2.52) are

$$\frac{1}{2J_J^{(A)}} \frac{dR_J(\gamma_J)}{d\gamma_J} + \left. \frac{\partial V}{\partial \gamma_J} \right|_{J_J^{(A)}} = 0 \quad (4.41)$$

and

$$-\frac{R_J(\gamma_J)}{2[J_J^{(A)}]^2} + \left. \frac{\partial V}{\partial J_J^{(A)}} \right|_{\gamma_J} = 0 \quad (4.42)$$

The angular frequency can be obtained from the energy levels in the same manner as before, i.e.

$$\omega_J \equiv \frac{dE_J}{d\sqrt{J(J+1)}} \quad (4.43)$$

Hence

$$\begin{aligned} \omega_J &= \left. \frac{\partial E_J}{\partial J_J^{(A)}} \right|_{J, \gamma_J} \times \frac{dJ_J^{(A)}}{d\sqrt{J(J+1)}} + \left. \frac{\partial E_J}{\partial \gamma_J} \right|_{J, \gamma_J} \times \frac{d\gamma_J}{d\sqrt{J(J+1)}} \\ &\quad + \cancel{\frac{1}{2J_J^{(A)}} \frac{\partial R_J(\gamma_J)}{\partial \sqrt{J(J+1)}} \Big|_{\gamma_J}} \\ &= \frac{1}{2J_J^{(A)}} \frac{\partial R_J(\gamma_J)}{\partial \sqrt{J(J+1)}} \Big|_{\gamma_J} \quad (4.44) \end{aligned}$$

using equations (4.41) and (4.42). Equation (4.43) defines  $\omega_J$  in terms of the energy levels  $E_J$  obtained by solving the Bohr Hamiltonian. Also  $\gamma_J$  is calculated by using wavefunctions obtained by solving the collective Hamiltonian. Hence equation (4.44)

defines  $J_J^{(A)}$ . In all cases, derivatives of functions defined only at discrete points are calculated by first interpolating the function with a spline function.

Parenthetically, it should be noted that the moment of inertia obtained from the data, i.e.  $J_J$ , is not the same as  $J_J^{(A)}$ . The former has been given in equation (2.11) as

$$J_J = \sqrt{J(J+1)} / \omega_J \quad (4.45)$$

Combining this equation with equation (4.44) we obtain

$$J_J = 2J_J^{(A)} \frac{\sqrt{J(J+1)}}{\left. \frac{\partial R_J(\gamma_J)}{\partial \sqrt{J(J+1)}} \right|_{\gamma_J}} \neq J_J^{(A)}$$

unless  $\gamma_J = 0$  for all  $J$ .

The ordered pair  $(J_J^{(A)}, J_J)$  is now known for all  $J$ . These ordered pairs are first plotted in the  $J_J^{(A)} - \gamma$  plane and then connected by straight lines. The VMIA potential  $V(J_J^{(A)}, \gamma)$  is then calculated by numerically integrating equations (4.41) and (4.42) along the straight lines. Since we have defined  $J_J^{(A)}$  and  $\gamma$  as functions of  $J$ , we can define

$$V_{VMIA}(J) = V(J_J^{(A)}, \gamma_J). \quad (4.46)$$

$V_{VMIA}$  has been included on the plot in Figure 4.22.

It is interesting that for the high spin states,  $V_{VMIA}$  is very close to the vibrational plus potential energy,  $U_J$ .

## CHAPTER 5

### EXTENSION OF THE BOHR HAMILTONIAN SOLUTION TO ODD PARTICLE NUCLEI

#### I. Introduction

Bohr (Boh 52) discussed odd particle systems in his original paper. In this model, the extra-core particle(s) move(s) in a deformed potential well formed by the even-even core. Because both collective and single particle degrees of freedom are involved, this is called the unified model.

The unified model contains all the complexities (eg.  $\beta$  and  $\gamma$  vibrations) that the quadrupole collective model possesses. In addition, the wavefunction of the extra particle (or particles) moving in a rotating potential must be considered. As a result the Schroedinger equation resulting from this model becomes extremely difficult to solve. Hence several approximations have to be made.

The first approximation usually made is the adiabatic approximation which states that the single particle motion is much faster than the collective (i.e. co-operative) motion. Often it is further assumed that the potential well is static in the body-fixed frame. This assumption eliminates rotation-vibration coupling.

The third approximation usually made is to choose a deformed potential which is axially symmetric (about one of the



body-fixed axes. This can be considered a Coriolis effect. The resulting wavefunction consists of a mixture of components with different angular momenta along the symmetry axis of the potential. The Coriolis effects can be very important, especially for the high spin states.

Kerman (Ker 56) was the first to perform an actual calculation with this model. He assumed a rigid axially symmetric core wavefunction. This implies that the core cannot have a component of angular momentum along its symmetry axis. With these approximations, the Hamiltonian for the core plus one particle system becomes

$$\hat{H} = \hat{T}_{\text{rot}} + \hat{H}_p \quad (5.1)$$

where

$$\hat{T}_{\text{rot}} = \frac{(\hat{J}_1 - \hat{j}_1)^2}{2J} + \frac{(\hat{J}_2 - \hat{j}_2)^2}{2J} \quad (5.2)$$

and

$$\hat{H}_p = -\frac{\hbar^2}{2\mu} \nabla^2 + V(X, Y, Z). \quad (5.3)$$

The Laplacian and the potential are each expressed in co-ordinates in the body-fixed frame. The rotational energy can be rewritten

$$\hat{T}_{\text{rot}} = \frac{1}{2J} (\hat{J}^2 - \hat{J}_3^2) + \frac{1}{2J} (\hat{j}^2 - \hat{j}_3^2) + T_c \quad (5.4)$$

where

$$\hat{T}_c = -\frac{1}{2J} (\hat{J}_+ \hat{j}_- + \hat{J}_- \hat{j}_+) \quad (5.5)$$

An unsymmetrized basis state for the Hamiltonian in equation (5.1) is  $|JMK\rangle |X_\Omega\rangle$  where  $X_\Omega$  is an eigenstate of  $\hat{H}_p$

with eigenvalue  $E_\Omega$  and where  $\Omega$  is the odd particle(s) component of angular momentum along the symmetry axis. Then the diagonal matrix elements of  $\hat{H}$  are

$$E_{J\Omega} = \frac{1}{2J} [J(J+1) - K^2] + \frac{1}{2J} [\langle X_\Omega | \hat{j}^2 | X_\Omega \rangle - \Omega^2] + E_\Omega. \quad (5.6)$$

The condition that the rotor wavefunction be axially symmetric implies  $K = \Omega$ . If the basis state is symmetrized with respect to the A representation of the  $D_2$  group, there is an additional contribution to the diagonal term when  $K = \frac{1}{2}$ . The off-diagonal matrix elements of  $\hat{H}$  are

$$\begin{aligned} \langle JK'\Omega' | \hat{H} | JK\Omega \rangle &= \langle JK'\Omega' | \hat{T}_C | JK\Omega \rangle \\ &= \frac{1}{2J} \sqrt{(J+K)(J+K+1)} \langle X_{\Omega\pm 1} | \hat{j}_\pm | X_\Omega \rangle \delta_{\Omega'\Omega\pm 1} \delta_{K'K\pm 1}. \end{aligned} \quad (5.7)$$

Kerman (Ker 56) applied the above equations to  $W^{183}$  and obtained reasonably good agreement with data.

The Coriolis term can be very important in these types of calculations. Stephens et.al. (SDL+ 72, SDB+ 73, GSD 73) have emphasized that Coriolis effects become especially important for high spin states. By examining equation (5.7), it can be seen that the Coriolis matrix elements are largest when  $J$  is large and  $K(=\Omega)$  is small. If the intrinsic state can be approximated as having good angular momentum  $j$ , then the last term in equation (5.7) becomes

$$\langle X_{\Omega\pm 1} | \hat{j}_\pm | X_\Omega \rangle \approx \langle j\Omega\pm 1 | \hat{j}_\pm | j\Omega \rangle = \sqrt{(j+\Omega)(j+\Omega+1)}. \quad (5.8)$$

This matrix element is large when  $j$  is large as in, for example,

$i_{13/2}$  neutrons and  $h_{11/2}$  protons. According to the Stephens theory, the Coriolis matrix element is strong enough to decouple the odd particle from the core. That is, the particle aligns its angular momentum along the direction of rotation of the core. In this case the members of a rotational band will have angular momenta  $J, J+2, J+4, \dots$  instead of the usual  $J, J+1, J+2, \dots$ .

Meyer ter Vehn et.al. (MSD 74, Mey 75) have investigated a model in which the core is still rigid but allowed to be axially asymmetric. Also only the A representation of the  $D_2$  group is considered. Better agreement to experimental spectra is obtained with the asymmetric core.

## II. Model Calculation Single Nilsson Orbital

### 1. Hamiltonian for Odd Particle System

In most previous calculations, the odd particle wavefunction has been restricted to the A representation of the  $D_2$  group (see Appendix A). In this section we describe a simple model to investigate whether the B representations exist at sufficiently low energy to be of physical interest. This work is still under investigation and only preliminary results are presented in this thesis. The full dynamics of the (asymmetric) core is included ( $\beta$  and  $\gamma$  vibrations, rotation-vibration coupling, etc.). However to simplify the calculation, the Coriolis effects are ignored. Since Coriolis effects are important, this must be considered a very crude model. Nonetheless, it should be possible to gain some understanding of the role of the B representations.

The particle-plus-core Hamiltonian is written

$$\hat{H}_{pc} = \hat{T}_{rot} + \hat{T}_{vib} + \hat{V}_{\beta\gamma} + \hat{H}_p \quad (5.9)$$

where

$$\hat{T}_{rot} = \sum_{v=1}^3 \frac{(\hat{J}_v - \hat{j}_v)^2}{2\mathcal{I}_v(\beta, \gamma)} \quad (5.10)$$

$\mathcal{I}_v(\beta, \gamma)$  are the usual Bohr inertial functions and where  $\hat{H}_p$  is the intrinsic Hamiltonian. Using the definitions

$$J_+ = \frac{1}{2} (J_+ + J_-) , \quad J_- = -\frac{i}{2} (J_+ - J_-) \text{ etc.} \quad (5.11)$$

equation (5.10) can be written

$$\begin{aligned} \hat{T}_{rot} = & p(\hat{J}^2 - \hat{J}_3^2 + \hat{j}^2 - \hat{j}_3^2) + \frac{1}{2} r(\hat{J}_+^2 + \hat{J}_-^2) + \frac{1}{2} r(\hat{J}_+^2 + \hat{J}_-^2) \\ & - r(\hat{J}_+ \hat{j}_+ + \hat{J}_- \hat{j}_-) - p(\hat{J}_+ \hat{j}_- + \hat{J}_- \hat{j}_+) + q(\hat{J}_3 - \hat{j}_3)^2 \end{aligned} \quad (5.12)$$

where  $p$ ,  $q$  and  $r$  are defined in equation (3.19). Our approximation is to restrict the intrinsic wavefunction to have good angular momentum along the 3-axis. Hence the intrinsic wavefunction is an eigenfunction of the operator  $\hat{j}_3$  with eigenvalue  $\Omega$ . This implies the matrix elements of  $\hat{j}_\pm$  in the model space are all zero. This leads to a model rotational Hamiltonian

$$\hat{T}_{rot}^{(m)} = p(\hat{J}^2 - \hat{J}_3^2 + \hat{j}^2 - \hat{j}_3^2) + q(\hat{J}_3 - \hat{j}_3)^2 + \frac{1}{2} r(\hat{J}_+^2 + \hat{J}_-^2) \quad (5.13)$$

In order to simplify the symmetry arguments, it is further assumed that the intrinsic wavefunction has good angular momentum  $j$ .

## 2. Symmetry of Intrinsic Wavefunction: A Representation

First we note the transformation properties of the intrinsic wavefunction under the operations of the  $\hat{D}_2$  group (see Appendix A):

$$C_1^2 x_{\Omega}^j = (-1)^{-j} x_{-\Omega}^j$$

$$C_2^2 x_{\Omega}^j = (-1)^{-j+\Omega} x_{-\Omega}^j \quad (5.14-i, ii, iii)$$

$$C_3^2 x_{\Omega}^j = (-1)^{-\Omega} x_{\Omega}^j$$

An unsymmetrized particle-plus-rotor state is

$$|\psi_{JM}\rangle = \sum_{\Omega=-j}^j \sum_{K=-J}^J d_{K\Omega} |JMK\rangle x_{\Omega}^j \quad (5.15)$$

Applying to  $|\psi_{JM}\rangle$  the projection operator appropriate to the A representation and then normalizing, we obtain the state

$$|\psi_{JM}^A\rangle = \frac{1}{2\sqrt{2}} \sum_{\Omega=-j}^j \sum_{K=-J}^J d_{K\Omega} (1 + c_1^2 + c_2^2 + c_3^2) |JMK\rangle x_{\Omega}^j \quad (5.16)$$

$$= \frac{1}{2\sqrt{2}} \sum_{\Omega=-j}^j \sum_{K=-J}^J d_{K\Omega} (1 + (-1)^{K-\Omega}) [ |JMK\rangle x_{\Omega}^j + (-1)^{J-j} |JM-K\rangle x_{-\Omega}^j ] \quad (5.17)$$

This yields the condition  $K-\Omega$  even for the A representation.

By relabeling the summation index  $\Omega$  equation (5.17) can be written

$$|\psi_{JM}^A\rangle = \frac{1}{\sqrt{2}} \sum_{\Omega=\frac{1}{2}}^j \sum_{K=-J}^J (d_{K\Omega} + (-1)^{J-j} d_{-K-\Omega}) [ |JMK\rangle x_{\Omega}^j + (-1)^{J-j} |JM-K\rangle x_{-\Omega}^j ] \quad (5.18)$$

In this model calculation, only one value of  $\Omega$  is considered.

Therefore, the appropriate wavefunction for the A representation is

$$|\psi_{JM\Omega}^A\rangle = \frac{1}{\sqrt{2}} \sum_{K=-J}^J a_K [ |JMK\rangle x_{\Omega}^j + (-1)^{J-j} |JM-K\rangle x_{-\Omega}^j ] \quad (5.19)$$

where the sum is over  $K-\Omega$  even. It should be noted that both positive and negative  $K$  values must be considered in contrast to the even-even nucleus case,

### 3. Symmetry of Intrinsic Wavefunction: B Representation

Of the three B representations of the  $D_2$  group, only the  $B_2$  representation will be considered. This is because an intrinsic state in the  $B_2$  representation is even under time reversal (as is the case for the A representation, but not the  $B_1$  or  $B_2$  representations).

The procedure to obtain a state in the  $B_2$  representation is similar to that followed for the A representation. Equation (5.16) is modified to

$$|\psi_{JM}^{B_2}\rangle = \frac{1}{2\sqrt{2}} \sum_{\Omega=-j}^j \sum_{K=-J}^J d_{K\Omega} (1 - c_1^2 + c_2^2 - c_2^3) |JMK\rangle x_{\Omega}^j \quad (5.20)$$

$$= \frac{1}{2\sqrt{2}} \sum_{\Omega=-j}^j \sum_{K=-J}^J d_{K\Omega} (1 - (-1)^{K-\Omega}) [ |JMK\rangle x_{\Omega}^j - (-1)^{J-j} |JM-K\rangle x_{-\Omega}^j ] \quad (5.21)$$

Hence  $K-\Omega$  must be odd for the  $B_2$  representation. The final result is

$$|\psi_{JM}^{B_2}\rangle = \frac{1}{\sqrt{2}} \sum_{K=-J}^J a_K [ |JMK\rangle x_{\Omega}^j - (-1)^{J-j} |JM-K\rangle x_{-\Omega}^j ] \quad (5.22)$$

#### 4. Matrix Elements of $\hat{T}_{rot}^{(m)}$

The matrix elements have the same form between basis states of the A representation (equation (5.19)) and between states of the  $B_2$  representation (equation (5.22)). As a result, we need only describe the evaluation of the matrix elements for the A representation. The wavefunction  $|\psi_{JM\Omega}^A\rangle$  has been expressed in a basis of states  $|\phi_{JM\Omega K}^A\rangle$  where

$$|\phi_{JM\Omega K}^A\rangle = \frac{1}{\sqrt{2}} [ |JMK\rangle x_{\Omega}^j + (-1)^{J-j} |JM-K\rangle x_{-\Omega}^j ] \quad (5.23)$$

In this basis, the diagonal matrix elements of  $\hat{T}_{rot}^{(m)}$  are

$$\langle \phi_{JM\Omega K}^A | \hat{T}_{rot}^{(m)} | \phi_{JM\Omega K}^A \rangle = p[J(J+1) - K^2 + j(j+1) - \Omega^2] + q(K - \Omega)^2 \quad (5.24)$$

The off-diagonal matrix elements are

$$\langle \phi_{JM\Omega K-2}^A | \hat{T}_{rot}^{(m)} | \phi_{JM\Omega K}^A \rangle = \frac{1}{2} r \sqrt{(J+K-1)(J-K+2)(J+K)(J-K+1)} \quad (5.25)$$

The eigenfunctions of  $\hat{H}_{pc}$  are obtained as in the even-even case except the rotational kinetic energy matrix elements are given by equation (5.23) instead of (3.24) and (3.25).

### III. Results of Model Calculation

Using a potential energy surface with a single minimum on the prolate axis,  $\hat{H}_{pc}$  is solved for angular momentum states  $J = 11/2, 13/2, \dots, 21/2$ . The intrinsic wavefunction is restricted to having good  $j = 11/2$  and good  $\Omega = 11/2$ . Wavefunctions of both the A and  $B_2$  representations are chosen. To limit the time required to do the computation, it was necessary to restrict

the number of K-components. For the A representation the wavefunction was restricted to having  $K = 7/2, 11/2$  and  $15/2$  since  $K-\Omega$  must be even. For  $J = 19/2$ , the respective probabilities of the wavefunction having those K-components are 2%, 91% and 7%. It is expected that if the wavefunction were allowed to have additional K-components (for example  $K = 3/2$  and  $K = 19/2$ ) these additional K-components would appear with low probability. The K-components for which  $K \approx \Omega$  are most probable because of the last term in equation (5.24). For the  $B_2$  representation, the wavefunction was restricted to having  $K = 9/2$  and  $13/2$  since  $K-\Omega$  must be odd.

The energy levels obtained from this calculation are shown on Figure 5.1. In all cases the Yrast state is of the A representation. It is very significant that, in general, the state of the  $B_2$  representation lies lower in energy than the first excited state of the A representation. Hence this model calculation indicates that states of the  $B_2$  representation are of physical interest.

For purposes of comparison, the experimental energies of the  $11/2^+$  band of  $Gd^{151}$  (SWJ 75) are given in Figure 5.2. For  $J = 13/2, 15/2, 17/2$  and  $21/2$  there is a state at only slightly higher energy than the Yrast state. It may be possible to explain these non-Yrast states using wavefunctions of the  $B_2$  representation. No attempt was made to choose a potential energy  $V(\beta, \gamma)$  to fit the  $Gd^{151}$  data. In fact the calculated spectra is considerably less compressed than the experimental



Calculated energy levels for A and B representations. The energy levels are obtained by solving the Hamiltonian given in equation (5.9) except  $\hat{T}_{\text{rot}}$  is given by equation (5.13) instead of equation (5.10).

Figure 5.1

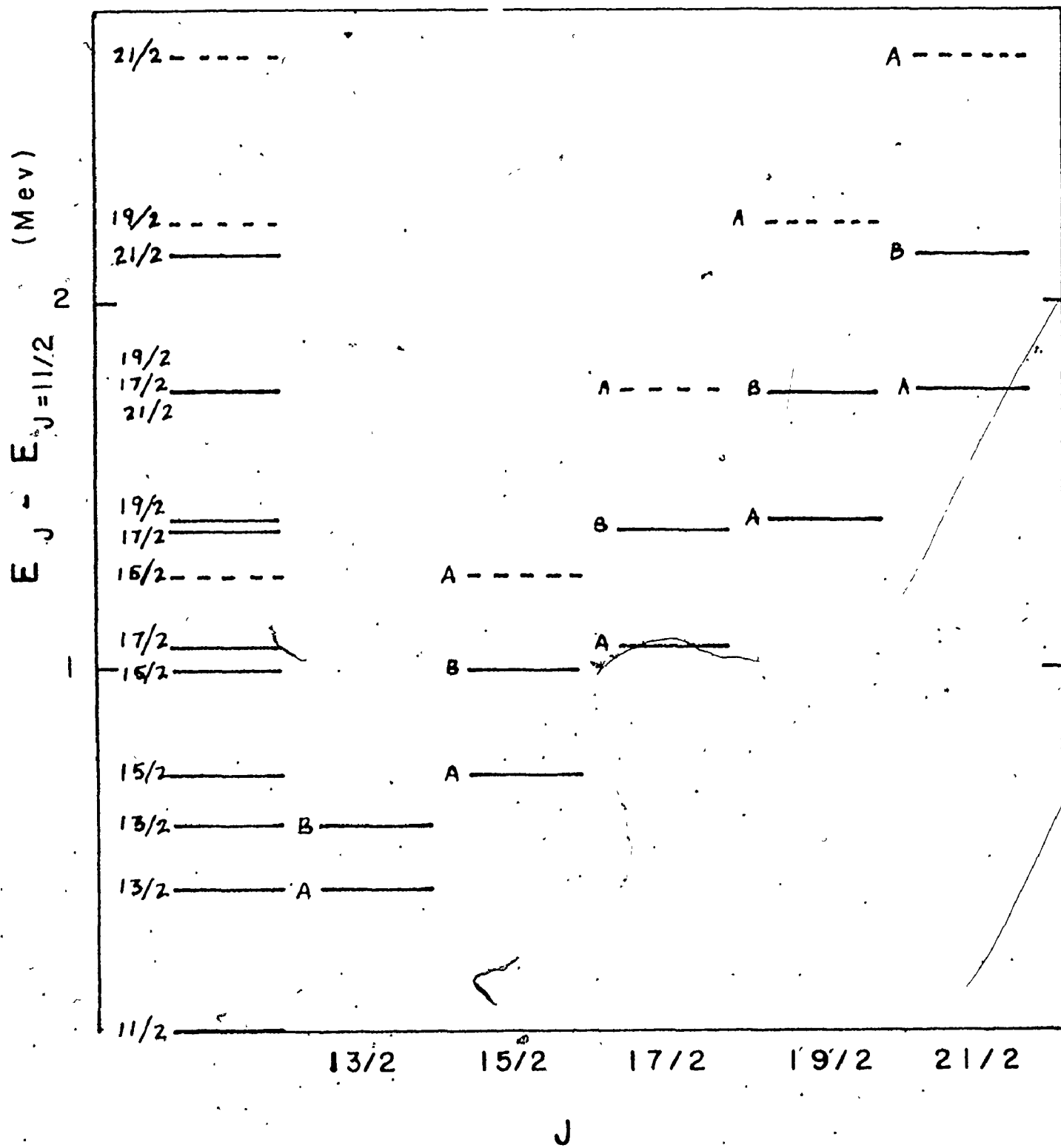
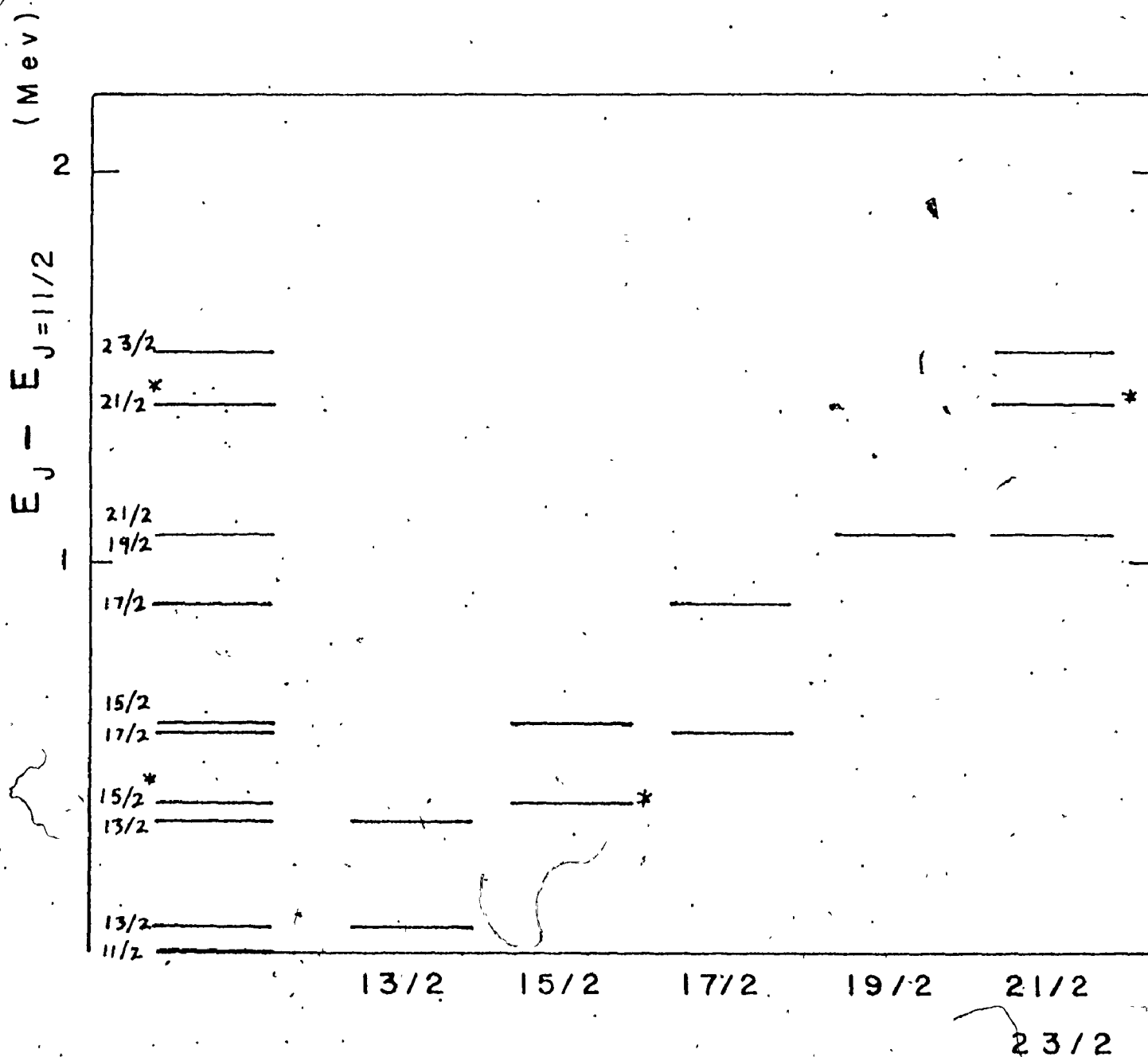


Figure 5.2

Some experimental energy levels of  $\text{Cd}^{151}$ . Only positive parity levels are given. The tentative identifications are indicated by asterisks.



spectra. Also the experimental spectra show staggering, probably due to Coriolis effects.

There are several improvements that can be made to the calculation described in this chapter. One possible calculation is to do a full Coriolis-coupled calculation with a rigid axially-asymmetric rotor as Meyer ter Vehn has done. However, both the A and B representations must be considered instead of just the A representation. A more ambitious calculation is to solve the full Hamiltonian given in equation (5.9). However many technical problems would have to be solved before such a calculation would become possible.

## CHAPTER 6

### SUMMARY AND DISCUSSION

Recent advances in experimental technique have made possible the investigation of nuclear systems in high spin states. This experimental work received great impetus when the phenomenon of backbending was first observed (JRH 72). Several theoretical models have been proposed to understand this so-called phase transition. In this thesis, two collective models for high spin states have been given. The predictions of these models have been calculated and compared with each other as well as with experiment. The basic idea of both these models is that nuclei become axially asymmetric in high spin states.

In Chapter 2, some of the early models of the spectra of even-even nuclei were briefly described. This is not meant to be an exhaustive list of previous models. It has been shown that in all cases, the earlier models became inadequate for high spin. One model which is valid for spin as high as  $J \approx 10$  is the Variable Moment of Inertia (VMI) model of Mariscotti, Scharff-Goldhaber and Buck (MSB 69). This model has been described in considerable detail since it formed a basis for a more generalized theory developed by Smith and Volkov (SV 73). The conventional statement of the VMI model has been given in Chapter 2. A more mathematical statement

of this model has been developed in Chapter 4. In Chapter 2, the concept of backbending has been defined. It has been shown that nuclear states above the backbending point could not be adequately described by the original VMI model. However this model has been very successful in giving the energy levels of the states below the backbending point. The fact that this two parameter model leads to an excellent description of five or more pieces of data suggests that there is a deep underlying principle involved. This thesis has described how the VMI model is a result of the variational principle of quantum-mechanics. Hence the VMI model is more than just another phenomenological theory. It has a firm basis in quantum-mechanics. Furthermore, it has been shown that the original VMI model is only one of a class of VMI type theories arising from the variational principle.

One such theory, namely the VMIA theory, has been described in detail. This model is a generalization of the original VMI theory in that the model includes the possibility of axial asymmetry. Moreover the amount of axial asymmetry (described by the quantity  $\gamma$ ) depends on the angular momentum of the state. It has been shown that above some critical angular momentum  $J_c$ , the nucleus can further reduce its rotational energy by becoming axially asymmetric. This implies that for  $J < J_c$ ,  $\gamma_J \approx 0$  whereas for  $J > J_c$ ,  $\gamma \approx \pi/6$ . It has been shown that this gain in energy is sufficient to cause backbending. The VMIA model predicts that the axially symmetric

solution ( $\gamma \approx 0$ ) persists above the critical angular momentum albeit at higher energy. These predicted additional states may explain "forking" which has been observed experimentally in  $\text{Ba}^{126}$  and  $\text{Os}^{186}$ .

The VMIA model has been extended in this thesis to allow the calculation of the lower members of the  $\gamma$  band. A projection technique has been used to ensure that the states in the  $\gamma$  band are orthogonal to states in the ground state band. The  $\gamma$  bandhead gives information on the " $\gamma$ -stiffness" of the nucleus. This is of considerable importance because in our model, backbending is related to  $\gamma$  deformation. It has been shown that the experimental critical "backbending" angular momentum is higher for the more " $\gamma$ -stiff" nuclei.

There are several ambiguities connected with the VMIA model arising from the fact that it is not fully quantum-mechanical. In particular there is the question of the nature of the states in the  $\gamma$  band for  $J > J_c$ . This difficulty arises from the fact that for  $J > J_c$ , the members of the Yrast band are as axially asymmetric as the lower  $\gamma$  band members. A second possible objection to the VMIA model is that the model does not display in an unambiguous fashion the role of band crossing. A third objection is that the model inhibits the effect of the mixing of states and hence the backbending occurs too suddenly.

In order to investigate these deficiencies, the conse-

quences of the fully quantum-mechanical Bohr-Mottelson collective model (Boh 52, BM 53) were examined since this model allows for the possibility of non-axial deformation and band crossing as well as other rotation-vibration effects. In order to investigate the backbending phenomenon, it is necessary to be able to solve the Bohr Hamiltonian for spins as high as  $J \approx 20$ . This poses a technical problem of considerable magnitude. A new method of solution has been developed which is valid for arbitrary potential surfaces and arbitrary inertial functions. The method involves converting the Schroedinger equation into a system of coupled differential equations. Using finite difference techniques the system is transformed into a matrix eigenvalue equation. Because the dimensionality of the matrix to be diagonalized can be as large as  $1899 \times 1899$ , it has been found expedient to use the Lanczos algorithm to perform the diagonalization.

This method of solving the Bohr Hamiltonian has been tested for the cases of a harmonic oscillator and a well deformed prolate rotor and has been found to be sufficiently accurate. Suitable collective potential surfaces have been determined which give an approximate fit to the data for the nuclei  $\text{Er}^{164}$ ,  $\text{Er}^{162}$  and  $\text{Os}^{182}$ . In each of the three cases, the critical angular momentum for backbending agrees with experiment. In addition to the (backbending) ground state band, the data fitted included the  $\gamma$  band and in the case of  $\text{Er}^{164}$ , the  $\beta$ -band.



In  $\text{Er}^{164}$  and  $\text{Er}^{162}$ , a two minima collective potential has been used: one minimum on the ~~prolate~~ axis and one minimum in the asymmetric region. It has been found that at the critical angular momentum, the Yrast states become more asymmetric. Essentially what happens is that the  $\gamma$  band crosses the ground state band and thus becomes the "Yrast band". Because the odd  $J$  members of the  $\gamma$  band are displaced upward in energy with respect to the even  $J$  members, the odd  $J$  members are not expected to be readily observed experimentally.

A two minima potential also has been used for  $\text{Os}^{182}$ . However in this case one minimum is on the prolate axis and the second minimum is on the oblate axis. Again a sudden shape change is calculated for a critical angular momentum. As a separate check on the model,  $B(E2)$ 's have been calculated using the collective wavefunctions obtained from solving the Bohr Hamiltonian. Since the lifetime data have large experimental uncertainty for high spin states, no direct comparison has been made to the data. The calculated  $B(E2)$ 's agree with the rigid rotor estimate to within a factor of two and consequently are in qualitative agreement with experiment.

By comparing the variable moment of inertia model with the Bohr collective model, it has been possible to investigate the potential  $V$  appearing in the variable moment of inertia model. It has been found that this  $V$  corresponds to the sum of vibrational and potential energies rather than to just the potential energy.

Preliminary results have been presented for the calculation of the spectra of odd particle nuclei within the framework of the Bohr collective model. It has been suggested that some states of  $Gd^{151}$  can be explained as arising from a wavefunction of the  $B_2$  representation of the  $D_2$  group. This is quite significant since normally only the A representation is considered for solutions of the Bohr collective model. However, more elaborate calculations will have to be performed before the role of the B representations is understood in detail.

## APPENDIX A

### $D_2$ GROUP

The set of transformation operators  $\{E, c_1^2, c_2^2, c_3^2\}$  form a group under composition. The symbol  $c_v^2$  is the operator of rotation by  $\pi$  radians about the  $v$ -axis where  $v = 1, 2, 3$ .

The symbol  $E$  stands for the identity operator. This group is called the  $D_2$  group. It has four one-dimensional irreducible representations:  $A, B_1, B_2, B_3$ . The character table of the group is given in Table A.1.

Table A.1: Character Table of  $D_2$  Group

$D_2$	$E$	$c_1^2$	$c_2^2$	$c_3^2$
$A$	1	1	1	1
$B_1$	1	-1	-1	1
$B_2$	1	-1	1	-1
$B_3$	1	1	-1	-1

A general element of the above matrix will be represented by  $p_v^R$ , where  $R$  stands for a particular representation:  $A, B_1, B_2$  or  $B_3$ . The symbol  $v$  denotes the group element by indicating the axis of rotation ( $v = 0$  corresponds to the identity element).

## APPENDIX B

### THE QUANTUM-MECHANICAL ASYMMETRIC ROTOR.

The Hamiltonian for an asymmetric rigid rotor can be expressed as

$$\hat{R} = a \hat{J}_1^2 + b \hat{J}_2^2 + c \hat{J}_3^2 \quad (B.1)$$

where  $\hat{J}_i, i = 1, 2, 3$  are the angular momentum operators about the three principle axes fixed in the rotor (body-fixed axes). The rotational parameters are related to the principle moments of inertia by

$$a^{-1} = 2J_1, \quad b^{-1} = 2J_2, \quad c^{-1} = 2J_3 \quad (B.2)$$

Because the state of a rigid rotor can be described completely by three Euler angles,  $\theta_1, \theta_2$  and  $\theta_3$ , the operators  $\hat{J}_i$  are written in terms of these Euler angles. A general asymmetric rotor wavefunction  $\langle \theta_1 \theta_2 \theta_3 | JM \rangle$  can be expanded in terms of the Wigner rotation matrix functions  $D_{MK}^J(\theta_1, \theta_2, \theta_3)$ . The  $D_{MK}^J$  functions are eigenfunctions of the angular momentum operators:

$$\hat{J}^2 D_{MK}^J(\theta_1, \theta_2, \theta_3) = J(J+1) D_{MK}^J(\theta_1, \theta_2, \theta_3) \quad (B.3-i)$$

$$\hat{J}_3 D_{MK}^J(\theta_1, \theta_2, \theta_3) = K D_{MK}^J(\theta_1, \theta_2, \theta_3) \quad (B.3-ii)$$

$$\hat{J}_z D_{MK}^J(\theta_1, \theta_2, \theta_3) = M D_{MK}^J(\theta_1, \theta_2, \theta_3) \quad (B.3-iii)$$

Here  $\hat{J}_z$  is the component of  $\hat{J}$  along the z-axis in the space-fixed co-ordinate system.

The  $D_{MK}^J(\theta_1, \theta_2, \theta_3)$  satisfy the integral relation

$$\int |D_{MK}^J(\theta_1, \theta_2, \theta_3)|^2 \sin \theta_2 d\theta_1 d\theta_2 d\theta_3 = \frac{8\pi^2}{2J+1} \quad (B.4)$$

Hence it is convenient to define normalized angular momentum states by

$$(\theta_1, \theta_2, \theta_3 | JMK) = \sqrt{\frac{2J+1}{8\pi^2}} D_{MK}^J(\theta_1, \theta_2, \theta_3). \quad (B.5)$$

For each of the symmetry operations of the  $D_2$  group, the operators  $\hat{J}_\alpha$  either change sign or remain invariant. In addition the rotational parameters  $a$ ,  $b$  and  $c$  are invariant under operations of the  $D_2$  group. As a result the asymmetric rotor Hamiltonian,  $\hat{R}$ , remains invariant under operations of the  $D_2$  group. This allows the eigenstates of  $\hat{R}$  to be classified by the irreducible representations of the  $D_2$  group. The Hamiltonian will have no matrix elements between states of different representations.

The most general eigenstate of  $\hat{R}$  (with total angular momentum  $J$  and z-component  $M$ ) can be written as

$$|\psi_{JM}\rangle = \sum_{K=-J}^J d_K |JMK\rangle$$

For conciseness the Euler angle notation has been omitted.

An eigenstate of representation  $R$  is obtained by acting on the state  $|\psi_{JM}\rangle$  with the projection operator

$$\hat{O}_R \equiv \sum_{v=0}^3 P_v^R C_v^2. \quad (B.7)$$

(See Appendix A for notation.) For the case of the A representation this yields the state

$$|\psi_{JM}^A\rangle = \sum_{K=-J}^J d_K (1 + C_1^2 + C_2^2 + C_3^2) |JMK\rangle. \quad (B.8)$$

Using the Davydov (Dav 66) convention for the  $D_{MK}^J$  matrices,  $D_2$  operations on the function  $D_{MK}^J$  give

$$C_1^2 D_{MK}^J = (-1)^J D_{M-K}^J \quad (B.9-i)$$

$$C_2^2 D_{MK}^J = (-1)^{J-K} D_{M-K}^J \quad (B.9-ii)$$

$$C_3^2 D_{MK}^J = (-1)^K D_{MK}^J \quad (B.9-iii)$$

Assuming that  $J$  is integral and combining equations (B.5), (B.8) and (B.9), the rotor state is

$$|\psi_{JM}^A\rangle = \sum_{K=0}^J (1 + (-1)^K) \frac{(d_K + (-1)^J d_{-K})}{1 + \delta_{K0}} [ |JMK\rangle + (-1)^J |JM-K\rangle ]. \quad (B.10)$$

This equation indicates that  $K$  must be even for the A representation. If  $K=0$ ,  $J$  must be even. Hence  $J=1$  is forbidden. If the wavefunction is symmetric about the  $z$ -axis, then  $K=0$  and hence  $J$  is even.

Equation (B.10) can be written

$$|\psi_{JM}^A\rangle = \sum_{K=0(2)}^J a_{JK} |\phi_{MK}^J\rangle \quad (B.11)$$

where

$$|\phi_{MK}^J\rangle = \frac{1}{\sqrt{2(1+\delta_{K0})}} [ |JMK\rangle + (-1)^J |JM-K\rangle ] \quad (B.12)$$

and

$$a_{JK} = \frac{2\sqrt{2}}{\sqrt{1+\delta_{K0}}} (d_K + (-1)^J d_{-K}). \quad (B.13)$$

The prime denotes summation over even  $K$  only. The lower limit of the sum is 0 or 2 if  $J$  is even or odd respectively. It turns out that the A representation is the only representation which allows  $J=0$  for positive parity states. As a result, in this model the ground state of an even-even nucleus must be in the A representation.

The rotor energies and coefficients  $a_{JK}$  are determined by diagonalizing the rotor Hamiltonian  $\hat{R}$  in the basis formed from states defined by equation (B.12). Since  $J$  and  $M$  are good quantum numbers, only the  $K$  quantum number is mixed in the matrix diagonalization. For a given angular momentum  $J$ , the different magnetic substates (given by  $M$ ) are all degenerate. Hence the quantum number  $M$  can be ignored. For angular momentum  $J$ , the dimensionality of the matrix is  $J/2+1$  if  $J$  is even and  $(J-1)/2$  if  $J$  is odd.

## APPENDIX C

### SYMMETRIES OF THE BOHR COLLECTIVE HAMILTONIAN

Most discussions of the symmetry of the Bohr Hamiltonian (eg, KB 67) have followed along the line originally given by Bohr (Boh 52). In this method, it is observed that there are 24 different ways of attaching a right-handed set of axes to a spheroidal nucleus and hence 24 different ways of defining  $\beta$ ,  $\gamma$  and the three Euler angles. Each of the 24 configurations of the principle axes can be generated by repeated application of the three symmetry operators  $R_1$ ,  $R_2$  and  $R_3$ .  $R_1$  is a rotation by  $\pi$  about the z-axis.  $R_2$  and  $R_3$  will be defined later in this appendix. It is then asserted that the wavefunction is invariant under each of these symmetry operations; i.e.

$$R_i \psi = + \psi \quad i = 1, 2, 3. \quad (C.1)$$

This method is restrictive in that the B representations of the  $D_2$  group are ruled out a priori.

In this Thesis an alternative procedure is used which is more general. Attention is focussed on the symmetry operations of the Hamiltonian,  $\hat{H}_B$  (see equation (3.14)). The eigenstates of  $\hat{H}_B$  are then classified as irreducible representations of the appropriate symmetry group. There are several symmetry operations of  $\hat{H}_B$ . Three of these are the same as the three symmetry operations of the asymmetric



rotor. Denoted by  $c_1^2$ ,  $c_2^2$  and  $c_3^2$  the corresponding symmetry operators rotate the body-fixed co-ordinate system about each of the principle axes of the spheroidal nucleus.

The effect of the operator  $c_v^2$  on the angular momentum operators has already been described in Appendix B. To see the effect of  $c_v^2$  on the shape co-ordinates  $\beta$  and  $\gamma$ , it is necessary to examine equation (3.1) which defines  $\beta$  and  $\gamma$ . From this equation it can be seen that the three semi-axes of the spheroid are given by

$$R_1 = R_0 \left( 1 + \sqrt{\frac{5}{4\pi}} \beta \cos \left( \gamma + \frac{2\pi}{3} \right) \right) \quad (\text{C.2-i})$$

$$R_2 = R_0 \left( 1 + \sqrt{\frac{5}{4\pi}} \beta \cos \left( \gamma + \frac{2\pi}{3} \right) \right) \quad (\text{C.2-ii})$$

$$R_3 = R_0 \left( 1 + \sqrt{\frac{5}{4\pi}} \beta \cos \gamma \right) \quad (\text{C.2-iii})$$

It can be seen that rotation by  $\pi$  about each of the three axes does not affect either  $\beta$  or  $\gamma$ . Hence  $\hat{T}_{\text{vib}}$ ,  $\hat{V}$  and the three moments of inertia  $\mathcal{I}_v(\beta, \gamma)$  (all of which depend on  $\beta$  and  $\gamma$  only) are unaffected by this transformation. Therefore,  $\hat{H}_B$  is invariant under the transformations given by  $c_v^2$ . Since these three operators, along with the identity operator, form the  $D_2$  group, the methods of Appendix B can be employed. For the even-even case, it appears that the A representation of the  $D_2$  group is the only representation of physical interest for the low lying states because of the nature of the intrinsic state of the nucleus (see DV, 72). However, in an odd particle

system, the B' representations may play a role.

Another symmetry operator of  $\hat{H}_B$  is  $R_2$ , the rotation by  $\pi/2$  about the 3-axis. Under  $R_2$ ,  $\hat{J}_1 \rightarrow \hat{J}_2$ ,  $\hat{J}_2 \rightarrow \hat{J}_1$ ,  $\hat{J}_3 \rightarrow \hat{J}_3$ . By examining equation (C.2), it can be seen that  $\gamma \rightarrow -\gamma$ . The transformation  $\gamma \rightarrow -\gamma$  affects the moments of inertia  $J_v(\beta, \gamma)$  in the following way:

$$J_1(\beta, \gamma) = 4B\beta^2 \sin^2(\gamma - \frac{2\pi}{3}) + 4B\beta^2 \sin^2(\gamma + \frac{2\pi}{3}) = J_2(\beta, \gamma)$$

$$J_2(\beta, \gamma) = 4B\beta^2 \sin^2(\gamma - \frac{4\pi}{3}) + 4B\beta^2 \sin^2(\gamma + \frac{4\pi}{3}) = J_1(\beta, \gamma)$$

$$J_3(\beta, \gamma) = 4B\beta^2 \sin^2 \gamma + 4B\beta^2 \sin^2 \gamma = J_3(\beta, \gamma)$$

Hence under  $R_2$ ,  $\hat{T}_{\text{rot}} = \sum_{v=1}^3 \frac{\hat{J}_v^2}{2J_v(\beta, \gamma)}$  is invariant. Moreover the operator  $\gamma \rightarrow -\gamma$  does not alter  $\hat{T}_{\text{vib}}$ . In order that the potential energy operator,  $\hat{V}$ , does not destroy the symmetry it is necessary that  $V(\beta, \gamma) = V(\beta, -\gamma)$ . Since each of  $\hat{T}_{\text{rot}}$ ,  $\hat{T}_{\text{vib}}$  and  $\hat{V}$  is invariant under  $R_2$ , so is  $\hat{H}_B$ . It is possible to classify the eigenfunctions of  $\hat{H}_B$  as having either even or odd parity under  $R_2$ . Both possibilities imply K is even (KB 67). This is compatible with the A and  $B_1$  representations but not with the  $B_2$  and  $B_3$  representations.

Another symmetry operator of  $\hat{H}_B$  is the operator  $R_3$  which is a rotation of  $\pi/2$  about the 3-axis followed by a rotation of  $\pi/2$  about the 1 axis. This corresponds to a cyclical permutation of the axes. Under this transformation,  $\hat{J}_1 \rightarrow \hat{J}_3$ ,  $\hat{J}_2 \rightarrow \hat{J}_1$ ,  $\hat{J}_3 \rightarrow \hat{J}_2$  and  $\gamma \rightarrow \gamma + 2\pi/3$ . Under  $R_3$ ,  $\hat{H}_B$  is invariant provided the collective potential has the property

$$V(\beta, \gamma) = V(\beta, \gamma + 2\pi/3).$$

The symmetry operators  $R_2$  and  $R_3$  have been included for completeness. The wavefunction will not be classified by its properties under the  $R_2$  or  $R_3$  symmetry operators. Only irreducible representations of the  $D_2$  group will be employed.

## APPENDIX D

### BRIEF DESCRIPTION OF SPLINE FUNCTIONS

In this appendix, spline functions (Rei 67) will be defined. A spline function  $f(x)$  is used to interpolate or smooth a function  $y(x)$  which is known only at discrete points  $x_i$ ,  $i = 0, 1, 2, \dots, n$ . We define  $y_i = y(x_i)$ . The interval on which the spline is to be defined is divided up into several (not necessarily equal) sub-intervals. The endpoints of the sub-intervals are called the knots of the spline. Within each sub-interval, the spline is defined to be equal to a polynomial. However, in general, the polynomial is different for each sub-interval. Each of the polynomials must have the same degree. Another restriction on the spline is that  $f \in C^2$ . In particular this means that  $f(x)$ ,  $f'(x)$  and  $f''(x)$  are continuous at each of the knots. Although the polynomials of the spline can have any degree greater than two, the most common degree is three. In this thesis, only cubic splines have been used.

Often the value of the function at the discrete points is not known with infinite precision. In this case splines can be used to "smooth" the function. The condition that the spline  $f$  be a good approximation to the given function  $y$  is

$$\sum_{i=0}^n \left( \frac{f(x_i) - y_i}{\delta y_i} \right)^2 \leq 1 \quad (D.1)$$

where  $\delta y_i$  gives the relative uncertainty of the value  $y_i$ . If

the knots of the spline are taken to be the values  $x_i$ ,  $i = 0, 1, 2, \dots, n$ , then there is a large class of cubic splines satisfying condition (D.1). The particular spline chosen is the one which minimizes the quantity

$$\int_{x_0}^{x_n} (f''(x))^2 dx.$$

## APPENDIX E

### NUMERICAL INTEGRATION AND DIFFERENTIATION WEIGHTS

The 10 coefficients of the polynomial  $P_3(x,y)$  discussed in Chapter 3, Section III-2, are related to the function values at the grid points as follows:

i) Point A  $(0, \sqrt{3})$ :  

$$3\sqrt{3} d + 3g + \sqrt{3} j + k = f_A \quad (\text{E.1-i})$$

ii) Point B  $(-\frac{1}{2}, \frac{\sqrt{3}}{2})$ :  

$$-\frac{1}{8} a + \frac{\sqrt{3}}{8} b - \frac{3}{8} c + \frac{3\sqrt{3}}{8} d + \frac{1}{4} e - \frac{\sqrt{3}}{4} f + \frac{3}{4} g - \frac{1}{2} h + \frac{\sqrt{3}}{2} j + k = f_B \quad (\text{E.1-ii})$$

iii) Point C  $(\frac{1}{2}, \frac{\sqrt{3}}{2})$ :  

$$\frac{1}{8} a + \frac{\sqrt{3}}{8} b + \frac{3}{8} c + \frac{3\sqrt{3}}{8} d + \frac{1}{4} e + \frac{\sqrt{3}}{4} f + \frac{3}{4} g + \frac{1}{2} h + \frac{\sqrt{3}}{2} j + k = f_C \quad (\text{E.1-iii})$$

iv) Point D  $(-1, 0)$ :  

$$-a + e - h + k = f_D \quad (\text{E.1-iv})$$

v) Point E  $(0, 0)$ :  

$$k = f_E \quad (\text{E.1-v})$$

vi) Point F  $(1, 0)$ :  

$$a + e + h + k = f_F \quad (\text{E.1-vi})$$

vii) Point G  $(-\frac{3}{2}, -\frac{\sqrt{3}}{2})$ :

$$-\frac{27}{8}a - \frac{9\sqrt{3}}{8}b - \frac{9}{8}c - \frac{3\sqrt{3}}{8}d + \frac{9}{4}e + \frac{3\sqrt{3}}{4}f + \frac{3}{4}g$$

$$- \frac{3}{2}h - \frac{\sqrt{3}}{2}j + k = f_G \quad (\text{E.1-vii})$$

viii) Point H  $(-\frac{1}{2}, -\frac{\sqrt{3}}{2})$ :

$$-\frac{1}{8}a - \frac{\sqrt{3}}{8}b - \frac{3}{8}c - \frac{3\sqrt{3}}{8}d + \frac{1}{4}e + \frac{\sqrt{3}}{4}f + \frac{3}{4}g$$

$$- \frac{1}{2}h - \frac{\sqrt{3}}{2}j + k = f_H \quad (\text{E.1-viii})$$

ix) Point I  $(\frac{1}{2}, -\frac{\sqrt{3}}{2})$ :

$$\frac{1}{8}a - \frac{\sqrt{3}}{8}b + \frac{3}{8}c - \frac{3\sqrt{3}}{8}d + \frac{1}{4}e - \frac{\sqrt{3}}{4}f + \frac{3}{4}g + \frac{1}{2}h$$

$$- \frac{\sqrt{3}}{2}j + k = f_I \quad (\text{E.1-ix})$$

x) Point J  $(\frac{3}{2}, -\frac{\sqrt{3}}{2})$ :

$$\frac{27}{8}a - \frac{9\sqrt{3}}{8}b + \frac{9}{8}c - \frac{3\sqrt{3}}{8}d + \frac{9}{4}e - \frac{3\sqrt{3}}{4}f + \frac{3}{4}g$$

$$+ \frac{3}{2}h - \frac{\sqrt{3}}{2}j + k = f_J \quad (\text{E.1-x})$$

The solution of the above system of equations gives the polynomial coefficients in terms of the grid point function values as follows:

$$6a = -f_G + 3f_H - 3f_I + f_J \quad (\text{E.2-i})$$

$$2\sqrt{3}b = 2f_D - 4f_E + 2f_F - f_G + f_H + f_I - f_J \quad (\text{E.2-ii})$$

$$3c = -2f_B + 2f_C + 2f_D - 2f_F - \frac{1}{2}f_G - \frac{1}{2}f_H + \frac{1}{2}f_I + \frac{1}{2}f_J \quad (\text{E.2-iii})$$

$$3\sqrt{3}d = \frac{4}{3}f_A - 2f_B - 2f_C + f_D + 2f_E + f_F - \frac{1}{6}f_G - \frac{1}{2}f_H$$

$$- \frac{1}{2}f_I - \frac{1}{6}f_J \quad (\text{E.2-iv})$$

$$2e = f_D - 2f_E + f_F$$

(E.2-v)

$$\sqrt{3}f = -f_B + f_C + f_H - f_I$$

(E.2-vi)

$$6g = 2f_B + 2f_C - f_D - 6f_E - f_F + 2f_H + 2f_I$$

(E.2-vii)

$$2h = -f_D + f_F + \frac{1}{3}f_G - f_H + f_I - \frac{1}{3}f_J$$

(E.2-viii)

$$3\sqrt{3}j = -f_A + 3f_B + 3f_C - \frac{3}{2}f_D - \frac{3}{2}f_F + \frac{1}{2}f_G - \frac{3}{2}f_H + \frac{1}{2}f_J$$

(E.2-ix)

$$k = f_E$$

(E.2-x)

Using equations (E.2) the partial derivatives of  $P'_3(x, y)$  can be written in terms of the function  $g(x, y)$  (see Chapter 3, section III-3) as:

$$\left. \frac{\partial P'_3(x, y)}{\partial x} \right|_A = -3g_B + 3g_C + \frac{3}{2}g_D - \frac{3}{2}g_F - \frac{1}{3}g_G + \frac{1}{3}g_J \quad (\text{E.3-i})$$

$$\left. \frac{\partial P'_3(x, y)}{\partial y} \right|_A = \sqrt{3} \left( \frac{11}{9}g_A - g_B - g_C + \frac{1}{2}g_D + \frac{1}{2}g_F - \frac{1}{9}g_G - \frac{1}{9}g_J \right) \quad (\text{E.3-ii})$$

$$\left. \frac{\partial P'_3(x, y)}{\partial y} \right|_B = -g_B + g_C - g_D + 2g_E - g_F + \frac{1}{6}g_G - \frac{1}{2}g_I + \frac{1}{3}g_J \quad (\text{E.3-iii})$$

$$\left. \frac{\partial P'_3(x, y)}{\partial y} \right|_B = \sqrt{3} \left( \frac{2}{9}g_A + \frac{2}{2}g_B - \frac{1}{3}g_C - \frac{1}{3}g_D - \frac{2}{3}g_E + \frac{1}{3}g_F + \frac{1}{18}g_G + \frac{1}{6}g_I - \frac{1}{9}g_J \right) \quad (\text{E.3-iv})$$

$$\left. \frac{\partial P'_3(x, y)}{\partial x} \right|_C = -g_B + g_C + g_D - 2g_E + g_F - \frac{1}{3}g_G + \frac{1}{2}g_H - \frac{1}{6}g_J \quad (\text{E.3-v})$$

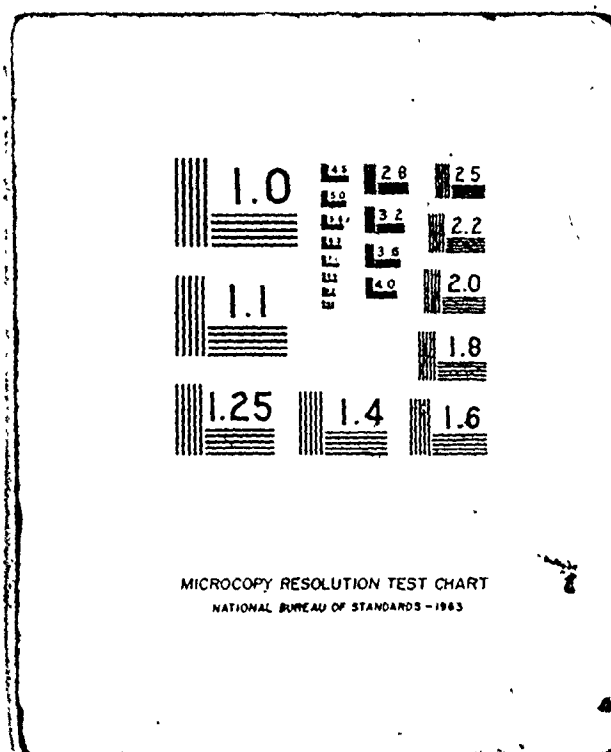
$$\left. \frac{\partial P'_3(x, y)}{\partial y} \right|_C = \sqrt{3} \left( \frac{2}{9}g_A - \frac{1}{3}g_B + \frac{2}{3}g_C + \frac{1}{3}g_D - \frac{2}{3}g_E - \frac{1}{3}g_F - \frac{1}{9}g_G + \frac{1}{6}g_H + \frac{1}{18}g_J \right) \quad (\text{E.3-vi})$$

$$\left. \frac{\partial P'_3(x, y)}{\partial x} \right|_D = -\frac{3}{2}g_D + 2g_E - \frac{1}{2}g_F - \frac{1}{3}g_G + g_H - g_I + \frac{1}{3}g_J \quad (\text{E.3-vii})$$



3 3

OF/DE



$$\left. \frac{\partial P_3'(x, Y)}{\partial y} \right|_D = \sqrt{3} \left( -\frac{1}{9} g_A + \frac{2}{2} g_B + \frac{1}{6} g_D - \frac{2}{3} g_E + \frac{1}{6} g_F - \frac{1}{9} g_G \right. \\ \left. - \frac{1}{3} g_H + \frac{1}{3} g_I - \frac{1}{9} g_J \right) \quad (\text{E.3-viii})$$

$$\left. \frac{\partial P_3'(x, Y)}{\partial x} \right|_E = -\frac{1}{2} g_D + \frac{1}{2} g_F + \frac{1}{6} g_G - \frac{1}{2} g_H + \frac{1}{2} g_I - \frac{1}{6} g_J \quad (\text{E.3-ix})$$

$$\left. \frac{\partial P_3'(x, Y)}{\partial y} \right|_E = \sqrt{3} \left( -\frac{1}{9} g_A + \frac{1}{3} g_B + \frac{1}{3} g_C - \frac{1}{6} g_D - \frac{1}{6} g_F + \frac{1}{18} g_G \right. \\ \left. - \frac{1}{6} g_H - \frac{1}{6} g_I + \frac{1}{18} g_J \right) \quad (\text{E.3-x})$$

$$\left. \frac{\partial P_3'(x, Y)}{\partial x} \right|_F = \frac{1}{2} g_D - 2g_E + \frac{3}{2} g_F - \frac{1}{3} g_G + g_H - g_I + \frac{1}{3} g_J \quad (\text{E.3-xi})$$

$$\left. \frac{\partial P_3'(x, Y)}{\partial y} \right|_F = \sqrt{3} \left( -\frac{1}{9} g_A + \frac{2}{3} g_C + \frac{1}{6} g_D - \frac{2}{3} g_E + \frac{1}{6} g_F - \frac{1}{9} g_G \right. \\ \left. + \frac{1}{3} g_H - \frac{1}{3} g_I - \frac{1}{9} g_J \right) \quad (\text{E.3-xii})$$

$$\left. \frac{\partial P_3'(x, Y)}{\partial x} \right|_G = -\frac{11}{6} g_G + 3g_H - \frac{3}{2} g_I + \frac{1}{3} g_J \quad (\text{E.3-xiii})$$

$$\left. \frac{\partial P_3'(x, Y)}{\partial y} \right|_G = \sqrt{3} \left( \frac{2}{9} g_A - g_B + 2g_D - \frac{11}{18} g_G - g_H + \frac{1}{2} g_I - \frac{1}{9} g_J \right) \quad (\text{E.3-xiv})$$

$$\left. \frac{\partial P_3'(x, Y)}{\partial x} \right|_H = -\frac{1}{3} g_G - \frac{1}{2} g_H + g_I - \frac{1}{6} g_J \quad (\text{E.3-xv})$$

$$\left. \frac{\partial P_3'(x, Y)}{\partial y} \right|_H = \sqrt{3} \left( \frac{2}{9} g_A - \frac{2}{3} g_B - \frac{1}{3} g_C + \frac{2}{3} g_D + \frac{4}{3} g_E - \frac{1}{9} g_G \right. \\ \left. - \frac{5}{6} g_H - \frac{1}{3} g_I + \frac{1}{18} g_J \right) \quad (\text{E.3-xvi})$$

$$\left. \frac{\partial P_3'(x, Y)}{\partial x} \right|_I = \frac{1}{6} g_G - g_H + \frac{1}{2} g_I + \frac{1}{3} g_J \quad (\text{E.3-xvii})$$

$$\left. \frac{\partial P_3'(x, Y)}{\partial y} \right|_I = \sqrt{3} \left( \frac{2}{9} g_A - \frac{1}{3} g_B - \frac{2}{3} g_C + \frac{4}{3} g_E + \frac{2}{3} g_F + \frac{1}{18} g_G \right. \\ \left. - \frac{1}{3} g_H - \frac{5}{6} g_I - \frac{1}{8} g_J \right) \quad (\text{E.3-xix})$$

$$\left. \frac{\partial P_3^1(x, y)}{\partial x} \right|_J = -\frac{1}{3} g_G + \frac{3}{2} g_H - 3g_I + \frac{11}{6} g_J \quad (\text{E.3-ix})$$

$$\left. \frac{\partial P_3^1(x, y)}{\partial y} \right|_J = \sqrt{3} \left( \frac{2}{9} g_A - g_C + 2g_F - \frac{1}{9} g_G + \frac{1}{2} g_H - g_I - \frac{11}{18} g_J \right) \quad (\text{E.3-xx})$$

## APPENDIX F

### BOUNDARY CONDITIONS AT $\gamma = \pi/3$

There is a relationship among the different K-components of the intrinsic wavefunction along the  $\gamma = \pi/3$  boundary. The condition is

$$\frac{\sqrt{1+\delta} A_K(\beta, \gamma=\pi/3)}{D_{K0}^J(\pi/2, \pi/2, \pi)} = \frac{A_{K+2}(\beta, \gamma=\pi/3)}{D_{K+20}^J(\pi/2, \pi/2, \pi)} \quad K = 0, 2, \dots, J-2 \quad (F.1)$$

This condition will be proved in this appendix.

The rotational kinetic energy has already been given by equation (3.18):

$$\hat{T}_{\text{rot}} = p \hat{J}^2 + (q-p) \hat{J}_3^2 + \frac{1}{2} r (\hat{J}_+^2 + \hat{J}_-^2) \quad (F.2)$$

$$\text{where } p = \frac{1}{4} \left( \frac{1}{J_1} + \frac{1}{J_2} \right), \quad q = \frac{1}{2J_3}, \quad r = \frac{1}{4} \left( \frac{1}{J_1} - \frac{1}{J_2} \right). \quad (F.3-i, ii, iii)$$

The Bohr moments of inertia are

$$\mathcal{J}_v(\beta, \gamma) = 4B\beta^2 \sin^2(\gamma - \frac{2\pi}{3} v) \quad (F.4)$$

It is observed that

$$\mathcal{J}_v(\beta, \gamma = \pi/3) = 0 \quad (F.5)$$

As a result, the inertial parameters  $p$  and  $r$  become infinite at the oblate ( $\gamma = \pi/3$ ) boundary. This property of the inertial parameters leads to the condition given by equation (F.1)

It is convenient to define

$$s = \pi/3 - \gamma \quad (F.6)$$

Near the oblate boundary the moment of inertia about the 2-axis is approximately

$$j_2 \sim 4B\beta^2 s^2 \quad s \ll 1. \quad (F.7)$$

Thus, in the same limit the angular momentum operator coefficients in equation (F.2) are proportional to  $s^{-2}$ :

$$p \propto 1/(4B\beta^2 s^2), \quad (q-p) \propto -1/(4B\beta^2 s^2), \quad r \propto -1/(4B\beta^2 s^2). \quad (F.8-i, ii, iii)$$

Near  $\gamma = \pi/3$ , the following relation is approximately valid:

$$\hat{T}_{\text{rot}} \approx \hat{T}'_{\text{rot}} / (4B\beta^2 s^2) \quad s \ll 1 \quad (F.9)$$

where

$$\hat{T}'_{\text{rot}} = \frac{1}{4} \hat{J}^2 - \frac{1}{4} \hat{J}_3^2 - \frac{1}{8} (\hat{J}_+^2 + \hat{J}_-^2). \quad (F.10)$$

The rotational energy has been given in equation (3.33)

as

$$\begin{aligned} \langle \psi_{\lambda JM} | \hat{T}_{\text{rot}} | \psi_{\lambda JM} \rangle &= \sum_{K, K'} \iint d\beta_x d\beta_y Q(\beta_x, \beta_y) A_{\lambda JK'}^*(\beta_x, \beta_y) \\ &\times \langle \phi_{MK'}^J | \hat{T}'_{\text{rot}} | \phi_{MK}^J \rangle A_{\lambda JK}(\beta_x, \beta_y). \end{aligned} \quad (F.11)$$

For  $s \ll 1$ ,  $\hat{T}_{\text{rot}} \propto 1/s^2$  and  $Q(\beta_x, \beta_y) = 2B^{5/2} \beta_y (3\beta_x^2 - \beta_y^2) \propto s$ .

In order to avoid a  $1/s$  singularity in the integrand of equation (F.11) as  $s \rightarrow 0^+$ , it is necessary that the coefficient of the  $1/s$  term be zero. This implies that

$$\sum_{K, K'} A_{\lambda JK'}^*(\beta, \gamma=\pi/3) \langle \phi_{MK'}^J | \hat{T}'_{\text{rot}} | \phi_{MK}^J \rangle A_{\lambda JK}(\beta, \gamma=\pi/3) = 0. \quad (F.12)$$

Using the analytic expressions for the rotational matrix elements (equations (3.24), (3.25)) and simplifying the notation somewhat, the following condition is obtained:

$$\sum_{K=0}^J \frac{1}{4} (J(J+1) - K^2) A_K^2 - \frac{1}{4} \sum_{K=0}^{J-2} T_{K, K+2}^J A_K A_{K+2} = 0 \quad (\text{F.13})$$

where

$$T_{KK+2}^J = \sqrt{(1 + \delta_{K0}) (J+K+2) (J+K+1) (J-K) (J-K-1)} \quad (\text{F.14})$$

For  $\gamma = \pi/3$ ,  $\beta_1(\beta, \gamma = \pi/3) = \beta_2(\beta, \gamma = \pi/3)$ . As a result the operator  $\hat{T}_{\text{rot}}$  is axially symmetric about the 2-axis. If  $K_2$  represents the quantum number specifying angular momentum about the 2-axis, then  $|\phi_{K_2}^J\rangle$  is an eigenfunction of  $\hat{T}_{\text{rot}}$ . Moreover since  $\beta_2 = 0$  at  $\gamma = \pi/3$ , it is necessary that  $K_2 = 0$ . This can be stated mathematically as

$$\hat{T}_{\text{rot}} |\phi_{K_2=0}^J\rangle = E |\phi_{K_2=0}^J\rangle \quad s \ll 1 \quad (\text{F.15})$$

Since  $\hat{T}'_{\text{rot}}$  is proportional to  $\hat{T}_{\text{rot}}$ ,  $|\phi_{K_2=0}^J\rangle$  is also an eigenfunction of  $\hat{T}'_{\text{rot}}$ :

$$\hat{T}'_{\text{rot}} |\phi_{K_2=0}^J\rangle = E' |\phi_{K_2=0}^J\rangle \quad s \ll 1 \quad (\text{F.16})$$

Hence

$$E = E' / (4B\beta^2 s^2) \quad (\text{F.17})$$

For the energy  $E$  to be finite, it is necessary that  $E' = 0$ . As a result equation (F.15) becomes

$$\hat{T}'_{\text{rot}} |\phi_{K_2=0}^J\rangle = 0 \quad (\text{F.18})$$

The state  $|\phi_{K_2=0}^J\rangle$  can be expressed in terms of the usual basis in which the 3-axis is the quantization axis. Let  $\hat{u}$  be the rotation operator which rotates a state by Euler angles  $(\pi/2, \pi/2, \pi)$ . (This is equivalent to the variable change  $X \rightarrow Z$ ,  $Y \rightarrow X$ ,  $Z \rightarrow Y$ ). Then equation (F.18) becomes

$$\hat{T}'_{\text{rot}} \hat{U} |\phi_{K=0}^J\rangle = 0 \quad (\text{F.19})$$

$$\dots \langle \phi_K^J | \hat{T}'_{\text{rot}} \hat{U} | \phi_{K=0}^J \rangle = 0 \quad (\text{F.20})$$

For definiteness we assume  $J \geq 2$  and  $J$  is even. For states appropriate to the  $\Lambda$  representation of the  $D_2$  group, the relevant values for  $K$  are  $K = 0, 2, \dots, J$ . There are three cases for equation (F.20).

Case (i)  $K=0$ : Inserting a complete set of states between the operators in equation (F.20) for this case we obtain

$$\begin{aligned} \langle \phi_{K=0}^J | \hat{T}'_{\text{rot}} | \phi_{K=0}^J \rangle \langle \phi_{K=0}^J | \hat{U} | \phi_{K=0}^J \rangle \\ + \langle \phi_{K=0}^J | \hat{T}'_{\text{rot}} | \phi_{K=2}^J \rangle \langle \phi_{K=2}^J | \hat{U} | \phi_{K=0}^J \rangle = 0 \end{aligned} \quad (\text{F.21})$$

where only  $K=0$  and  $K=2$  states give non-vanishing matrix elements.

Using the  $A$  representation state

$$|\phi_K^J\rangle = \frac{1}{\sqrt{2(1+\delta_{K0})}} (|JK\rangle + (-1)^J |J-K\rangle)$$

(already given in equation (B.12)) the matrix elements of  $\hat{U}$  can be written

$$\begin{aligned} \langle \phi_K^J | \hat{U} | \phi_{K'}^J \rangle &= [ \langle JK | \hat{U} | JK' \rangle + \langle JK | \hat{U} | J-K' \rangle ] / \sqrt{(1+\delta_{K0})(1+\delta_{K'0})} \\ &= [ D_{KK'}^J(\frac{\pi}{2}, \frac{\pi}{2}, \pi) + D_{K-K'}^J(\frac{\pi}{2}, \frac{\pi}{2}, \pi) ] / \sqrt{(1+\delta_{K0})(1+\delta_{K'0})} \\ &= 2 D_{KK'}^J(\frac{\pi}{2}, \frac{\pi}{2}, \pi) / \sqrt{(1+\delta_{K0})(1+\delta_{K'0})} \end{aligned} \quad (\text{F.22})$$

using the fact that  $J, K$  and  $K'$  are all even. Equation (F.21) becomes

$$\frac{1}{4} J(J+1) D_{00}^J - \frac{1}{8} T_{02}^J \sqrt{2} D_{20}^J = 0 \quad (F.23)$$

$$\therefore \frac{T_{02}^J D_{20}^J}{\sqrt{2} D_{00}^J} = J(J+1) \quad (F.24)$$

Henceforth explicit reference to the Euler angles  $(\pi/2, \pi/2, \pi)$  in the  $D_{KK}^J$  functions is suppressed.

Case (ii)  $K = J$ : For this case equation (f.20) becomes

$$\begin{aligned} & \langle \phi_{K=J}^J | \hat{T}_{\text{rot}} | \phi_{K=J}^J \rangle \langle \phi_{K=J}^J | \hat{U} | \phi_{K=0}^J \rangle \\ & + \langle \phi_{K=J}^J | \hat{T}_{\text{rot}} | \phi_{K=J-2}^J \rangle \langle \phi_{K=J-2}^J | \hat{U} | \phi_{K=0}^J \rangle = 0 \end{aligned} \quad (F.25)$$

$$\frac{1}{4} J \sqrt{2} D_{J0}^J - \frac{1}{8} T_{J-2J}^J \sqrt{2} D_{J-20}^J = 0 \quad (F.26)$$

$$\therefore \frac{T_{J-2J}^J D_{J0}^J}{D_{J-20}^J} = \frac{(T_{J-2J}^J)^2}{2J} \quad (F.27)$$

If  $J \geq 4$ , there is a case (iii),  $2 \leq K \leq J-2$ :

$$\begin{aligned} & \langle \phi_K^J | \hat{T}_{\text{rot}} | \phi_K^J \rangle \langle \phi_K^J | \hat{U} | \phi_K^J \rangle + \langle \phi_K^J | \hat{T}_{\text{rot}} | \phi_{K-2}^J \rangle \langle \phi_{K-2}^J | \hat{U} | \phi_{K=0}^J \rangle \\ & + \langle \phi_K^J | \hat{T}_{\text{rot}} | \phi_{K+2}^J \rangle \langle \phi_{K+2}^J | \hat{U} | \phi_{K=0}^J \rangle = 0 \end{aligned} \quad (F.28)$$

$$\begin{aligned} & \frac{1}{4} [J(J+1) - K^2] \sqrt{2} D_{K0}^J - \frac{1}{8} T_{K-2K}^J \sqrt{2} D_{K-20}^J \\ & - \frac{1}{8} T_{KK+2}^J \sqrt{2} D_{K+20}^J = 0 \end{aligned} \quad (F.29)$$

$$\therefore \frac{T_{KK+2}^J D_{K+20}^J}{D_{K0}^J} = 2[J(J+1) - K^2] - \frac{T_{K-2K}^J D_{K-20}^J}{D_{K0}^J \sqrt{1+\delta_{K2}}} \quad (F.30)$$

Define a set of quantities  $L_K$  by

$$L_K = \frac{\sqrt{1+\delta_{K0}} T_{KK+2}^J D_{K+20}^J}{2 D_{K0}^J} \quad (F.31)$$



Then from equation (F.24),

$$L_0 = J(J+1). \quad (F.32)$$

Equation (F.27) implies

$$L_{J-2} = (T_{J-2J}^J)^2 / (4J). \quad (F.33)$$

Finally if  $J \geq 4$ , equation (F.30) implies for  $2 \leq K \leq J$

$$\begin{aligned} L_K &= J(J+1) - K^2 - \frac{T_{K-2K}^J D_{K-20}^J}{2 D_{K0} \sqrt{1+\delta_{K2}}} \\ &= J(J+1) - K^2 - (T_{K-2K}^J)^2 / (4L_{K-2}). \end{aligned} \quad (F.34)$$

Consider the quantity  $X$  defined by

$$X \equiv \sum_{K=0}^{J-2} (\sqrt{L_K} A_K - \frac{T_{KK+2}^J A_{K+2}}{2\sqrt{L_K}})^2 \quad (F.35)$$

$$\begin{aligned} &= L_0 A_0^2 + \sum_{K=2}^{J-2} (L_K + \frac{(T_{K-2K}^J)^2}{4L_{K-2}}) A_K^2 + \frac{(T_{J-2J}^J)^2}{4L_{J-2}} A_J^2 - \sum_{K=0}^{J-2} T_{KK+2}^J A_K A_{K+2} \end{aligned} \quad (F.36)$$

Substituting equations (F.32), (F.33) and (F.34) into (F.36),  $X$  becomes

$$\begin{aligned} X &= J(J+1)A_0^2 + \sum_{K=2}^{J-2} [J(J+1) - K^2] A_K^2 + JA_J^2 - \sum_{K=0}^{J-2} T_{KK+2}^J A_K A_{K+2} \\ &= \sum_{K=0}^J [J(J+1) - K^2] A_K^2 - \sum_{K=0}^{J-2} T_{KK+2}^J A_K A_{K+2}. \end{aligned} \quad (F.37)$$

By comparing equation (F.13) with equation (F.37) it can be seen that  $X = 0$ .  $X$  has been defined in equation (F.35) as a sum of squares, each term in the sum must vanish identically; ie

$$\sqrt{L_K} A_K - \frac{T_{KK+2}^J A_{K+2}}{2\sqrt{L_K}} = 0 \quad K = 0, 2, 4, \dots, J-2 \quad (F.38)$$

This yields the desired boundary conditions for  $\gamma = \pi/3$ :

$$\frac{\sqrt{1+\delta_{K0}} A_K}{D_{K0}^J(\pi/2, \pi/2, \pi)} = \frac{A_{K+2}}{D_{K+20}^J(\pi/2, \pi/2, \pi)} \quad K = 0, 2, \dots, J-2 \quad (F.39)$$

These boundary conditions have been derived using the simple principle that the energy must be finite. The rather complicated symmetry arguments used by Kumar and Baranger in their original derivation of these boundary conditions are not required although some elegance may be lost.

## BIBLIOGRAPHY

- H. R. Andrews, D. Ward, R. L. Graham, J. S. Geiger, Nucl. Phys. .  
A219 (1974) 141.
- S. T. Belyaev, K. Danske Vidensk. Selsk. Mat.-Fys. Medd. 31  
(1959) No. 11.
- D. R. Bes, Nucl. Phys. 10 (1959) 373.
- A. Bohr, K. Danske Vidensk. Selsk. Mat.-Fys. Medd. 26 (1952) No. 14.
- A. Bohr, B.R. Mottelson, K. Danske Vidensk. Selsk. Mat.-Fys.  
Medd. 27 (1953) No. 16.
- A. P. Budnik, A. A. Seregin, Sov. J. Nucl. Phys. 19 (1974) 503. \*
- J. Burde, R. M. Diamond, F. S. Stephens, Nucl. Phys. A92 (1967)  
306.
- T. E. Clarkson, R. M. Diamond, F. S. Stephens, I. Perlman,  
Nucl. Phys. A93 (1967) 272.
- D. Cline, Bull. Am. Phys. Soc. 19 (1974) 27.
- T. K. Das, B. Banerjee, Phys. Rev. C7 (1973) 2590.
- T.K. Das, R. M. Dreizler, A. Klein, Phys. Lett. 34B (1971) 235.
- S. Das Gupta, A.B. Volkov, Phys. Rev. C6 (1972) 1893.
- A. S. Davydov, Quantum Mechanics (Pergamon Press, Oxford, 1965),  
P. 157.
- A. S. Davydov, A.A. Chaban, Nucl. Phys. 20 (1960) 499.
- A. S. Davydov, G.F. Filippov, Nucl. Phys. 8 (1958) 237.
- R M. Diamond, F.S. Stephens, W.J. Swiatecki, Phys. Lett. 11  
(1964) 315.
- J. M. Eisenberg, W. Greiner, Nuclear Theory, Vol. 1 (North-  
Holland, Amsterdam, 1970).

- C. Flaum, D. Cline, A.W. Sunyar, O.C. Kistner, Phys. Rev. Lett. 33 (1974) 973.
- G. Gneuss, U. Mosel, W. Greiner, Phys. Lett. 30B (1969) 397.
- Gotthard Gneuss, Walter Greiner, Nucl. Phys. A171 (1971) 449.
- J. A. Grau, Z.W. Grabowski, F. A. Rickey, P. C. Simms, R. M. Steffen, Phys. Rev. Lett. 32 (1974) 677.
- L. Grodzins, Phys. Lett. 2 (1962) 88.
- E. Grosse, F.S. Stephens, R.M. Diamond, Phys. Rev. Lett. 31 (1973) 840.
- S. M. Harris, Phys. Rev. Lett. 13 (1964) 663.
- S. M. Harris, Phys. Rev. 138B (1965) 509.
- A. S. Householder, The Theory of Matrices in Numerical Analysis, (Blaisdell, New York, 1964), p. 254.
- D. Inglis, Phys. Rev. 96 (1954) 1059.
- E. Isaacson, H.B. Keller, Analysis of Numerical Methods, (Wiley New York, 1966), p. 58.
- A. Johnson, H. Ryde, S. A. Hjorth, Nucl. Phys. A179 (1972) 753.
- A. K. Kerman, K. Danske Vidensk. Selsk. Mat.-Phys. Medd. 30 (1956) No. 15.
- T. L. Khoo, F. M. Bernthal, J. S. Boyno, R. A. Warner, Phys. Rev. Lett. 31 (1973) 1146.
- A. Klein, R. M. Dreizler, T. K. Das, Phys. Lett. 31B (1970) 333.
- C.-M. Ko, Private communication, 1974.
- Krishna Kumar, Michel Baranger, Nucl. Phys. A92 (1967) 608.
- C. Lanczos, Journal of Research of NBS, Washington, 1952.

- N. Lark, H. Morinaga, Nucl. Phys. 63 (1965) 466.
- R. M. Lieder, H. Beuscher, W. F. Davidson, A. Neskakis, C. Mayer-Boricke, Y. El Masri, P. Monseu, J. Steyaert, J. Vervier, Phys. Lett. 49B (1974) 161.
- J. C. Lisle, F. Kearns, G. D. Dracoulis, J. C. Willmot, W. F. Davidson, R. M. Lieder, H. Beuscher, A. Neskakis, C. Mayer-Boricke, Proc. International Conf. on Nuclear Physics, Munich, 1973, Vol. 1, p. 188.
- M. A. J. Mariscotti, Gertrude Scharf-Goldhaber, Brian Buck, Phys. Rev. 178 (1969) 1864.
- J. Meyer ter Vehn, Phys. Lett. 55B (1975) 273.
- J. Meyer ter Vehn, F. S. Stephens, R. M. Diamond, Phys. Rev. Lett. 32 (1974) 1383.
- H. Morinaga, Nucl. Phys. 75 (1966) 385.
- H. Morinaga, P. C. Gugelot, Nucl. Phys. 46 (1963) 210.
- H. Morinaga, N. Lark, Nucl. Phys. 67 (1965) 315.
- S. A. Moszkowski, Nuclear Spin Parity Assignments, ed. N. B. Gove, p. 429.
- B. R. Mottelson, J. G. Valatin, Phys. Rev. Lett. 5 (1960) 511.
- W. D. Myers, W. J. Swiatecki, Nucl. Phys. 81 (1966) 1.
- J. O. Newton, F. S. Stephens, R. M. Diamond, Nucl. Phys. A95 (1967) 357.
- W. Pauli, Handbuch der Physik 24/1 (Springer, Berlin, 1933) p.120.
- J. Rainwater, Phys. Rev. 79 (1950) 432.
- C.H. Reinsch, Num. Mat. 10 (1967) 177.

V. Rezvani, G. Gneuss, H. Arenhovel, Phys. Rev. Lett. 25 (1970) 1667.

C. K. Ross, Y. Nogami, Nucl. Phys. A211 (1973) 145.

O. Saethre, S. A. Hjorth, A. Johnson, S. Jagare, H. Ryde, Z. Szymanski, Nucl. Phys. A207 (1973) 486.

Mitsuo Sakai, Nuclear Data Tables A8 (1970) 323.

G. Scharff-Goldhaber, M. McKeown, W. F. Piel Jr., Phys. Lett. 44B (1973) 416.

T. Sebe, J. Nachamkin, Ann. of Phys. 51 (1969) 100.

B. C. Smith, A. B. Volkov, Phys. Lett. 47B (1973) 193.

H. J. Smith, J. C. Waddington, M. W. Johns, Bull. Am. Phys. Soc. 20 (1975) 624.

Raymond A. Rosenson, Rev. Mod. Phys. 45 (1973) 353.

F. S. Stephens, R. M. Diamond, D. Benson Jr., M. R. Maier, Phys. Rev. C7 (1973) 2163.

F. S. Stephens, R. M. Diamond, J. R. Leigh, T. Kammuri, K. Nakai, Phys. Rev. Lett. 29 (1972) 438.

F. S. Stephens, N. Lark, R. M. Diamond, Phys. Rev. Lett. 12 (1964) 225.

F. S. Stephens, N. Lark, R. M. Diamond, Nucl. Phys. 63 (1963) 82.

F. S. Stephens, R. S. Simon, Nucl. Phys. A183 (1972) 257.

P. Thieberger, Proc. Conf. on High Spin Nuclear States and Related Phenomenon, Stockholm, 1972.

A. B. Volkov, Phys. Lett. 35B (1971) 299.

D. Ward, R. L. Graham, J. S. Geiger, H. R. Andrews, Phys. Lett. 44B (1973) 39.

R. A. Warner, F. M. Bernthal, J. S. Boyno, T. L. Khoo, Phys.  
Rev. Lett. 31 (1973) 835.

R. R. Whitehead, Nucl. Phys. A182 (1972) 290.

Lawrence Wilets and Maurice Jean. Phys. Rev. 102 (1956) 788.

J. H. Wilkinson, The Algebraic Eigenvalue Problem (Oxford, 1965)  
p. 388.